Western&Graduate&PostdoctoralStudies

Western University
Scholarship@Western

Electronic Thesis and Dissertation Repository

12-10-2020 10:30 AM

The Effect of MoOx Reducibility on its Activity for Anisole Hydrodeoxygenation

Chantal Walker, *The University of Western Ontario*

Supervisor: Pjontek, Dominic, *The University of Western Ontario*
Co-Supervisor: Herrera, Jose, *The University of Western Ontario*
A thesis submitted in partial fulfillment of the requirements for the Master of Engineering Science degree in Chemical and Biochemical Engineering

Follow this and additional works at: https://ir.lib.uwo.ca/etd

Part of the Catalysis and Reaction Engineering Commons

Abstract

Catalytic hydrodeoxygenation (HDO) is a process for upgrading crude bio-oil as it has a high oxygen content which causes several undesirable properties. Current methods for HDO use sulfided NiMo and CoMo or supported noble metal catalysts which hydrogenate aromatic rings, leading to less valuable products and increasing the hydrogen consumption. Using 10 wt. % MoO_3 supported on ZrO_2, TiO_2, γ-Al_2O_3, SiO_2 and CeO_2, we investigated the atmospheric HDO of anisole, a model compound, at 350 °C. All catalysts achieved $C - O$ bond cleavage, preserving the aromatic ring. In situ UV-Vis spectroscopy showed a peak corresponding to intervalence charge transfer (IVCT) transitions where $Mo^{5+} - O - Mo^{6+} \rightarrow Mo^{6+} - O - Mo^{5+}$. The IVCT positions were used to classify the catalysts according to their degree of reduction. In general, a direct correlation is established between the supported catalyst's activity and its ability to preserve Mo^{5+} sites, preventing over-reduction to less active Mo^{4+} sites.

Summary for Lay Audience

Currently, the world's primary source of transportation fuel is fossil fuels, which contribute to climate change and are a non-renewable source of energy. Bio-oil, a renewable source of energy derived from biomass, such as wood and switchgrass, is considered a promising alternative source of energy. However, the problem is that it contains a high concentration of oxygen, leading to undesirable characteristics, such as high acidity. Therefore, oxygen must be removed for it to be considered a feasible source of energy. One method for achieving this is hydrodeoxygenation (HDO), where hydrogen (H_2) removes oxygen in the form of H_2O. HDO studies have been successfully carried out using different types of catalysts. However, with these catalysts, hydrogen not only reacts to break the carbon-oxygen bond, but also reacts to break the carbon double bonds to single bonds. This results in high levels of hydrogen consumption and lower value products. However, recently molybdenum oxide (MoO_3) on a support has been shown to be an effective catalyst for HDO, where hydrogen does not react with the carbon double bonds.

In this work, we investigated the impact of a support (ZrO_2, TiO_2, γ-Al_2O_3 and SiO_2) on the HDO activity using MoO_3. The ZrO_2 and TiO_2 supported catalysts had significantly higher degrees of HDO relative to the other catalysts and were the most stable. Although HDO using the γ-Al_2O_3 supported catalyst initially resulted in the highest levels of carbon-oxygen bond breaking, it did not break the specific carbon-oxygen bond needed to remove the oxygen and it deactivated quickly. Generally, we found that the activity of the catalyst was correlated with its ability to preserve a certain number of oxygen vacancies per Mo atom. If too many oxygen vacancies were created, then MoO_3 went to MoO_2 which is not active for HDO. The oxygen vacancies were the easiest to create on the ZrO_2 and TiO_2 supported catalysts but the γ-Al_2O_3 supported catalyst was able to prevent too many oxygen vacancies from being created. When the catalysts were synthesized, MoO_3 was the most dispersed on the γ-Al_2O_3 catalyst but post-reaction it was the least dispersed.

Acknowledgments

First, I would like to extend my sincere gratitude to my supervisors Dr. Herrera and Dr. Pjontek. Their knowledge, experience and guidance helped to steer me in the right direction when required. This work could not have been done without them.

I would also like to thank Wei Tian for his helpful advice and strong support throughout the duration of my thesis.

Finally, I would like to express my profound gratitude to my family and friends who provided support and encouragement, which helped give me motivation and strength when I needed it the most. This achievement wouldn't have been possible without them.

Table of Contents

List of Tables

List of Figures

List of Abbreviations

BTX – Benzene Toluene Xylene

E_a – Activation Energy

Eg – Band Gap Energy

 eV – Electron Volt

IVCT – Intervalence Charge Transfer

FCC – Fluid Catalytic Cracking

HDO – Hydrodeoxygenation

HDN - Hydrodenitrogenation

HDS - Hydrodesulphurization

HHV – Higher Heating Value

LMCT - Ligand-to-Metal Charge Transfer

NAP – Near-Ambient Temperature

RTP – Rapid Thermal Processing

STP – Standard Temperature and Pressure

TCD – Thermal Conductivity Detector

TGA – Thermogravimetric Analysis

T_{max} – Temperature corresponding to the maximum rate of reduction

TPR – Temperature Programmed Reduction

UHP – Ultra High Purity

UV-Vis DRS – Ultraviolet–Visible Spectroscopy Diffuse Reflectance Spectroscopy

WHSV - Weight Hourly Space Velocity

Chapter 1

1   Introduction

1.1   Background & Motivation

With the world energy demand projected to increase by a third through 2040 and with the concerns of depleting fossil fuel reserves and climate change, there is a growing need to research and develop clean and sustainable sources of energy (BP Energy Outlook, 2019). Renewables such as wind, solar, geothermal, biomass and biofuels are attractive sustainable energy sources and are expected to be the largest source of power by 2040 (BP Energy Outlook, 2019). Among renewables, biomass-based liquid fuel, known as biofuel, is an attractive option as it is the only renewable organic carbon resource in nature, which has the potential to directly replace fossil fuel based transportation fuels such as gasoline, diesel and jet fuel (Li et al., 2015). With growing concerns of greenhouse gas emissions associated with fossil fuels, biomass is considered an indispensable renewable source of fuel due to its lower net carbon emissions as plants absorb CO_2 as they grow. Furthermore, the development of biofuels would result in local and regional benefits such as providing energy security, rural development and economic growth (Eijck et al., 2014).

One process for converting biomass into bio-oil is known as fast pyrolysis, where biomass particles are heated to high temperatures in the absence of oxygen. The crude bio-oil, however, contains a much larger concentration of oxygen compared to conventional petroleum oil. This imparts many undesirable characteristics to bio-oil such as corrosivity, thermal and chemical instability, and immiscibility with petroleum oil (Miguel & Makibar, 2012). The oxygen must therefore be removed for bio-oil to be considered a feasible source of energy. One method of achieving this is known as hydrodeoxygenation (HDO), where hydrogen is reacted with bio-oil under favorable conditions to remove the oxygen in the form of H_2O.

Typically, HDO studies use phenolic model compounds, such as anisole, as they are representative of the lignin fraction of biomass, which is the component that is the most underutilized and difficult to hydrodeoxygenate. Several types of catalysts have successfully carried out HDO including conventional hydrotreating catalysts, such as sulfided NiMo and sulfided CoMo, as well as supported noble metal catalysts. However, these catalysts

hydrogenate the aromatic rings, resulting in high levels of H_2 consumption and lower octane numbers. Supported and bulk MoO_3 are promising catalysts as they have been shown to preserve the aromatic ring and selectively cleave the $C_{aromatic}$ – O bond over the weaker $C_{aliphatic}$ – O bond.

1.2   Thesis Objectives

The overall objective of the presented thesis is to synthesize and characterize MoO_3 catalysts on various supports to establish how the structure of the supported molybdenum oxide moieties affect the catalyst's activity for anisole hydrodeoxygenation. Potential descriptors of catalytic activity such as reducibility and cluster size are evaluated. The specific objectives of this thesis are summarized below:

- Study the effect of Mo – support interactions on the reducibility of supported molybdenum oxide by H_2-TPR.
- Investigate the impact of the support on the molybdenum oxide cluster size and surface reducibility via ex situ and in situ DRUV-Vis spectroscopy.
- Examine the effect of molybdenum oxide cluster size and reducibility on the activity of supported MoO_3 catalysts for anisole hydrodeoxygenation.

References

BP Energy Outlook. (2019). https://www.bp.com/content/dam/bp/business-sites/en/global/corporate/pdfs/energy-economics/energy-outlook/bp-energy-outlook-2019.pdf

Eijck, J. Van, Batidzirai, B., & Faaij, A. (2014). Current and future economic performance of first and second generation biofuels in developing countries. *Applied Energy*, *135*, 115–141. https://doi.org/10.1016/j.apenergy.2014.08.015

Li, C., Zhao, X., Wang, A., Huber, G. W., & Zhang, T. (2015). Catalytic Transformation of Lignin for the Production of Chemicals and Fuels. *Chemical Reviews*, *115*, 11559−11624. https://doi.org/10.1021/acs.chemrev.5b00155

Miguel, G. S., & Makibar, J. (2012). New Advances in the Fast Pyrolysis of Biomass. *Biobased Materials and Bioenergy*, *6*, 1–11. https://doi.org/10.1166/jbmb.2012.1209

Chapter 2

2   Literature Review

2.1   Biomass Classification and Composition

Biofuels are generally classified as either first or second generation. First generation biofuels, such as biodiesel and bioethanol, are produced from edible biomass feedstocks including corn, sugarcane, wheat and soybeans. Biodiesel, for example, is produced through transesterification of vegetable oils and fats while bioethanol is made via fermentation of sugars and starches. However, first generation biofuels require significant amounts of land, water and fertilizer and are controversial due to the "food vs. fuel" debate (Alalwan et al., 2019). These issues have increased interest in the development of second-generation biofuels which use inedible lignocellulosic biomass such as switch grass, sawdust, and agricultural and municipal wastes. The low cost and availability of lignocellulosic biomass make it an attractive renewable feedstock. However, more than 99% of all currently produced biofuels are first generation, primarily because lignocellulosic biomass must be separated into its main components for efficient downstream processing and upgrading, which is a complex and expensive process (Eijck et al., 2014; Den et al., 2018).

Lignocellulosic biomass consists of three main polymers: cellulose (40 – 50 wt. %), hemicellulose (25-35 wt. %), and lignin (15-20%), with varying composition depending on the source of biomass (Figure 2.1) (Huber et al., 2006; Rowell et al., 2005; Mohan et al., 2006). Cellulose is a high molecular weight linear polysaccharide of β-glycosidic linked glucose monomers with a degree of polymerization of up to 9,000-10,000 units (Huber et al., 2006; Rowell et al., 2005; Mohan et al., 2006). Hemicellulose is an amorphous branched polymer consisting of five carbon (xylose and arabinose) and six carbon (glucose, galactose and manose) monosaccharaides with uronic acid substituents that are linked by β-glycosidic bonds. On average, it has 100-200 repeating monosaccharaides (Rowell et al., 2005; Mohan et al., 2006). Lastly, lignin is an amorphous cross-linked resin with no exact structure and is rich in oxygenated aromatic species; it's mainly composed of three phenolic compounds: p-coumaryl alcohol, coniferyl alcohol and sinapyl alcohol (Molino et al., 2016). Lignin is vital to the structural integrity of plants, encompassing the hemicellulose and cellulose fractions.
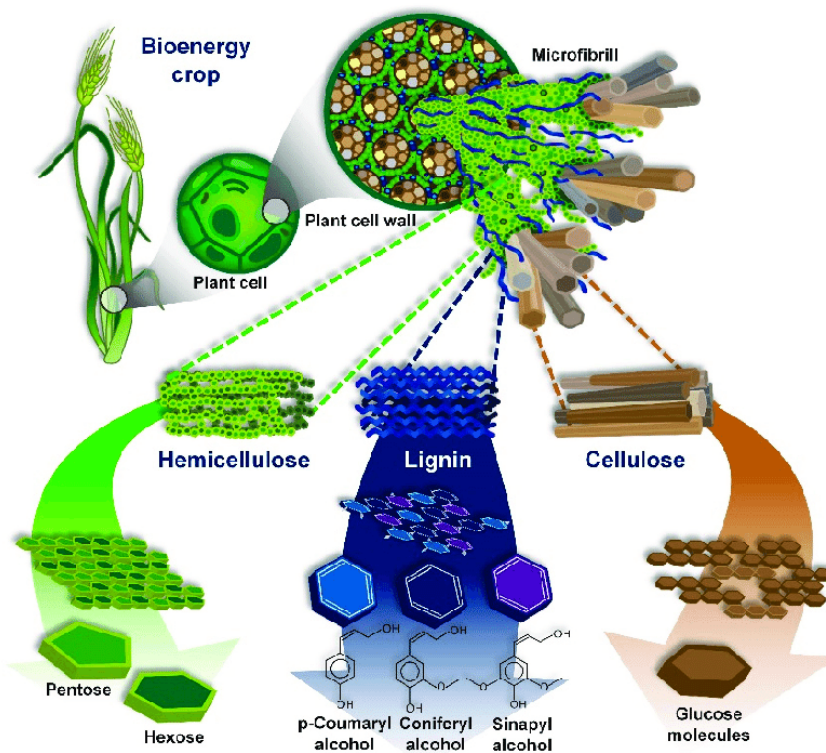
Figure 2.1 Structure of lignocellulosic biomass (Bajpai, 2016)

2.2   Biomass Conversion Processes

The production of biofuels from lignocellulosic feedstocks can be achieved through biochemical processes and/or thermochemical processes. Biochemical processes use enzymes and microorganisms to convert biomass into valuable products, whereas thermochemical processes, such as gasification, liquefaction and pyrolysis, convert biomass by using heat, catalysts and/or chemical reactants.

Biochemical conversion of lignocellulosic biomass involves enzymatic hydrolysis to depolymerize cellulose and hemicellulose to its monomer sugars which are then typically fermented to produce bioethanol. However, the outer lignin layer makes it difficult for enzymes to access the internal polysaccharides. Therefore, biomass must be thermochemically pretreated in order to increase the yield of fermentable sugars. Although enzymatic hydrolysis is characterized by high product selectivity, removing lignin from the feedstock prior to its conversion is costly and results in an unwanted loss of carbon (Buck et al., 2020).

Another route for biomass conversion is gasification. This process involves the partial combustion of biomass using steam, air or oxygen at temperatures of 800-900 °C to produce synthesis gas (mixture of CO, H_2, CO_2 and CH_4), commonly referred to as syngas (Raheem et al., 2015). Syngas can be converted to methanol or upgraded to produce diesel-like fuel via the Fischer-Tropsch process. However, high quality syngas is difficult to obtain with the main pollutants being tar, ammonia and sulphuric/chloridric acids (Molino et al., 2016).

A biomass conversion process which does produce high quality products is liquefaction. In this process, biomass is converted in a hot and pressurized solvent environment where it is broken down to bio oil. This process requires high pressures (5-20 MPa), moderate temperatures (300-400 °C) and residence times of 0.2-1.0 h (longer than gasification and pyrolysis) (Xiu & Shahbazi, 2012). Unlike gasification and pyrolysis, liquefaction can process wet biomass feedstocks, eliminating the drying pre-treatment step. Liquefaction produces higher quality bio oil compared to pyrolysis, with higher heating values and lower oxygen contents. However, it has lower yields (20-60 %) compared to pyrolysis (up to 80% of a dry feed) and higher operating pressures resulting in higher capital costs (Xiu & Shahbazi, 2012).

In pyrolysis, lignocellulosic biomass is converted to a wide range of products including non-condensable gases (CO, CO_2 and H_2), condensable vapors, and solid biochar by heating the feedstock in the absence of oxygen at near atmospheric pressures (Puy et al., 2013). Cooling and condensation of the vapours results in a dark brown liquid known as bio-oil. Product yields of pyrolysis are highly dependent on the reaction temperature, heating rate, residence time, feedstock and reactor configuration (Akhtar et al., 2012). Although pyrolysis has been used for thousands of years for charcoal production, it was only within the last 40 years that the process was modified to maximize oil yields. Pyrolysis can be classified as slow, intermediate or fast, depending on the reaction temperature and vapour residence time. Traditional slow pyrolysis for biochar production is typically performed at a temperature of 400 °C with low heating rates (0.1-1.0 °C/s) (Babu, 2008) and extremely long vapour residence times (days) (Bridgwater, 2015). Long vapour residence times allow the produced vapours to continually react and form biochar and non-condensable gases (Zhang et al., 2010). Therefore, the liquid yield from slow pyrolysis of dry wood is only about 30 wt. % (Bridgwater, 2015). Fast pyrolysis can maximize the bio-oil yield up to 75 wt. % by limiting the residence time to less than 2 seconds

(Bridgwater, 2015), using faster heating rates (10-200 °C/s), operating at slightly higher temperatures (500 °C) and by rapid condensation of the product vapours (Babu, 2008).

Thermochemical techniques are preferred to biochemical conversion methods as they are more energy efficient, they have shorter reaction times and they convert all the biomass fractions, including lignin, to high-value biofuel (Leibbrandt et al., 2011). Fast pyrolysis has shown to be a promising thermochemical process due to its reduced operating pressure and higher liquid yield compared to liquefaction. Furthermore, the liquid bio oil product can be easily transported and stored unlike the syngas produced from gasification (Xiu & Shahbazi, 2012).

2.3   Commercialized Fast Pyrolysis

Fluidized bed systems have been successful at meeting the stringent requirements of fast pyrolysis and involve the injection of dried biomass particles into a fluidized bed of hot sand particles (Figure 2.2). Several companies have successfully commercialized fast pyrolysis, including Ensyn with Rapid Thermal Processing (RTP) technology for the production of liquids from wood biomass. In the Ensyn RTP process, hot sand particles rapidly come into contact with the solid biomass feedstock and fragments it into vapours, gases and char. The vapours are rapidly quenched and recovered as bio-crude, while the gases and char flow to a second vessel where the sand is reheated and recirculated back to the reactor. Ensyn has a plant located in Renfrew, Ontario with a processing capacity of approximately 70 dry tons/day of wood residues (Ensyn, n.d.). Red Arrow is another company that uses Ensyn's RTP technology with 5 plants located in Wisconsin. Of the 5 facilities, the three larger units process 30-40 dry tons/day of wood residues (Ensyn, n.d.).
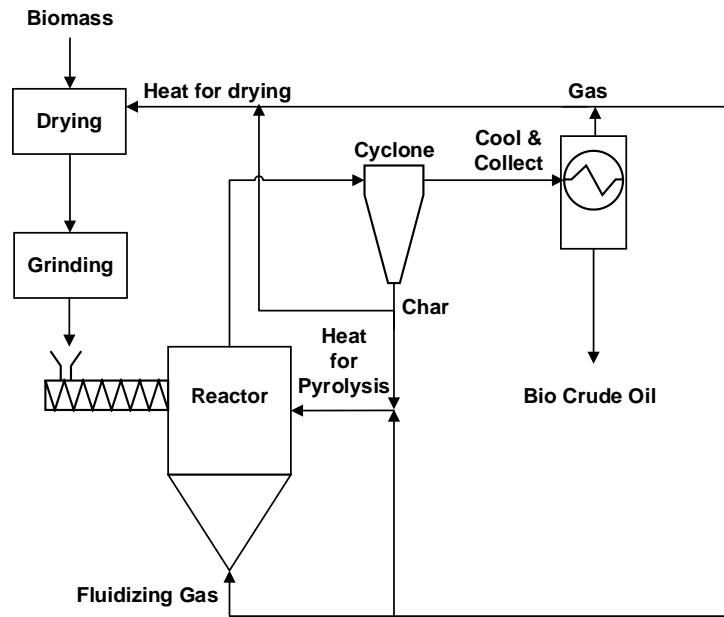
Figure 2.2 Schematic of fast pyrolysis process

2.4   Pyrolysis Bio-Oil vs Petroleum Oil

Bio-oil has a significantly higher oxygen content compared to petroleum oil, which results in many undesireable properties (Table 1). The high oxygen content lowers the higher heating value (HHV) of bio-oil compared to conventional fuel and the polarity of oxygen rich molecules makes bio-oil immiscible with non-polar hydrocarbons in petroleum oil (Miguel & Makibar, 2012). Bio-oils are also very acidic with a pH of about 2.5, mainly due to the presence of acetic and formic acids (Zhang et al., 2010). The high acidity of the oil corrodes most common construction materials such as carbon steel and aluminum. Bio-oil also exhibits a wide range of viscosities, which can increase when handled at high temperatures due to its thermal instability (Czernik & Bridgwater, 2004). It is also chemically unstable due to reactive organic compounds, such as aldehydes and phenols, which can polymerize and increase the bio-oil viscosity and molecular weight. This process is known as 'aging' and the water generated from these reactions can lead to phase separation of bio-oil into water-soluble and organic fractions (Oasmaa & Czernik, 1999). Bio-oil also has a higher water content than petroleum oil, causing ignition delays and lowering the combustion rate and heating value (Miguel & Makibar, 2012). The high moisture content, however, has some positive effects, such as enhancing bio-oil flow characteristics and lowering NO_x emissions (Czernik &

8

Bridgwater, 2004). Biomass-derived pyrolysis bio-oils must thus be deoxygenated to obtain similar properties to conventional crude oils or transportation fuels.

Table 2.1 Property comparison between raw bio-oil and crude oil (Venderbosch et al., 2010; Oasmaa & Czernik, 1999; Ruddy et al., 2014)

Property	Crude Bio-Oil	Crude Petroleum Oil
Water (wt. %)	15 – 30	0.1
pH	2.8 – 3.8	–
Elemental Analysis		
C (wt. %)	55 – 65	83 – 86
O (wt. %)	28 – 40	<1
H (wt. %)	5 – 7	11 – 14
S (wt. %)	<0.05	<4
N (wt. %)	<0.4	<1
HHV (MJ/kg)	16-19	44
Viscosity at 50 °C (cP)	40-100	180
Ash (wt. %)	<0.2	0.1

2.5   Raw Bio-oil Applications

Raw bio-oil can be burned in adapted boilers to generate heat and results in lower NO_x and SO_x emissions compared to the levels produced when burning fossil fuel, though particulate emissions are typically higher (Gust, 1997). Fewer pollutants are emitted when using raw bio-oil in turbines, with the exception of carbon monoxide (Bridgwater, 2004; Oasmaa et al., 2005). However, raw bio-oil must first be filtered to remove particulates as they cause fouling and corrosion of the turbine blades. Raw bio-oil has also been successfully used in diesel engines to generate power but there are major concerns, such as difficult ignition, corrosion, and coking.

2.6   Bio-Oil Upgrading Processes

There are two main routes for deoxygenation of pyrolysis bio-oils: zeolite cracking and hydrodeoxygenation (HDO). The main difference is that HDO uses high hydrogen pressures

whereas zeolite cracking occurs in the absence of hydrogen at atmospheric pressure. Both methods involve simultaneous reactions such as cracking, decarbonylation, decarboxylation, hydrocracking, hydrodeoxygenation and hydrogenation, though the extents of the reactions depend on the upgrading method and the composition of the feed (Figure 2.3). Undesirable polymerization and polycondensation reactions also occur, resulting in coke formation.
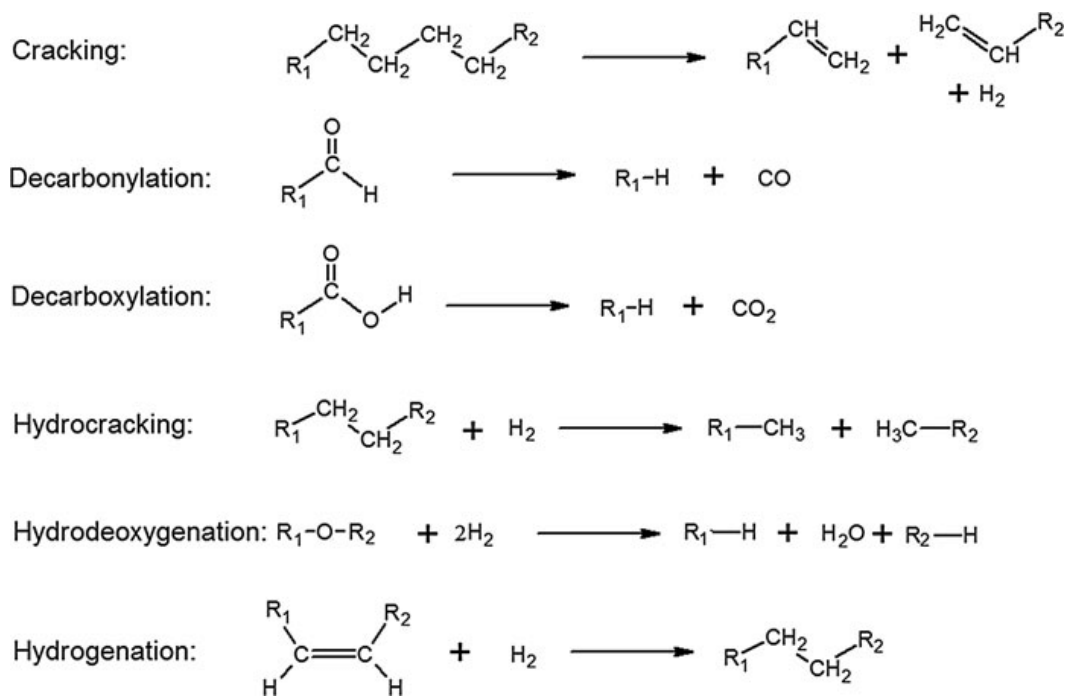
Figure 2.3 Main reactions involved in catalytic bio-oil upgrading (Mortensen et al., 2011)

Bio-oil catalytic cracking is similar to fluid catalytic cracking (FCC) used in the petroleum industry; it's carried out at atmospheric pressure, in the absence of H_2, and uses acidic zeolite catalysts at temperatures ranging from 350 to 500 °C (Huber et al., 2006). Currently, Envergent Technologies, a company created as a joint venture between Honeywell UOP and Ensyn, has commercialized the co-feeding of crude bio-oil and crude petroleum oil into an FCC unit to produce gasoline and diesel. In this process, cracking is the primary reaction which converts heavy molecules to light components, and oxygen is rejected as CO_2 and H_2O (Chang & Silvestri, 1977). The conceptual reaction of this mechanism is summarized in Eq. (1), where $CH_{1.2}$ represents an unidentified hydrocarbon product. Unlike HDO, zeolite cracking doesn't require an external H_2 source, significantly lowering the cost. However, the restricted hydrogen results in a low H/C ratio of the zeolite cracking oil, implying that the hydrocarbon products

from these reactions are typically aromatics and have heating values that are 25% lower than crude oil (Saidi et al., 2014). The zeolite catalysts quickly deactivate as coking levels are high, ranging from 30 to 40 g/g bio-oil feed (Adjaye et al., 1996; Katikaneni et al., 1995). Consequently, bio-oil yields are low, ranging from 14-23 wt.% (Balat et al., 2009).

$$CH_{1.4}O_{0.4} \rightarrow 0.9CH_{1.2} + 0.1\,CO_2 + 0.2\,H_2O \quad (1)$$
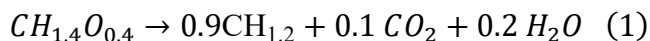
In catalytic HDO, the main reaction that takes place is hydrodeoxygenation, where oxygen is removed in the form of H_2O. Minor amounts of CO_2 and CO are also formed via undesirable endothermic decarboxylation and decarbonylation reactions, respectively, lowering the upgraded bio-oil carbon yield. The general HDO reaction of bio-oil is shown below with an overall heat of reaction of 2.4 MJ/kg (Saidi et al., 2014). Although HDO requires an external H_2 source, thereby increasing upgrading costs, it is the preferred upgrading route due to higher yields and compatibility with existing hydrotreating technologies.

$$CH_{1.4}O_{0.4} + 0.7H_2 \rightarrow 1"CH_2" + 0.4\,H_2O \quad (2)$$
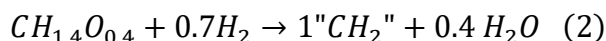
2.7   Hydrodeoxygenation of Bio Oil: Model Compounds

Raw pyrolysis bio-oil is a complex mixture of oxygenated hydrocarbons resulting from depolymerization of the cellulose, hemicellulose and lignin fractions, and subsequent simultaneous isomerization, dehydration, repolymerization/condensation and cracking reactions. More than 400 different compounds in pyrolytic bio-oils have been identified consisting of acids, esters, alcohols, ketones, aldehydes and phenols (Huber et al., 2006). Rather than using pyrolysis bio-oil at the lab-scale, most studies use model compounds to provide insights on the reaction kinetics and mechanisms and to compare the performance of catalysts. Model compounds are also used due to the unstable nature of bio-oils during storage.

Bio-oil produced from lignocellulosic biomass contains a large fraction (30 to 40 wt. %) (Bertero et al., 2012; Lazzari et al., 2016; Wang et al., 2009) of lignin-derived phenolic species. These compounds are highly resistant to HDO due to the high strength of their $C_{aromatic} - O$ bonds and are the primary cause for coking and catalyst deactivation (Hong et al., 2010). Lignin on its own has significant potential to be converted to bio-oil as it is an underutilized source of aromatic compounds and is readily available. Lignin is currently regarded as a waste product

in lignocellulosic biomass to bioethanol processes. Another major source of lignin is from the pulp and paper industry, accounting for 90% of total lignin production (Azadi et al., 2013). Here 50 million tons of lignin are produced as a by-product with only 2 % being commercially available, and the remainder being burned as low-value fuel for steam and electricity generation (Laurichesse & Avérous, 2014; Kim et al., 2014; Li & Mcdonald, 2014). Therefore, lignin-derived phenolic species such as phenol, guaiacol and anisole are typically selected as model compounds for HDO. In this study, we selected anisole as the model compound as it is less complex to study the reaction mechanism than guaiacol, with two separate functional groups, but more complex than phenol, which has only two main parallel routes: direct deoxygenation to benzene by cleavage of the $C - O$ bond and hydrogenation, in which the aromatic ring is hydrogenated to cyclohexanol. It should be noted, however, that complications can arise when applying the information obtained using model compounds to real pyrolysis bio-oils.

2.8 Reaction Pathways in Bio Oil Hydrodeoxygenation

Two reaction pathways are generally accepted for the HDO of lignin-derived aromatic oxygenates: 1) hydrogenation followed by deoxygenation to ring-saturated hydrocarbons and 2) direct deoxygenation via $C - O$ bond cleavage to aromatic hydrocarbons (Jin et al., 2019; Zhang et al., 2020; Pourzolfaghar et al., 2018). An overview of the main reaction pathways that have been observed for HDO of anisole is presented in Figure 2.4. The hydrogenation route is highlighted in green and the direct deoxygenation route is highlighted in red, respectively. After methoxycyclohexane is formed in the hydrogenation route, it can be directly deoxygenated to form cyclohexane (Li et al., 2017). Alternatively, the $C_{aliphatic} - O$ bond can break, forming cyclohexanol, which can then be deoxygenated to form cyclohexane (Khromova et al., 2014). Another pathway involves demethylation to form phenol, followed by aromatic ring hydrogenation forming cyclohexanol, and then finally deoxygenation to cyclohexane (Feliczak-guzik et al., 2020). The direct deoxygenation route involves breaking either the $C_{aromatic} - O$ bond to form benzene directly (Prasomsri et al., 2014), or breaking the $C_{aliphatic} - O$ bond to form phenol, followed by deoxygenation to form benzene (Li et al., 2011). Some studies have reported that benzene can be subsequently hydrogenated to cyclohexane (Yakovlev et al., 2009). Typically, it's desirable to break the $C_{aromatic} - O$ bond in anisole rather than the $C_{aliphatic} - O$ bond in order to deoxygenate the compound; however, accomplishing this

12

is challenging, as the $C_{aromatic} - O$ bond energy exceeds that of the $C_{aliphatic} - O$ bond. Although not shown here, transalkylation reactions have also been reported (Zhu et al., 2011; Peters et al., 2015).
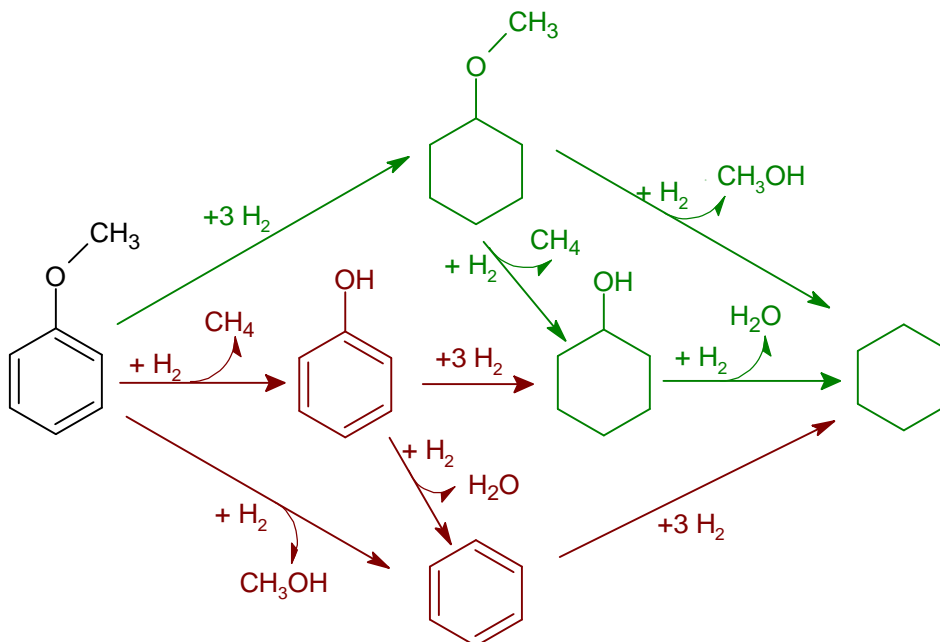
Figure 2.4 Proposed anisole HDO reaction pathways

The main pathway on this reaction network depends on the type of catalyst and on reaction conditions. The hydrogenation route is favoured for catalysts with either dominant hydrogen dissociation function, such as noble metal catalysts (Wildschut et al., 2010; (Zhao et al., 2009) or sulfided NiMo catalysts (Moreau et al., 1988; Moreau et al., 1990). On the other hand, the direct deoxygenation route is the main pathway for metal oxides and carburized analogues (Prasomsri et al., 2014), as well as for sulfided CoMo catalysts (Moreau et al., 1990; Weigold, 1982). Olcese et al. studied the equilibrium of guaiacol and hydrogen at atmospheric pressure and calculated the Gibbs free energy at different temperatures; they proposed that the aromatic ring began to be preserved above 427 °C, when coke tends to form (Olcese et al., 2012). Baddour et al. calculated the equilibrium constant as a function of temperature for the hydrogenation of benzene to cyclohexane at 0.44 MPa, shown in Figure 2.5a (Baddour et al., 2017). Since the reaction is exothermic, the equilibrium constant decreases as temperature increases, with benzene being favoured above 280 °C. The effect of pressure on the equilibrated product distribution at 300 °C is shown in Figure 2.5b. Increasing the pressure

will shift the equilibrium towards the formation of cyclohexane. The preservation of the aromatic ring is therefor favoured at high temperature and low hydrogen pressure, consistent with past experimental HDO results. For example, Rensel et al. found that increasing the temperature from 300 °C to 400 °C enhanced the benzene selectivity from 28% to 90% (Rensel et al., 2013). Yohe et al. observed a significant increase in arene selectivity when decreasing the pressure from 2.35 MPa to 0.101 MPa, going from near 0% to 93% (Yohe et al., 2016).
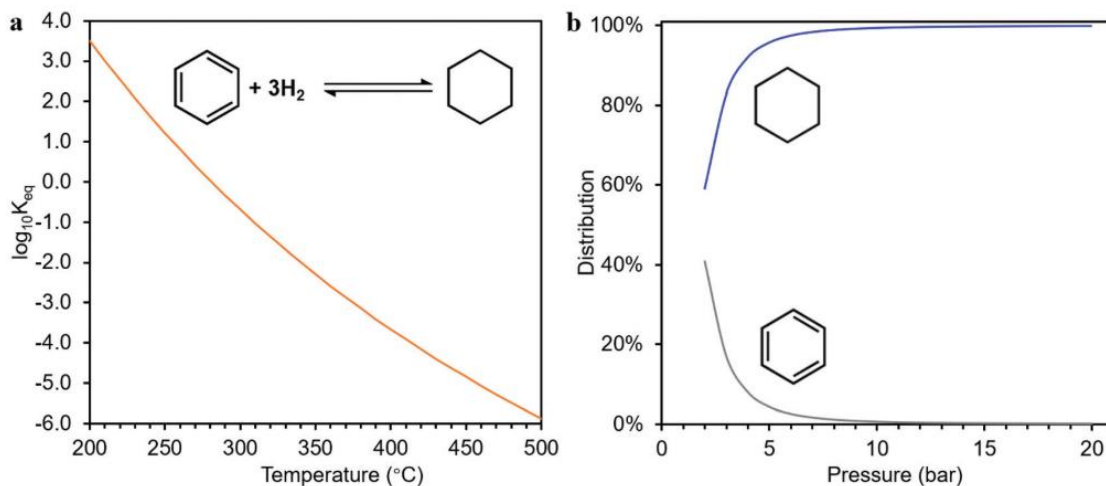
Figure 2.5 Position of the thermodynamic equilibrium for the hydrogenation of benzene to cyclohexane plotted as a) a function of temperature at 0.44 MPa and b) of total pressure at 300 °C (Zhang et al., 2020)

2.9   High Pressure Hydrodeoxygenation

High pressure or conventional HDO is similar to the well-established hydrodesulphurization (HDS) process used in petroleum refining, where sulfur is removed from organic compounds. Conventional HDO and HDS both use high hydrogen pressures to remove the heteroatoms, forming H_2O and H_2S, respectively. Operating conditions in conventional HDO range from pressures of 1 to 30 MPa and temperatures between 200 and 400 °C (Ohta et al., 2012; Mercader et al., 2010; Venderbosch et al., 2010). High pressures are used to ensure higher solubility of hydrogen in bio-oil and consequently the hydrogen availability in the vicinity of the catalyst. This increases the reaction rate and decreases coking in the reactor (Venderbosch et al., 2010).

2.10 Catalysts used for High Pressure Hydrodeoxygenation

Some of the first catalysts tested in HDO systems were sulfided 14 wt. % CoMo and NiMo catalysts supported on Al_2O_3 as they are traditional hydrotreating catalysts used in HDS processes. Although sulfided catalysts are reported to exhibit high HDO activity, they are rapidly stripped of their sulfur and therefore deactivate due to the low bio-oil sulfur content (0.05 wt.%) (Table 1). An external sulfur source (H_2S) is therefore required to regenerate the catalyst, though this results in contamination of the upgraded product. Sulfided catalysts are also prone to coking and water poisoning (Badawi et al., 2011; Viljava & Krause, 2005).

Noble transition metals such as Pt, Pd, Ru, Rh are promising for high HDO because they are known to activate hydrogen, are more tolerant to water poisoning, and do not require sulfur cofeeding (Gutierrez et al., 2009; Ohta et al., 2012). Transition metal catalysts should be bifunctional, where a support activates the oxy-compounds and the metal promotes hydrogen activation and donation to the oxygenated compounds (Mortensen et al., 2011). HDO of bio-oil was investigated at 350 °C and 20 MPa for 4 h over traditional sulfided catalysts and over zirconia supported mono- and bi-metallic noble metal (Ru, Pd and Pt) catalysts with loadings of <0.73 wt.% (Ardiyanti et al., 2011). All noble metal catalysts showed higher HDO activities per gram of metal than $CoMo/Al_2O_3$ catalysts. Although noble transition metals are seen as promising catalysts for high pressure HDO, their high cost, low availability and low resistance towards poisoning make them unsuitable in industrial applications (Bridgwater, 2010).

Non-noble transition metal catalysts such as Ni, Fe, Cu and Co have been studied for high pressure HDO due to their low cost and availability. However, these catalysts are generally much less active for HDO than noble transition metal catalysts. Inexpensive nickel-based catalysts have been extensively studied as they are highly active for hydrogenation (Zhang et al., 2013). The addition of copper facilitates the reduction of Ni at lower temperatures (Rogatis et al., 2009) and decreases coking (Lee et al. 2004). Higher reaction temperatures (>300 °C) and higher metal loadings (>20 wt.%) compared to noble based metals are required for high process efficiency, thereby increasing the upgrading cost. For example, Yakovlev et al. investigated 38 wt. % Ni and NiCu supported on SiO_2, Al_2O_3, CeO_2, ZrO_2 and CeO_2-ZrO_2 for HDO of anisole and reported higher activity for the bimetallic NiCu catalysts compared to the monometallic Ni catalysts (Yakovlev et al., 2009). Although noble and non-noble transition

metal catalysts are active for high pressure HDO, they fully saturate aromatic rings which is undesirable due to the large consumption of H_2, significantly increasing the cost of upgrading (Elliott, 2007). For example, Elliot et al. used hydrogen in excess of 35-420 mol H_2 per kg bio-oil for HDO of a real pyrolysis bio-oil using Pd/C whereas only 25 mol H_2 per kg bio-oil was theoretically required for complete deoxygenation (Elliott et al., 2009);Venderbosch et al., 2010).

2.11   Low Pressure Hydrodeoxygenation

Low pressure HDO generally does not lead to hydrogenation of aromatic rings, thus consuming significantly less hydrogen than high pressure HDO (Jin et al., 2019). Arenes such as benzene, toluene and xylene (BTX) also have higher octane numbers than aliphatic hydrocarbons and are the building blocks of a wide range of materials including plastics, detergents, drugs, dyes, lubricants and pesticides (Sirous-Rezaei et al., 2018). Traditionally, BTXs are produced from naphtha reforming (C_6–C_{12} over Pt/Al_2O_3) in a petroleum refinery. The current process for converting lignin to BTX involves pyrolysis of lignin, followed by deoxygenation via zeolite cracking; however, BTX yields are low and deactivation of the acidic catalyst is rapid (Sirous-Rezaei et al., 2018). Low pressure HDO can therefore serve as the future supply of BTX, mitigating dependence on fossil fuels and improving the economic viability of bio-refineries. Low pressure HDO could also be integrated in pre-existing fast pyrolysis systems, unlike conventional HDO which requires construction of special high-pressure equipment. Lastly, low pressure reactors are safer to operate.

Low pressure HDO typically operates at moderate to high temperatures (up to 565 °C) with the most prevalent temperature being 300 °C, and at low or atmospheric pressures (Pourzolfaghar et al., 2018). The catalyst should be able to activate molecular hydrogen and selectively cleave $C_{aromatic} - O$ bonds without hydrogenating the aromatic rings. Furthermore, the catalyst should be able to tolerate the high operating temperature, be resistant to deactivation by coking and water poisoning, and be inexpensive and environmentally friendly. Various types of catalysts have been studied for the vapor phase HDO of model compounds including noble metals, base metals and base metal phosphides, carbides and oxides.

2.12 Catalysts used for Low Pressure Hydrodeoxygenation

2.12.1 Noble Metals

Noble metals are an attractive catalyst choice because of their high activities for HDO reactions. Gao et al. tested four noble metal catalysts (Pt, Pd, Rh and Ru) supported on carbon at atmospheric pressure for the HDO of guaiacol (Gao et al., 2014). Pt was found to be most active and stable at 300 °C, as conversion was around 90 %. Zanuttini et al. studied atmospheric HDO of m-cresol with 1.7 wt.% Pt/Al_2O_3 in a fixed bed reactor at 300 °C and achieved a high conversion (84%) and toluene selectivity (77%) (Zanuttini et al., 2013). Nimmanwudipong, Runnebaum et al. studied the conversion of guaiacol catalyzed by 1 wt.% Pt supported on γ-Al_2O_3 with the main products being catechol, phenol and 3-methylcatechol, and inferred that the metal catalyzes the hydrodeoxygenation and hydrogenation reactions and the acidic alumina support catalyzes the transalkylation reactions (Nimmanwudipong, Runnebaum, et al., 2011). One study compared the performance of Pt/SiO_2, Pt/HBeta and HBeta catalysts in HDO of anisole; it was found that both transalkylation and HDO are achieved at significantly higher rates over the strongly acidic zeolite-supported catalyst, leading to the formation of BTX with lower H_2 consumption and a significant reduction in carbon losses, in comparison to the Pt/SiO_2 and HBeta catalysts (Zhu et al., 2011). However, another study concluded that although basic supports do not catalyze transalkylation reactions, they deactivate at slower rates and have higher conversion efficiencies compared to acidic ones, as deoxygenated product selectivities were 70% and 30% for the reactions using Pt/MgO and Pt/γ-Al_2O_3, respectively (Nimmanwudipong et al., 2012). Runnenaum et al. studied low pressure HDO of the bio-oil model compounds, guaiacol, anisole, 4-methylanisole and cyclohexanone, catalyzed by 1 wt. % Pt/Al_2O_3 at 300 °C and, in addition to HDO, they observed C – O bond cleavage that did not remove oxygen from the reactant, thus increasing the H_2 consumption (Runnebaum et al., 2012). Another study used Pt/SiO_2 for the HDO of m-cresol and found toluene to be the major product (Nie & Resasco, 2014). Although the ring-saturated compounds, 3-methylcyclohexanone and 3-methylcyclohexanol, were found to exist in an equilibrium with m-cresol, the ring saturated deoxygenated product, methylcyclohexane, was observed in very low yield. Therefore, undesirable hydrogenation/dehydrogenation reactions took place at a faster rate than the HDO reactions. Although noble metals have high activities for low pressure HDO, their high cost and limited availability prevent their use on an industrial

scale, as previously mentioned. Furthermore, noble metal catalysts are more prone to hydrogenation of the aromatic ring, thus increasing the costly hydrogen consumption.

2.12.2   Transition Metal Carbides/Phosphides

Transition metal carbides and phosphides have been used in hydroprocessing (HDS and HDN) processes for several decades, thus inspiring their application in HDO. These catalysts have been reported to exhibit hydrotreating activities similar to MoS_2-based catalysts (Furimsky, 2003; Oyama, 2003; Oyama et al., 2009) and have catalytic properties similar to noble metals (Hwu & Chen, 2005; Kelly et al., 2012; Oyama, 1992). Metal carbides such as Mo_2C are reported to possess bifunctional properties, unlike noble metal catalysts, requiring a support to activate the oxygenated molecule (Sullivan & Bhan, 2016; Lee, Wang, Zheng, et al., 2014). Lee et al. investigated anisole HDO over Mo_2C at atmospheric pressure and low temperatures (150 – 250 °C) and obtained >90% benzene selectivity (Lee, Wang, Wu, et al., 2014). In a comparative study, Mo_2C was applied for HDO of a phenolic mixture with the catalyst displaying >90% arene selectivity (Chen et al., 2016). Zhao et al. compared the performance of a series of phosphide catalysts, including Fe_2P/SiO_2, Co_2P/SiO_2, Ni_2P/SiO_2, MoP/SiO_2 and WP/SiO_2 for the gas phase HDO of guaiacol (Zhao et al., 2011). Ni_2P/SiO_2 displayed the highest turnover frequency and benzene selectivity (60%) of all the catalysts tested. Kinetic measurements indicate that the high benzene selectively is attributed to dehydration/hydrogenation reactions as oppose to direct C – O bond cleavage. Although transition metal carbides and phosphides are active for HDO at low pressures, surface oxidation (via water) causes deactivation, as the metal carbides and phosphides are converted to inactive metal oxides or oxy-carbides and oxy-phosphides (Ruddy et al., 2014). They are also typically synthesized via temperature programmed reduction (TPR) methods which requires high reaction temperatures and long reaction times.

2.12.3   Base Metals

Base metals such as Fe, Ni, and Mo are promising catalysts for selective HDO in the gas phase as they are generally oxophilic, inexpensive and environmentally friendly. Oxophilicity is defined as the tendency to form oxides and is related to the reactivity with removing oxygen from oxygenated aromatic compounds. A study by Tan et al. investigated the conversion of

anisole at atmospheric pressure over Fe, Ru and Pt supported on inert SiO_2 (Tan et al., 2017). Phenol and benzene were sequentially formed over the noble metal-based catalysts, whereas there was no phenol detected with benzene being the only major product over the most oxophillic catalyst tested, Fe/SiO_2. Based on DFT calculations, they concluded that the higher the oxophilicity of a metal catalyst, the lower the energy barrier for direct $C – O$ bond cleavage and the higher the energy barrier for hydrogenation reactions. A separate DFT study confirmed this by indicating that, compared to Pd, the more oxophillic Fe metal interacts with oxygen groups of guaiacol to a greater degree, resulting in a greater distortion of the $C – O$ bonds and therefore a lower energy barrier for direct $C – O$ bond cleavage (Hensley et al., 2016). However, if the metal is extremely highly oxophillic, as is the case for tungsten, then it is not readily reducible and oxygen vacancies cannot be created (Zhang et al., 2020).

2.12.4   Base Metal Oxides

Reducible base metal oxides such as MoO_3 have been widely used in catalysis due to their unique redox properties and are commonly used to catalyze selective oxidation reactions. For example, iron molybdate is used to catalyze the oxidation of methanol to formaldehyde, and bismuth molybdate catalyzes propylene oxidation to acrolein and ammoxidation of propene to acrylonitrile (Cheng, 1996; Pudar et al., 2007; Pudar et al., 2010). It is believed that these oxidation reactions occur via a redox or Mars-van Krevelen mechanism (Bamroongwongdee et al., 2008). The first step of the mechanism involves adsorption of the reactant to the catalyst surface. Subsequently, a reaction takes place between the adsorbate and an oxygen from the lattice of the catalyst, forming a partially oxidized product. Next, the product desorbs from the catalyst, leaving an oxygen vacancy at the surface. Finally, the vacancy is re-oxidized by O_2, returning the catalyst to its original state. By the principle of microscopic reversibility, the metal oxide catalysts that are active for oxidization reactions will also be active for hydrodeoxygenation reactions.

DFT calculations have shown that HDO of acrolein to propene and acetaldehyde to ethylene are thermodynamically favourable over MoO_3 (Mei et al., 2011; Prasomsri et al., 2013). Prasomsri et al. screened five reducible metal oxides for low pressure HDO of acetone (V_2O_5, Fe_2O_3, CuO, WO_3 and MoO_3) and found that MoO_3 featured the highest reactivity (80%) and selectivity (98%) to deoxygenated hydrocarbon products (Prasomsri et al., 2013). Subsequent

HDO experiments were performed over MoO_3 with other bio-oil model compounds, including other ketones (2-hexanone and cyclohexanone), furanics (2-methylfuran and 2,5-dimethylfuran) and an aromatic lignin model compound (anisole). In every case, MoO_3 was active for HDO with deoxygenated hydrocarbon selectivities exceeding 97%. Furthermore, MoO_3 did not result in saturation of the hydrocarbons, with the products being olefins and aromatics. MoO_3 exhibited a high tolerance to water poisoning and to coking, with <1% of the carbon being lost as coke. Notably, MoO_3 selectively cleaves the $C_{aromatic} - O$ bonds over the weaker $C_{aliphatic} - O$ bonds and minimizes carbon loss of compounds containing methoxy groups by promoting transmethylation reactions of the methanol by-product with the aromatic ring to form alkylbenzenes (Prasomsri et al., 2014). Nolte et al., performed HDO of cellulose, lignin and corn stover pyrolysis vapours over MoO_3 at low H_2 pressures and obtained high yields of linear alkanes and aromatics (up to 90 %) (Nolte et al., 2015). These studies suggest that MoO_3 has properties that make it suitable for use as an HDO catalyst; it's relatively inexpensive, active at moderate temperatures (200–400 °C) and low H_2 pressures while generally being more hydrogen efficient by minimizing hydrogenation reactions.

2.13   Catalyst Support Type

The catalyst support material has been shown to influence the catalyst's stability, activity and selectivity towards certain products. Typically, high surface area mesoporous supports are used to enhance the dispersion of active catalytic species, increasing the available active sites for the reaction to occur (Li et al., 2018). Supports with specific acid sites have been shown to catalyze HDO reactions, such as transalkylation (Saidi et al., 2014), dehydration and hydrogenolysis reactions (Mirodatos et al., 2009). However, acidic support sites create positions for coke formation. Alumina is one of the most commonly used supports in catalytic processes due to its high surface area, low cost and availability (He & Wang, 2012). However, alumina is highly acidic, making it susceptible to deactivation by coke formation. Moreover, since bio-oil contains ~30 wt. % water, it may not be a suitable support for HDO, as alumina's been reported to transform into boehmite in the presence of large amounts of water (Lødeng et al., 2017; Elliott, 2007; Venderbosch et al., 2010; Laurent & Delmon, 1994). Alternatively, less acidic and more hydrothermally stable metal oxides such as SiO_2, ZrO_2, TiO_2 and CeO_2 have been used as supports (Valencia et al., 2019; Gonçalves et al., 2017; Ranga et al., 2018; Phan et al., 2015; Lødeng et al., 2017; Chary et al., 2004).

2.14 General Deactivation Mechanism of HDO Catalysts

Lifetime is a key parameter to evaluate catalysts. Mechanisms of catalyst deactivation in HDO include coking, metal deposition, sintering and poisoning by water, phosphorous and nitrogen. The extent of these deactivation routes depend on the type of catalyst, feed composition and reaction operating conditions, though carbon deposition has proven to be the main cause of catalyst deactivation (Furimsky & Massoth, 1999). The formation of carbon occurs via polymerization and polycondensation reactions on the catalyst surface, forming polyaromatic species which plug pores and block the active sites. Lignin derived compounds, such as anisole, are prone to coking due to their high concentrations of unsaturated hydrocarbon elements (i.e. aromatics), which have significantly stronger interactions with the catalyst's surface compared to saturated hydrocarbons (Kopinke et al., 1993). It has also been inferred that compounds with more than one oxygen atom have higher affinities for coke formation (Mortensen et al., 2011). Furthermore, studies indicate a positive correlation between the rate of coking and the acidity of the catalyst (Saidi et al., 2014). Catalysts with higher acidity dissociate hydrogen protons to form carbocations, precursors to carbon deposition. Coke formation can, however, be minimized by lowering the reaction temperature and increasing the hydrogen partial pressure (Furimsky & Massoth, 1999). Therefore, low pressure HDO systems are more prone to coking compared to liquid phase HDO processes.

2.15 Catalytic Active Site of MoO_3 in Hydrodeoxygenation

Gonçalves et al. found a correlation between the number of oxygen vacancies on MoO_X on various supports and the direct deoxygenation reaction rate; they determined that partially reduced Mo species (Mo^{5+}) play a vital role for directly cleaving the $C_{aromatic} - O$ bonds, thus producing arenes (Gonçalves et al., 2017; Valencia et al., 2019). Whiffen et al. obtained a high conversion for the HDO of cresol over a partially reduced Mo oxide and concluded that it was due to the Brønsted acid sites and the formation of oxygen vacancies (Whiffen & Smith, 2010). Prasomsri et al. investigated the low pressure HDO of lignin-derived model compounds over bulk MoO_3 at temperatures ranging from 300 to 400 °C and observed an induction period whereby pristine MoO_3 (i.e. Mo^{6+} state) required <2 h to display full catalytic activity (Prasomsri et al., 2014). Pre-reducing MoO_3 with H_2 for 3 h eliminated the induction period and an oxycarbohydride ($MoO_xC_yH_z$) phase was formed after introduction of a carbon source

(i.e. the model compound m-cresol). They therefore proposed that Mo^{5+} Lewis acid sites, which are generated from either the carburization of MoO_3 to $MoO_xC_yH_z$ or from the reduction of MoO_3 to MoO_{3-x}, are the active sites responsible for the enhanced activity (Prasomsri et al., 2014; Bouchy et al., 2000; Lødeng et al., 2017; Zhang, Tang, et al., 2019). However, it's possible to over-reduce MoO_3, as was found by the authors, where the catalyst deactivated due to the formation of inactive MoO_2 (i.e. Mo^{4+} state). Over-reduction of MoO_3 at 350 °C resulted in the conversion decreasing from above 80% to about 60% after 7 h of operation (Prasomsri et al., 2014). However, they demonstrated that the over-reduced catalyst can be regenerated by calcination without losing its original activity. It was hypothesized that oxygen vacancies (MoO_{3-x}) activate the C – O bond and the lattice carbon in $MoO_xC_yH_z$ plays a critical role in stabilizing the active Mo^{5+} state, thereby slowing the reduction to Mo^{4+} and prolonging the activity of the catalyst. This is in agreement with observations by Delporte et al., where the reactant's carbon atoms filled the oxygen vacancies to form an oxycarbohydride phase, slowing the MoO_2 rate of formation (Delporte et al., 1995). Ranga et al. carburized MoO_3/ZrO_2 using a H_2/CH_4 mixture and found that it generated defects in the Mo oxide structure with increased amounts of the lower Mo oxidation state, Mo^{5+} (Ranga et al., 2018). They performed HDO of anisole over this catalyst and concluded that the Mo^{5+} oxidation state is closely related to the catalytic activity. Murugappan et al. used operando near-ambient pressure (NAP) XPS to study the oxidation states of MoO_3 during the HDO of anisole at 320 °C and at low H_2 pressures (≤ 0.1 kPa) (Murugappan et al., 2018). The technique revealed that the Mo species transitioned between 5+ and 6+ oxidation states during the reaction, thus providing evidence for the proposed oxygen-vacancy driven mechanism.

It is believed that these HDO reactions over bulk and supported MoO_3 catalysts proceed through a reverse Mars-van Krevelen mechanism which involves two concerted cycles: (1) hydrogen reduction of the catalyst surface and (2) oxidation of the catalyst surface by the oxygenated molecule, as illustrated in Figure 2.6 (Gonçalves et al., 2017; Rellán-Piñeiro & López, 2018; Moberg et al., 2010). First, an oxygen vacancy is formed via adsorption of H_2, followed by a proton transfer and finally the release of H_2O (Prasomsri et al., 2013). The oxygen of the reactant then adsorbs into the vacancy, i.e. a coordinatively unsaturated Mo site (i.e. Mo^{5+}), which weakens the $C_{aromatic}$ – O bond and lowers the energy barrier for direct deoxygenation. The next step is activation of H_2, which occurs by heterolytic dissociation. The

addition of a hydride species on the aromatic carbon bearing the oxygen results in cleavage of the $C_{aromatic} - O$ bond, thus forming the deoxygenated product. The catalytic cycle is complete as the adsorbed oxygen becomes part of the catalyst surface. Prasomsri et al. demonstrated that deactivation can be minimized by tuning the hydrogen partial pressure, thus regenerating the oxygen vacancies (Prasomsri et al., 2013).
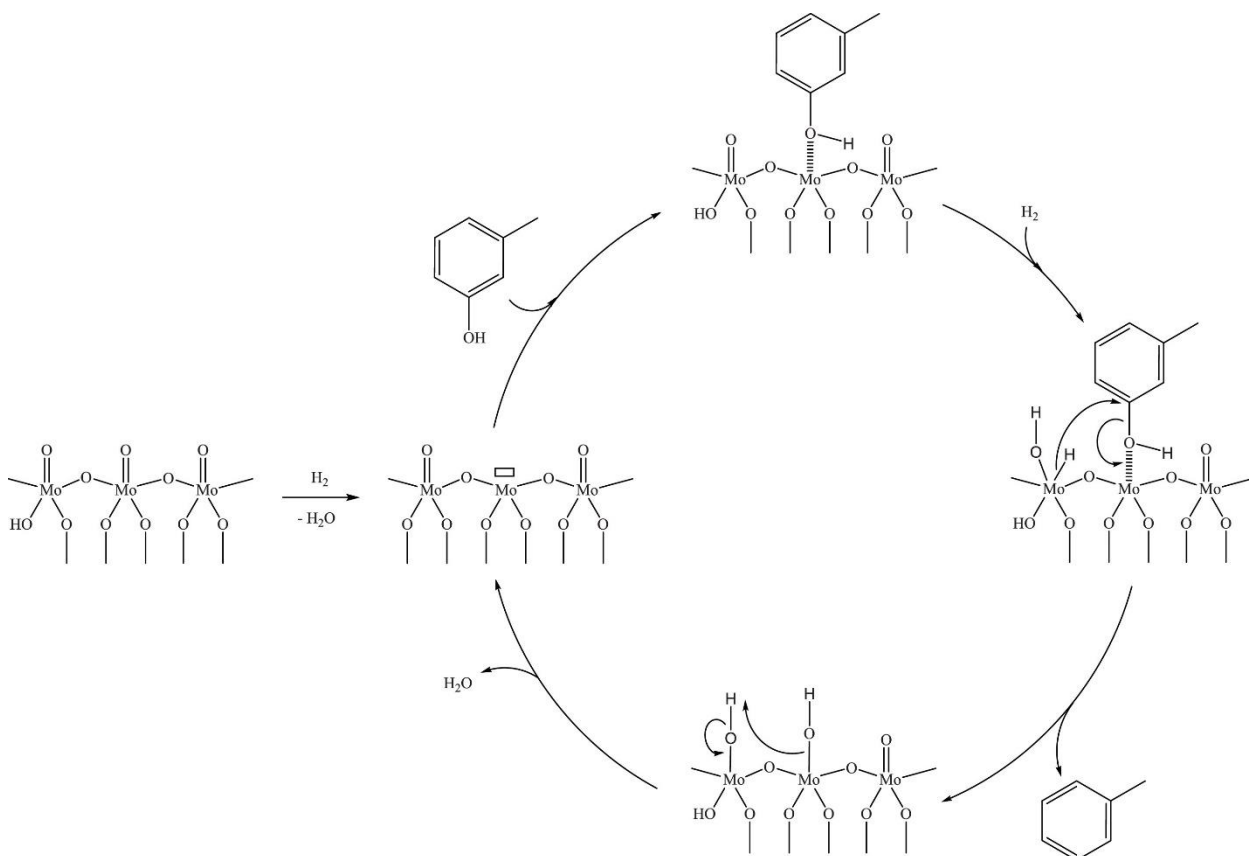
Figure 2.6 Mechanism of the direct deoxygenation (DDO) route of m-cresol on a schematic molybdenum oxide site species (Gonçalves et al., 2017)

2.16   MoO$_3$ Supported Catalyst Formulation Parameters

Shetty et al. studied MoO$_3$ supported on different oxides (i.e. γ-Al$_2$O$_3$, SiO$_2$, ZrO$_2$, TiO$_2$ and CeO$_2$) for the atmospheric HDO of cresol at 320 °C (Shetty et al., 2015). They found that the supports played two key roles: 1) preventing the over-reduction of MoO$_3$ to lower oxidation states and 2) allowing the coordinately unsaturated sites to be formed at lower temperatures. Supporting MoO$_3$, particularly onto TiO$_2$ or ZrO$_2$, improved the catalyst stability and reactivity by stabilizing the proposed active site (Mo^{5+}), whereas the unsupported Mo more readily reduced to the less reactive Mo^{4+} and Mo^0 oxidation states. MoO$_3$ supported on γ-Al$_2$O$_3$ or

23

SiO$_2$ exhibited a higher tendency to form coke, which was attributed to the presence of surface acid sites. The lowest activity was observed with the CeO$_2$ supported catalyst, due to the facile transport of oxygen through the bulk CeO$_2$ to the Mo phase. A comparative study found that the support prevents the over-reduction of Mo^{6+} only at sub-monolayer MoO$_X$ dispersions (Shetty et al., 2017). Gonçalves et al. investigated HDO of m-cresol over supported MoO$_3$ catalysts and found that the reducibility of the molybdenum species depends on the support material used and correlates to the HDO activity, i.e. MoO$_3$/Al$_2$O$_3$ > MoO$_3$/SBA–15 > MoO$_3$/SiO$_2$ (Gonçalves et al., 2017).

The metal/support ratio can also affect the supported catalysts performance. Shetty et al. evaluated the vapour-phase HDO of anisole at 320 °C, and H$_2$ pressures ≤ 0.101 MPa over MoO$_3$ supported on ZrO$_2$ with loadings ranging from 1 to 36 wt. % (Shetty et al., 2017). HDO activity increased proportionally with an increase in loading until the monolayer coverage (~15 wt. %) was achieved, followed by a decrease in activity. Once the monolayer is exceeded, crystallites of MoO$_3$ and Zr(MoO$_4$)$_2$ are formed, which undergo over-reduction to less reactive MoO$_2$ (Shetty et al., 2017; El-Sharkawy et al., 2007; Tsilomelekis & Boghosian, 2010; Chary et al., 2004). At very low loadings, isolated MoO$_x$ species are formed over the support and increasing the loading results in oligomeric MoO$_x$ domains, which are more reducible and reactive towards HDO than isolated MoO$_x$ domains. Lødeng et al. studied the liquid phase HDO over a series of molybdenum oxide catalysts with loadings of 7, 15, and 25 wt. % and found that the intermediate Mo loading oxide catalyst showed superior performance (Lødeng et al., 2017). Ranga et al. also used a series of Mo loadings (7, 12 and 19 wt. %) on zirconia for the HDO of anisole at gas phase conditions (Ranga et al., 2018). The product selectivity and stability were the same regardless of the Mo loading used, yet it did have an impact on the activity. The 12 wt.% loading had the largest anisole conversion and the 7 wt. % Mo catalyst had the highest TOF (0.15 s^{-1}). We therefore selected a 10 wt.% loading to maximize the number of Mo^{5+} species, while not exceeding monolayer coverage.

References

Adjaye, J. D., Katikaneni, S. P. R., & Bakhshi, N. N. (1996). Catalytic conversion of a biofuel to hydrocarbons : effect of mixtures of HZSM-5 and silica-alumina catalysts on product distribution. *Fuel Processing Technology*, *48*, 115–143.

Akhtar, J., Saidina, N., & Wood, P. (2012). A review on operating parameters for optimum liquid oil yield in biomass pyrolysis. *Renewable and Sustainable Energy Reviews*, *16*, 5101–5109.

Alalwan, H. A., Alminshid, A. H., & Aljaafari, H. A. S. (2019). Promising evolution of biofuel generations . Subject review. *Reinforced Plastics*, *28*, 127–139. https://doi.org/10.1016/j.ref.2018.12.006

Ardiyanti, A. R., Gutierrez, A., Honkela, M. L., Krause, A. O. I., & Heeres, H. J. (2011). Hydrotreatment of wood-based pyrolysis oil using zirconia-supported mono- and bimetallic (Pt , Pd , Rh) catalysts. *"Applied Catalysis A, General," 407*(1–2), 56–66. https://doi.org/10.1016/j.apcata.2011.08.024

Azadi, P., Inderwildi, O. R., Farnood, R., & King, D. A. (2013). Liquid fuels , hydrogen and chemicals from lignin : A critical review. *Renewable and Sustainable Energy Reviews*, *21*, 506–523. https://doi.org/10.1016/j.rser.2012.12.022

Babu, B. V. (2008). Biomass pyrolysis : a state-of- the-art review. *Biofuels, Bioproducts and Biorefining*, *2*, 393–414. https://doi.org/10.1002/bbb

Badawi, M., Paul, J. F., Cristol, S., Payen, E., Romero, Y., Richard, F., Brunet, S., Lambert, D., Portier, X., Popov, A., Kondratieva, E., Goupil, J. M., Fallah, J. El, Gilson, J. P., Mariey, L., Travert, A., & Maugé, F. (2011). Effect of water on the stability of Mo and CoMo hydrodeoxygenation catalysts : A combined experimental and DFT study. *Journal of Catalysis*, *282*(1), 155–164. https://doi.org/10.1016/j.jcat.2011.06.006

Baddour, F. G., Witte, V. A., Nash, C. P., Gri, M. B., Ruddy, D. A., & Schaidle, J. A. (2017). Late-Transition-Metal-Modified β - Mo2C Catalysts for Enhanced Hydrogenation during Guaiacol Deoxygenation. *ACS Sustainable Chemistry and Engineering*, *5*, 11433−11439. https://doi.org/10.1021/acssuschemeng.7b02544

Balat, M., Balat, M., Kırtay, E., & Balat, H. (2009). Main routes for the thermo-conversion of biomass into fuels and chemicals . Part 1 : Pyrolysis systems. *Energy Conversion and Management*, *50*(12), 3147–3157. https://doi.org/10.1016/j.enconman.2009.08.014

Bamroongwongdee, C., Shannon, Æ. M., & Carley, Æ. A. (2008). The Selective Oxidation of Methanol on Iron Molybdate Catalysts. *Topics in Catalysis*, *48*, 158–165. https://doi.org/10.1007/s11244-008-9058-3

Bertero, M., Puente, G. De, & Sedran, U. (2012). Fuels from bio-oils : Bio-oil production from different residual sources , characterization and thermal conditioning. *Fuel*, *95*, 263–271. https://doi.org/10.1016/j.fuel.2011.08.041

Bouchy, C., Pham-huu, C., Heinrich, B., Chaumont, C., & Ledoux, M. J. (2000). Microstructure and Characterization of a Highly Selective Catalyst for the Isomerization of Alkanes : A Molybdenum Oxycarbide. *Journal of Catalysis*, *190*, 92–103. https://doi.org/10.1006/jcat.1999.2741

Bridgwater, A. V. (2010). Hydrotreating for bio-oil upgrading. In M. Crocker (Ed.), *Thermochemical Conversion of Biomass to Liquid Fuels and Chemicals* (p. 288). RCS.

Bridgwater, A V. (2015). Pyrolysis of Biomass. In W. van Swaaij, S. Kersten, & W. Palz (Eds.), *Biomass Power for the World* (1st ed., pp. 474–479). Pan Stanford Publishing.

Bridgwater, Anthony V. (2004). Biomass fast pyrolysis. *Thermal Science*, *8*(2), 21–49.

Buck, V. De, Polanska, M., & Impe, J. Van. (2020). Modeling Biowaste Biorefineries : A Review. *Frontiers in Sustainable Food Systems*, *4*(February). https://doi.org/10.3389/fsufs.2020.00011

Chang, C. D., & Silvestri, A. J. (1977). The Conversion of Methanol and Other O-Compounds to Hydrocarbons over Zeolite Catalysts. *Journal of Catalysis*, *47*, 249–259.

Chary, K. V. R., Rajender, K., Kishan, G., Niemantsverdriet, J. W., & Mestl, G. (2004). Structure and catalytic properties of molybdenum oxide catalysts supported on zirconia. *Journal of Catalysis*, *226*, 283–291. https://doi.org/10.1016/j.jcat.2004.04.028

Chen, C., Lee, W., & Bhan, A. (2016). Mo2C catalyzed vapor phase hydrodeoxygenation of lignin-derived phenolic compound mixtures to aromatics under ambient pressure. *Applied Catalysis A : General*, *510*, 42–48.

Cheng, W. (1996). Methanol and Formaldehyde Oxidation Study over Molybdenum Oxide. *Journal of Catalysis*, *485*(158), 477–485.

Delporte, P., Meunier, F., Pham-huu, C., Vennegues, P., Ledoux, M. J., & Guille, J. (1995). Physical characterization of molybdenum oxycarbide catalyst ; TEM, XRD and XPS. *Catalysis Today*, *23*, 251–267.

Den, W., Sharma, V. K., Lee, M., & Nadadur, G. (2018). Lignocellulosic Biomass

Transformations via Greener Oxidative Pretreatment Processes : Access to Energy and Value-Added Chemicals. *Frontiers in Chemistry*, *6*, 1–23. https://doi.org/10.3389/fchem.2018.00141

Eijck, J. Van, Batidzirai, B., & Faaij, A. (2014). Current and future economic performance of first and second generation biofuels in developing countries. *Applied Energy*, *135*, 115–141. https://doi.org/10.1016/j.apenergy.2014.08.015

El-Sharkawy, E. A., Khder, A. S., & Ahmed, A. I. (2007). Structural characterization and catalytic activity of molybdenum oxide supported zirconia catalysts. *Microporous and Mesoporous Materials*, *102*(1–3), 128–137. https://doi.org/10.1016/j.micromeso.2006.12.037

Elliott, D. C. (2007). Historical Developments in Hydroprocessing Bio-oils. *Energy & Fuels*, *7*, 1792–1815. https://doi.org/10.1021/ef070044u

Elliott, D. C., Hart, T. R., Neuenschwander, G. G., Rotness, L. J., & Zacher, A. H. (2009). Catalytic Hydroprocessing of Biomass Fast Pyrolysis Bio-oil to Produce Hydrocarbon Products. *Environmental Progress & Sustainable Energy (Vol.28, 28*(3), 441–449. https://doi.org/10.1002/ep

Feliczak-guzik, A., Szczyglewska, P., Jaroniec, M., & Nowak, I. (2020). Ruthenium-containing SBA-12 catalysts for anisole hydrodeoxygenation. *Catalysis Today*. https://doi.org/10.1016/j.cattod.2020.03.006

Furimsky, E. (2003). Metal carbides and nitrides as potential catalysts for hydroprocessing. *Applied Catalysis A, General*, *240*, 1–28.

Furimsky, E., & Massoth, F. E. (1999). Deactivation of hydroprocessing catalysts. *Catalysis Today*, *52*, 381±495.

Gao, D., Schweitzer, C., Hwang, H. T., & Varma, A. (2014). Conversion of Guaiacol on Noble Metal Catalysts : Reaction Performance and Deactivation Studies. *Industrial & Engineering Chemistry Research*, *53*, 18658−18667. https://doi.org/10.1021/ie500495z

Gonçalves, V. O. O., Ciotonea, C., Arrii-Clacens, S., Guignard, N., Roudaut, C., Rousseau, J., Clacens, J. M., Royer, S., & Richard, F. (2017). Effect of the support on the hydrodeoxygenation of m-cresol over molybdenum oxide based catalysts. *Applied Catalysis B: Environmental*, *214*, 57–66. https://doi.org/10.1016/j.apcatb.2017.05.003

Gust, S. (1997). Combustion Experiences of Flash Pyrolysis Fuel in Intermediate Size Boilers. In D. G. B. (Eds. . Bridgwater, A.V., Boocock (Ed.), *Developments in*

Thermochemical Biomass Conversion (pp. 481–488). Springer, Dordrecht. https://doi.org/https://doi.org/10.1007/978-94-009-1559-6_37

Gutierrez, A., Kaila, R. K., Honkela, M. L., Slioor, R., & Krause, A. O. I. (2009). Hydrodeoxygenation of guaiacol on noble metal catalysts. *Catalysis Today*, *147*, 239–246. https://doi.org/10.1016/j.cattod.2008.10.037

He, Z., & Wang, Z. (2012). Hydrodeoxygenation of model compounds and catalytic systems for pyrolysis bio-oils upgrading. *Catalysis for Sustainable Energy*, 28–52. https://doi.org/10.2478/cse-2012-0004

Hensley, A. J. R., Wang, Y., & Mcewen, J. (2016). Surface Science Adsorption of guaiacol on Fe (110) and Pd (111) from fi rst principles. *Surface Science*, *648*, 227–235. https://doi.org/10.1016/j.susc.2015.10.030

Hong, D., Miller, S. J., Agrawal, K., & Jones, C. W. (2010). Hydrodeoxygenation and coupling of aqueous phenolics over bifunctional zeolite-supported metal catalysts. *Chemical Communications*, *46*, 1038–1040. https://doi.org/10.1039/b918209h

Huber, G. W., Iborra, S., & Corma, A. (2006). Synthesis of Transportation Fuels from Biomass: Chemistry, Catalysts, and Engineering. *Chemical Reviews*, *106*(9), 4044–4098. https://doi.org/10.1021/cr068360d

Hwu, H. H., & Chen, J. G. (2005). Surface Chemistry of Transition Metal Carbides. *Chemical Reviews*, *105*, 185–212. https://doi.org/10.1021/cr0204606

Jin, W., Pastor-pérez, L., Shen, D., Sepúlveda-escribano, A., & Gu, S. (2019). Catalytic Upgrading of Biomass Model Compounds : Novel Approaches and Lessons Learnt from Traditional Hydrodeoxygenation – a Review. *ChemCatChem*, *11*, 1–38. https://doi.org/10.1002/cctc.201801722

Katikaneni, S. P. R., Adjaye, J. D., & Bakhshi, N. N. (1995). Performance of Aluminophosphate Molecular Sieve Catalysts for the Production of Hydrocarbons from Wood-Derived and Vegetable Oils. *Energy & Fuels*, *7*, 599–609. https://doi.org/10.1021/ef00054a021

Kelly, T. G., Chen, J. G., & Kelly, T. G. (2012). Metal overlayer on metal carbide substrate : unique bimetallic properties for catalysis and electrocatalysis. *Chemical Society Reviews*. https://doi.org/10.1039/c2cs35165j

Khromova, S. A., Smirnov, A. A., Bulavchenko, O. A., Saraev, A. A., Kaichev, V. V, Reshetnikov, S. I., & Yakovlev, V. A. (2014). General Anisole hydrodeoxygenation

over Ni – Cu bimetallic catalysts : The effect of Ni / Cu ratio on selectivity. *Applied Catalysis A: General*, *470*, 261–270. https://doi.org/10.1016/j.apcata.2013.10.046

Kim, J., Hwang, H., Park, J., Oh, S., & Choi, J. W. (2014). Predicting structural change of lignin macromolecules before and after heat treatment using the pyrolysis-GC / MS technique. *Journal of Analytical and Applied Pyrolysis*, *110*, 305–312. https://doi.org/10.1016/j.jaap.2014.09.020

Kopinke, F.-D., Zimmermann, G., Reyniers, G., & Froment, G. F. (1993). Relative Rates of Coke Formation from Hydrocarbons in Steam Cracking of Naphtha. 2. Paraffins, Naphthenes, Mono-, Di-, and Cycloolefins, and Acetylenes. *Industrial & Engineering Chemistry Research*, *32*(1), 56–61. https://doi.org/10.1021/ie00013a009

Laurent, E., & Delmon, B. (1994). Influence of Water in the Deactivation of a Sulfided NiMo / y-AI2O3 Catalyst during Hydrodeoxygenation. *Journal of Catalysis*, *146*, 281–291.

Laurichesse, S., & Avérous, L. (2014). Progress in Polymer Science Chemical modification of lignins : Towards biobased polymers. *Progress in Polymer Science*, *39*(7), 1266–1290. https://doi.org/10.1016/j.progpolymsci.2013.11.004

Lazzari, E., Schena, T., Tatiane, C., Pereira, G., Elisabete, M., Andrea, C., Cardoso, L., Assis, R., & Bastos, E. (2016). Production and chromatographic characterization of bio-oil from the pyrolysis of mango seed waste. *Industrial Crops & Products*, *83*, 529–536. https://doi.org/10.1016/j.indcrop.2015.12.073

Lee, W., Wang, Z., Wu, R. J., & Bhan, A. (2014). Selective vapor-phase hydrodeoxygenation of anisole to benzene on molybdenum carbide catalysts. *Journal of Catalysis*, *319*, 44–53. https://doi.org/10.1016/j.jcat.2014.07.025

Lee, W., Wang, Z., Zheng, W., Vlachos, D. G., & Bhan, A. (2014). Vapor phase hydrodeoxygenation of furfural to 2-methylfuran on molybdenum carbide catalysts. *Catalysis Science & Technology*, *4*, 2340–2352. https://doi.org/10.1039/c4cy00286e

Leibbrandt, N. H., Knoetze, J. H., & Go, J. F. (2011). Comparing biological and thermochemical processing of sugarcane bagasse : An energy balance perspective. *Biomass and Bioenergy*, *35*, 2117–2126. https://doi.org/10.1016/j.biombioe.2011.02.017

Li, C., Zhao, X., Wang, A., Huber, G. W., & Zhang, T. (2015). Catalytic Transformation of Lignin for the Production of Chemicals and Fuels. *Chemical Reviews*, *115*, 11559−11624. https://doi.org/10.1021/acs.chemrev.5b00155

Li, H., & Mcdonald, A. G. (2014). Fractionation and characterization of industrial lignins. *Industrial Crops and Products*, *62*, 67–76.

Li, K., Wang, R., & Chen, J. (2011). Hydrodeoxygenation of Anisole over Silica-Supported Ni2P , MoP , and NiMoP Catalysts. *Energy & Fuels*, *25*, 854–863. https://doi.org/10.1021/ef101258j

Li, Y., Fu, J., & Chen, B. (2017). Highly selective hydrodeoxygenation of anisole, phenol and guaiacol to benzene over nickel phosphide. *RCS Advances*, 15272–15277. https://doi.org/10.1039/c7ra00989e

Liu, X., He, Y., Wang, S., & Zhang, Q. (2011). Preparation of MoO2 sub-micro scale sheets and their optical properties. *Journal of Alloys and Compounds*, *509*(SUPPL. 1), S408–S411. https://doi.org/10.1016/j.jallcom.2011.01.089

Lødeng, R., Ranga, C., Rajkhowa, T., Alexiadis, V. I., Bjørkan, H., Chytil, S., Svenum, I. H., Walmsley, J., & Thybaut, J. W. (2017). Hydrodeoxygenation of phenolics in liquid phase over supported MoO3 and carburized analogues. *Biomass Conversion and Biorefinery*, *7*(3), 343–359. https://doi.org/10.1007/s13399-017-0252-z

Mei, D., Karim, A. M., & Wang, Y. (2011). Density Functional Theory Study of Acetaldehyde Hydrodeoxygenation on MoO3. *The Journal of Physical Chemistry*, *115*, 8155–8164. https://doi.org/10.1021/jp200011j

Mercader, F. D. M., Groeneveld, M. J., Kersten, S. R. A., Way, N. W. J., Schaverien, C. J., & Hogendoorn, J. A. (2010). Production of advanced biofuels : Co-processing of upgraded pyrolysis oil in standard refinery units. *Applied Catalysis B, Environmental*, *96*(1–2), 57–66. https://doi.org/10.1016/j.apcatb.2010.01.033

Miguel, G. S., & Makibar, J. (2012). New Advances in the Fast Pyrolysis of Biomass. *Biobased Materials and Bioenergy*, *6*, 1–11. https://doi.org/10.1166/jbmb.2012.1209

Mirodatos, C., Geantet, C., Bui, V. N., & Toussaint, G. (2009). Co-processing of pyrolisis bio oils and gas oil for new generation of bio-fuels : ¨ acol and SRGO mixed feed Hydrodeoxygenation of guaı. *Catalysis Today*, *143*, 172–178. https://doi.org/10.1016/j.cattod.2008.11.024

Moberg, D. R., Thibodeau, T. J., Amar, F. G., & Frederick, B. G. (2010). Mechanism of hydrodeoxygenation of acrolein on a cluster model of MoO3. *Journal of Physical Chemistry C*, *114*(32), 13782–13795. https://doi.org/10.1021/jp104421a

Mohan, D., Pittman, C. U., & Steele, P. H. (2006). Pyrolysis of Wood / Biomass for Bio-Oil :

A Critical Review. *Energy and Fuels*, *20*, 848–889. https://doi.org/10.1021/ef0502397

Molino, A., Chianese, S., & Musmarra, D. (2016). Biomass gasification technology : The state of the art overview. *Journal of Energy Chemistry*, *25*(1), 10–25. https://doi.org/10.1016/j.jechem.2015.11.005

Moreau, C., Aubert, C., Durand, R., Zmimita, N., & Geneste, P. (1988). Structure-activity relationships in hydroprocessing of aromatic and heteroaromatic model compounds over sulphided NiO-MoO3/γ-Al2O3 and Nio-WO3/ γ -Al2O3 catalysts; chemical evidence for the existence of two types of catalytic sites. *Catalysis Today*, *4*(1), 117–131.

Moreau, C., Joffre, J., Saenz, C., & Geneste, P. (1990). Hydroprocessing of Substituted Benzenes over a Sulfided CoO-M oO3/~/-AI203Catalyst. *Journal of Catalysis*, *451*, 448–451.

Mortensen, P. M., Grunwaldt, J., Jensen, P. A., Knudsen, K. G., & Jensen, A. D. (2011). A review of catalytic upgrading of bio-oil to engine fuels. *Applied Catalysis A : General*, *407*, 1–19. https://doi.org/10.1016/j.apcata.2011.08.046

Murugappan, K., Anderson, E. M., Teschner, D., & Jones, T. E. (2018). Operando NAP-XPS unveils differences in MoO3 and Mo2C during hydrodeoxygenation. *Nature Catalysis*, *1*, 960–967.

Nie, L., & Resasco, D. E. (2014). Kinetics and mechanism of m-cresol hydrodeoxygenation on a Pt / SiO2 catalyst. *Journal of Catalysis*, *317*, 22–29. https://doi.org/10.1016/j.jcat.2014.05.024

Nimmanwudipong, T., Aydin, C., Browning, N. D., Block, D. E., & Gates, B. C. (2012). Selective Hydrodeoxygenation of Guaiacol Catalyzed by Platinum Supported on Magnesium Oxide. *Catalysis Letters*, *142*, 1190–1196. https://doi.org/10.1007/s10562-012-0884-3

Nimmanwudipong, T., Runnebaum, R. C., Block, D. E., & Gates, B. C. (2011). Catalytic conversion of guaiacol catalyzed by platinum supported on alumina: Reaction network including hydrodeoxygenation reactions. *Energy and Fuels*, *25*(8), 3417–3427. https://doi.org/10.1021/ef200803d

Nolte, M. W., Zhang, J., & Shanks, B. H. (2015). Ex situ hydrodeoxygenation in biomass pyrolysis using molybdenum oxide and low pressure hydrogen. *Green Chemistry*, *18*(1), 134–138. https://doi.org/10.1039/c5gc01614b

Oasmaa, A., & Czernik, S. (1999). Fuel Oil Quality of Biomass Pyrolysis Oils-State of the

Art for the End Users. *Energy and Fuels*, *13*, 914–921.

Oasmaa, A., Sipilä, K., Solantausta, Y., & Kuoppala, E. (2005). Quality Improvement of Pyrolysis Liquid: Effect of Light Volatiles on the Stability of Pyrolysis Liquids. *Energy & Fuels*, *19*(6), 2556–2561. https://doi.org/10.1021/ef0400924

Ohta, H., Yamamoto, K., Hayashi, M., Hamasaka, G., Uozumib, Y., & Watanabe, Y. (2012). Low temperature hydrodeoxygenation of phenols under ambient hydrogen pressure to form cyclohexanes catalysed by Pt nanoparticles supported on H-ZSM-5. *ChemComm*. https://doi.org/10.1039/x0xx00000x

Olcese, R. N., Bettahar, M., Petitjean, D., Malaman, B., Giovanella, F., & Dufour, A. (2012). Gas-phase hydrodeoxygenation of guaiacol over Fe / SiO2 catalyst. *Applied Catalysis B, Environmental*, *115–116*, 63–73. https://doi.org/10.1016/j.apcatb.2011.12.005

Oyama, S Ted. (2003). Novel catalysts for advanced hydroprocessing : transition metal phosphides. *Novel Catalysts for Advanced Hydroprocessing: Transition Metal Phosphides*, *216*, 343–352. https://doi.org/10.1016/S0021-9517(02)00069-6

Oyama, S Ted, Gott, T., Zhao, H., & Lee, Y. (2009). Transition metal phosphide hydroprocessing catalysts : A review. *Catalysis Today*, *143*, 94–107. https://doi.org/10.1016/j.cattod.2008.09.019

Oyama, Shigeo Ted. (1992). Preparation and Catalytic Properties of Transition Metal Carbides and Nitriles. *Catalysis Today*, *15*, 179–200. https://doi.org/10.1016/0920-5861(92)80175-M

Peters, J. E., Carpenter, J. R., & Dayton, D. C. (2015). Anisole and Guaiacol Hydrodeoxygenation Reaction Pathways over Selected Catalysts. *Energy & Fuels*, *29*, 909−916. https://doi.org/10.1021/ef502551p

Phan, B. M. Q., Ha, Q. L. M., Le, N. P., & Nimo-base, C. Á. S.-Á. (2015). Influences of Various Supports , γ -Al2O3 , CeO2 , and SBA-15 on HDO Performance of NiMo Catalyst. *Catalysis Letters*, *145*, 662–667. https://doi.org/10.1007/s10562-014-1412-4

Pourzolfaghar, H., Abnisa, F., Mohd, W., & Wan, A. (2018). Atmospheric hydrodeoxygenation of bio-oil oxygenated model compounds : A review. *Journal of Analytical and Applied Pyrolysis*, *133*, 117–127. https://doi.org/10.1016/j.jaap.2018.04.013

Prasomsri, T., Nimmanwudipong, T., & Román-Leshkov, Y. (2013). Effective hydrodeoxygenation of biomass-derived oxygenates into unsaturated hydrocarbons by

MoO3 using low H2 pressures. *Energy & Environmental Science*, *6*(6), 1643–1972. https://doi.org/10.1039/C3EE24360E

Prasomsri, T., Shetty, M., Murugappan, K., & Rom´an-Leshkov, Y. (2014). Insights into the catalytic activity and surface modification of MoO3 during the hydrodeoxygenation of lignin-derived model compounds into aromatic hydrocarbons under low hydrogen pressures. *Energy & Environmental Science*, *7*, 2660–2669. https://doi.org/10.1039/c4ee00890a

Pudar, S., Oxgaard, J., Chenoweth, K., Duin, A. C. T. Van, & Goddard, W. A. (2007). Mechanism of Selective Oxidation of Propene to Acrolein on Bismuth Molybdates from Quantum Mechanical Calculations. *Journal of Physical Chemistry*, *111*(44), 16405–16415. https://doi.org/10.1021/jp074452a

Pudar, S., Oxgaard, J., & Goddard III, W. A. (2010). Mechanism of Selective Ammoxidation of Propene to Acrylonitrile on Bismuth Molybdates from Quantum Mechanical Calculations. *Journal of Physical Chemistry*, *114*, 15678–15694. https://doi.org/10.1021/jp103054x

Puy, N., Martı, J. D., Navarro, V., & Mastral, A. M. (2013). Waste tyre pyrolysis – A review. *Renewable and Sustainable Energy Reviews*, *23*, 179–213. https://doi.org/10.1016/j.rser.2013.02.038

Raheem, A., Azlina, W. A. K. G. W., Tau, Y. H., & Danquah, M. K. (2015). Thermochemical conversion of microalgal biomass for biofuel production. *Renewable and Sustainable Energy Reviews*, *49*, 990–999. https://doi.org/10.1016/j.rser.2015.04.186

Ranga, C., Lødeng, R., Alexiadis, V. I., Rajkhowa, T., Bjørkan, H., Chytil, S., Svenum, I. H., Walmsley, J., Detavernier, C., Poelman, H., Voort, P. Van Der, & Thybaut, J. W. (2018). Effect of composition and preparation of supported MoO3 catalysts for anisole hydrodeoxygenation. *Chemical Engineering Journal*, *335*(April 2017), 120–132. https://doi.org/10.1016/j.cej.2017.10.090

Rellán-Piñeiro, M., & López, N. (2018). A Coupled Density Functional Theory-Microkinetic Modeling for the Hydrodeoxygenation of Glycerol to Propylene on MoO3. *ACS Sustainable Chemistry and Engineering*, *6*(12), 16169–16178. https://doi.org/10.1021/acssuschemeng.8b02933

Rensel, D. J., Rouvimov, S., Gin, M. E., & Hicks, J. C. (2013). Highly selective bimetallic

FeMoP catalyst for C – O bond cleavage of aryl ethers. *Journal of Catalysis*, *305*, 256–263. https://doi.org/10.1016/j.jcat.2013.05.026

Rogatis, L. De, Montini, T., Cognigni, A., Olivi, L., & Fornasiero, P. (2009). Methane partial oxidation on NiCu-based catalysts. *Catalysis Today*, *145*, 176–185. https://doi.org/10.1016/j.cattod.2008.04.019

Rowell, R. M., Pettersen, R., Han, J. S., Rowell, J. S., Tshabalala, M. A., & Service, F. (2005). Cell Wall Chemistry. In *Handbook of Wood Chemistry and Wood Composites* (pp. 36–37). CRC Press.

Ruddy, D. A., Schaidle, J. A., Ferrell III, J. R., Wang, J., & Luc Moensb Hensley, J. E. (2014). Recent advances in heterogeneous catalysts for bio-oil upgrading via "ex situ catalytic fast pyrolysis":catalyst development through the study of model compounds. *Green Chemistry*, *16*, 454–490. https://doi.org/10.1039/c3gc41354c

Runnebaum, R. C., Nimmanwudipong, T., Block, D., & Gates, B. C. (2012). Catalytic conversion of compounds representative of lignin-derived bio-oils: a reaction network for guaiacol, anisole, 4-methylanisole, and cyclohexanone conversion catalysed by Pt/Al2O3. *Catalysis Science & Technology*, *2*, 113–118. https://doi.org/10.1039/C1CY00169H

Saidi, M., Samimi, F., Karimipourfard, D., Nimmanwudipong, T., Gates, B. C., & Rahimpour, M. R. (2014). Upgrading of lignin-derived bio-oils by catalytic hydrodeoxygenation. *Energy and Environmental Science*, *7*(1), 103–129. https://doi.org/10.1039/c3ee43081b

Shetty, M., Murugappan, K., Green, W. H., & Roma, Y. (2017). Structural Properties and Reactivity Trends of Molybdenum Oxide Catalysts Supported on Zirconia for the Hydrodeoxygenation of Anisole. *ACS Sustainable Chemistry and Engineering*, *5*, 5293−5301. https://doi.org/10.1021/acssuschemeng.7b00642

Shetty, M., Murugappan, K., Prasomsri, T., Green, W. H., & Román-Leshkov, Y. (2015). Reactivity and stability investigation of supported molybdenum oxide catalysts for the hydrodeoxygenation (HDO) of m-cresol. *Journal of Catalysis*, *331*, 86–97. https://doi.org/10.1016/j.jcat.2015.07.034

Sullivan, M. M., & Bhan, A. (2016). Acetone Hydrodeoxygenation over Bifunctional Metallic − Acidic Molybdenum Carbide Catalysts. *ACS Catalysis*, *6*, 1145−1152. https://doi.org/10.1021/acscatal.5b02656

Tan, Q., Wang, G., Long, A., Dinse, A., Buda, C., Shabaker, J., & Resasco, D. E. (2017). Mechanistic analysis of the role of metal oxophilicity in the hydrodeoxygenation of anisole. *Journal of Catalysis*, *347*, 102–115. https://doi.org/10.1016/j.jcat.2017.01.008

Tsilomelekis, G., & Boghosian, S. (2010). Structural and vibrational properties of molybdena catalysts supported on alumina and zirconia studied by in situ Raman and FTIR spectroscopies combined with 18O/16O isotopic substitution. *Catalysis Today*, *158*(1–2), 146–155. https://doi.org/10.1016/j.cattod.2010.06.026

Valencia, D., Díaz, L., Ramírez-Verduzco, L. F., Amezcua-Allieri, M. A., & Aburto, J. (2019). MoO3 -based catalysts supported on SiO2 and their performance in hydrodeoxygenation. *Materials Letters*, *251*, 226–229. https://doi.org/10.1016/j.matlet.2019.05.075

Venderbosch, R. H., Ardiyanti, A. R., Wildschut, J., Oasmaac, A., & Heeres, H. J. (2010). Stabilization of biomass-derived pyrolysis oils. *Journal of Chemical Technology & Biotechnology*, *85*, 674–686. https://doi.org/10.1002/jctb.2354

Viljava, T., & Krause, A. O. I. (2005). Hydrodeoxygenation of aliphatic esters on sulphided NiMo / g -Al 2 O 3 and CoMo / g -Al 2 O 3 catalyst : The effect of water. *Catalysis Today*, *106*, 186–189. https://doi.org/10.1016/j.cattod.2005.07.129

Wang, S., Gu, Y., Liu, Q., Yao, Y., Guo, Z., Luo, Z., & Cen, K. (2009). Separation of bio-oil by molecular distillation. *Fuel Processing Technology*, *90*, 738–745. https://doi.org/10.1016/j.fuproc.2009.02.005

Weigold, H. (1982). Behaviour of Co-Mo-Al2O3 catalysts in the hydrodeoxygenation of phenols. *Fuel*, *61*(10), 1021–1026. https://doi.org/10.1016/0016-2361(82)90104-1

Whiffen, V. M. L., & Smith, K. J. (2010). Hydrodeoxygenation of 4-Methylphenol over Unsupported MoP, MoS2, and MoOx Catalysts. *Energy & Fuels*, *24*(6), 4728–4737. https://doi.org/10.1021/ef901270h

Wildschut, J., Melián-Cabrera, I., & Heeres, H. J. (2010). Applied Catalysis B : Environmental Catalyst studies on the hydrotreatment of fast pyrolysis oil. *"Applied Catalysis B, Environmental," 99*(1–2), 298–306. https://doi.org/10.1016/j.apcatb.2010.06.036

Xiu, S., & Shahbazi, A. (2012). Bio-oil production and upgrading research : A review. *Renewable and Sustainable Energy Reviews*, *16*(7), 4406–4414. https://doi.org/10.1016/j.rser.2012.04.028

Yakovlev, V. A., Khromova, S. A., Sherstyuk, O. V, Dundich, V. O., Ermakov, D. Y., Novopashina, V. M., Lebedev, M. Y., Bulavchenko, O., & Parmon, V. N. (2009). Development of new catalytic systems for upgraded bio-fuels production from bio-crude-oil and biodiesel. *Catalysis Today*, *144*, 362–366. https://doi.org/10.1016/j.cattod.2009.03.002

Yohe, S. L., Choudhari, H. J., Mehta, D. D., Dietrich, P. J., Detwiler, M. D., Akatay, C. M., Stach, E. A., Miller, J. T., Delgass, W. N., Agrawal, R., & Ribeiro, F. H. (2016). High-pressure vapor-phase hydrodeoxygenation of lignin-derived oxygenates to hydrocarbons by a PtMo bimetallic catalyst : Product selectivity , reaction pathway , and structural characterization. *Journal of Catalysis*, *344*, 535–552. https://doi.org/10.1016/j.jcat.2016.10.009

Zanuttini, M. S., Lago, C. D., Querini, C. A., & Peralta, M. A. (2013). Deoxygenation of m-cresol on Pt /γ-Al2O3 catalysts. *Catalysis Today*, *213*, 9–17. https://doi.org/10.1016/j.cattod.2013.04.011

Zhang, J., Sun, J., & Wang, Y. (2020). Recent advances in the selective catalytic hydrodeoxygenation of lignin-derived oxygenates to arenes. *Green Chemistry*, *22*(4), 1072–1098. https://doi.org/10.1039/c9gc02762a

Zhang, L., Charles, C., & Champagne, P. (2010). Overview of recent advances in thermo-chemical conversion of biomass. *Energy Conversion and Management*, *51*, 969–982. https://doi.org/10.1016/j.enconman.2009.11.038

Zhang, X., Tang, J., Zhang, Q., Liu, Q., Li, Y., & Chen, L. (2019). Hydrodeoxygenation of lignin-derived phenolic compounds into aromatic hydrocarbons under low hydrogen pressure using molybdenum oxide as catalyst. *Catalysis Today*, *319*(March 2018), 41–47. https://doi.org/10.1016/j.cattod.2018.03.068

Zhang, X., Wang, T., Ma, L., Zhang, Q., & Jiang, T. (2013). Bioresource Technology Hydrotreatment of bio-oil over Ni-based catalyst. *Bioresource Technology*, *127*, 306–311. https://doi.org/10.1016/j.biortech.2012.07.119

Zhao, C., Kou, Y., Lemonidou, A. A., Li, X., & Lercher, J. A. (2009). Highly Selective Catalytic Conversion of Phenolic Bio-Oil to. *Biofuels, Bioproducts and Biorefining*, *48*, 3987–3990. https://doi.org/10.1002/anie.200900404

Zhao, H. Y., Li, D., Bui, P., & Oyama, S. T. (2011). Hydrodeoxygenation of guaiacol as model compound for pyrolysis oil on transition metal phosphide hydroprocessing

catalysts. *Applied Catalysis A : General*, *391*, 305–310.
https://doi.org/10.1016/j.apcata.2010.07.039

Zhu, X., Lobban, L. L., Mallinson, R. G., & Resasco, D. E. (2011). Bifunctional
transalkylation and hydrodeoxygenation of anisole over a Pt / HBeta catalyst. *Journal of Catalysis*, *281*(1), 21–29. https://doi.org/10.1016/j.jcat.2011.03.030

Chapter 3

3   Methods and Results

3.1   Catalyst Materials and Synthesis

Bulk MoO_3 (≥99.5%) was purchased from Sigma-Aldrich. TiO_2 (≥99.5%, 21 nm diameter), SiO_2 (Davisil®, Grade 633, pore size 60Å), ZrO_2 (99.95 %, 20 nm) and CeO_2 (99.97 %, 10-30 nm) were purchased from Sigma-Aldrich and used directly as supports. Spherical γ-alumina particles (1.7 mm diameter, K2476) were purchased by Sasol. The alumina spheres were ground and sieved to obtain 200 – 425 μm particle sizes for use as a support.

10 wt. % MoO_3/SiO_2 and 10 wt. % MoO_3/ZrO_2 were prepared via incipient wetness impregnation. 1 g of supported catalyst was synthesized by first dissolving 0.136 g of ammonium molybdate tetrahydrate $((NH_4)_6Mo_7O_{24}\cdot 4H_2O$, 83 %, Sigma-Aldrich) in a volume of deionized water corresponding to the pore volume of the support. Then the solution was added dropwise to the support and was vigorously mixed. Next, the sample was placed in an oven for 12 h at 100 °C. Using a quartz reactor with an inner diameter of 2.2 cm, the samples were then calcined at 500 °C (ramp of 10 °C/min) in an air flow rate of 60 mL/min for 3 h.

TiO_2, CeO_2 and γ-Al_2O_3 supported 10 wt. % MoO_3 catalysts were prepared using the wetness impregnation method. 1 g of supported catalyst was synthesized by first dissolving 0.136 g of ammonium molybdate tetrahydrate $(NH_4)_6Mo_7O_{24}\cdot 4H_2O)$ in approximately 10 mL of deionized water. Then the support was added to the solution and was vigorously mixed for 24 h. The sample then underwent vacuum filtration to remove most of the solvent and then was dried in an oven for 12 h at 100 °C. Finally, the catalyst was calcined at the same conditions outlined above.

3.2   Catalyst Characterization

The bulk and supported MoO_3 catalysts were characterized via H_2-TPR, ex situ UV-Vis and in situ UV-Vis.

3.2.1   Temperature Programmed Reduction (H$_2$ – TPR)

A catalyst or support mass of 100 mg was loaded in a 0.25 in. ID quartz tube reactor. The reactor was placed inside a furnace which was connected to a temperature controller (Watlow, series 98) and a K-type thermocouple. The sample was then treated in a gas mixture of H$_2$ in argon (5 vol. % H$_2$, balance He) at a flowrate of 41 mL/min at atmospheric pressure. The temperature was then increased to 1000 °C at a rate of 10 °C/min and the H$_2$ consumption was measured using an SRI 110 TCD detector.

3.2.2   Ex Situ UV-Vis Spectroscopy

Diffuse reflectance UV-Vis spectra of the catalysts and supports were collected using a UV-VIS-NIR spectrometer (Shimadzu, model 3600) with a diffuse reflectance cell (Harrick, Praying Mantis) using BaSO$_4$ (Sigma-Aldrich, 99 %) as a white reference. Samples were packed down and flattened in the sample holder and UV/Vis spectra were obtained in the range of 200 to 800 nm in diffuse reflectance mode with 1 nm step size. UV Probe software was used to transform the reflectance into the corresponding absorbances via the Kubelka-Munk function.

3.2.3   In Situ UV-Vis Spectroscopy

Diffuse reflectance UV-Vis spectra of the spent catalysts were collected using a UV-VIS-NIR spectrometer (Shimadzu, model 3600) with a high temperature reaction chamber accessory (Harrick, model HVC-VUV-5). A schematic of the reactor set up can be seen in Figure 3.1. BaSO$_4$ (Sigma-Aldrich, 99 %) was used as a white reference. The baseline spectrum was obtained by first packing a small amount of BaSO$_4$ into the sample cup of the high temperature reaction chamber. Next, the dome was installed and the windows were wiped clean with a Kimtech wipe. Then the reflectance was measured for the 200 to 800 nm region and it was subsequently transformed into absorbance by via the Kubelka-Munk function. Finally, the dome was removed and the BaSO$_4$ sample was discarded.

After the baseline was obtained, a small amount of catalyst was packed down and flattened into the sample cup of the high temperature reaction chamber. Then, the dome was installed

and the pre-run diffuse reflectance spectra was measured using a UV-VIS-NIR spectrometer (Shimadzu, model 3600) at STP.
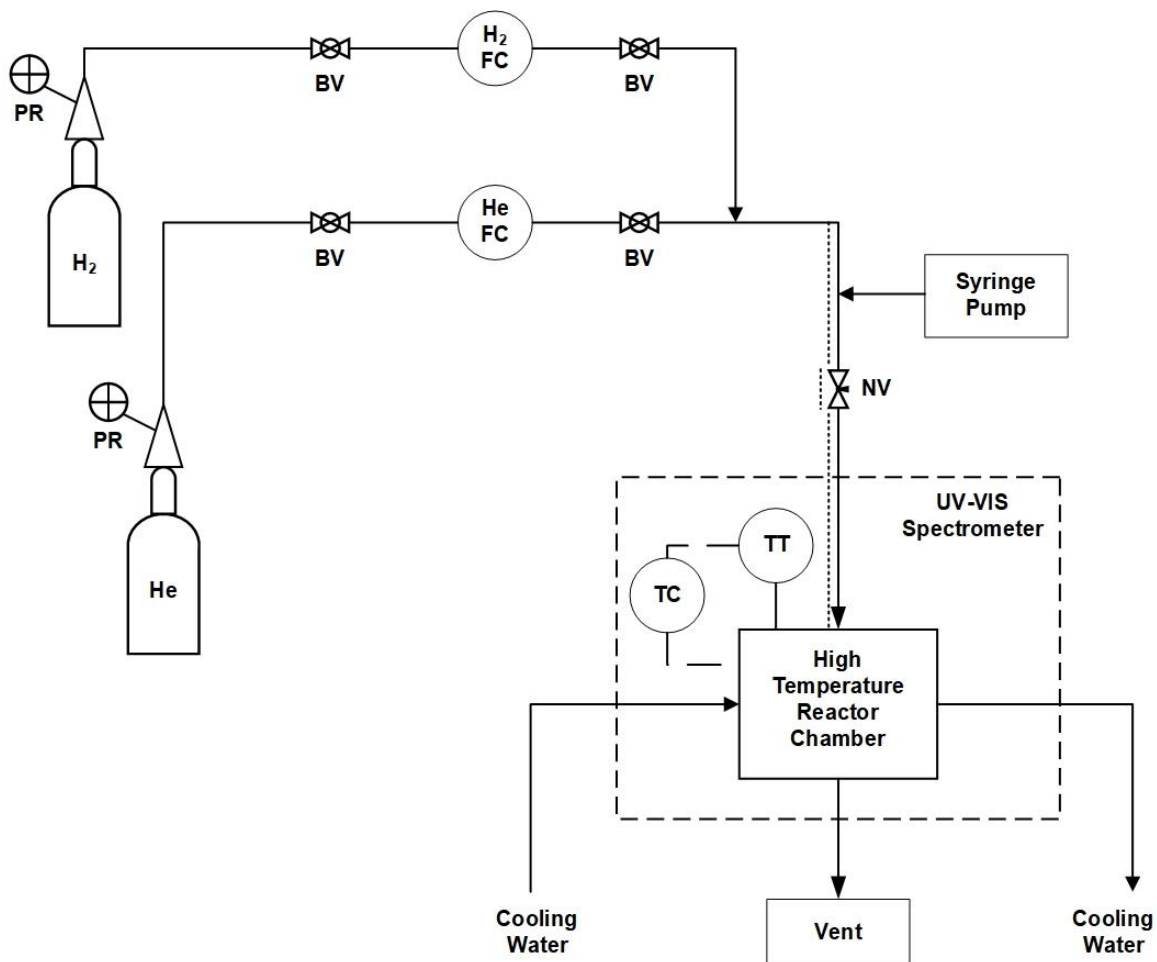
Figure 3.1 Schematic of in situ UV-Vis system (TT = temperature transmitter, TC = temperature controller, NV = needle valve, BV = ball valve, FC = flow controller, PR = pressure regular)

3.3   In situ Reduction Experiment

The baseline and pre-run sample was obtained using the procedure outlined above. Helium gas (Praxair, Ultra-High Purity (UHP)) flowed through the sample cup of the reaction chamber at 15.5 mL/min via a flow controller (VICI Condyne, model FC30SS1S3) and cooling water flowed through the shell of the reaction chamber in order to keep the outside walls cool while the sample cup was at a high temperature. Next, the temperature of the sample cup was increased to 150 °C at a rate of 20 °C/min via a K-type thermocouple and temperature controller (Harrick model ATK- 024-3) and was held for 30 minutes. Then hydrogen gas

(Praxair, Ultra-High Purity (UHP)) flowed through the sample cup of the reaction chamber at 15.5 mL/min via a flow controller (VICI Condyne, model FC30SS1S3) and was held for 1 h. Then the reactor chamber was cooled down to room temperature in helium gas at 15.5 mL/min and the diffuse reflectance spectra was measured using a UV-VIS-NIR spectrometer (Shimadzu, model 3600). The procedure was then repeated for the temperatures of 200, 250, 300 and 350 °C using the same catalyst sample.

3.4   In situ Reaction Experiment

The baseline and pre-run sample was obtained using the procedure outlined above. The temperature of the stainless-steel piping was increased to 150 °C via a heater (Staco Energy Products, model 3PNJ201B). Helium gas (Praxair, Ultra-High Purity (UHP)) flowed through the sample cup of the reaction chamber at 15.5 mL/min via a flow controller (VICI Condyne, model FC30SS1S3) and cooling water flowed through the shell of the reaction chamber. Next, the temperature was increased to 150 °C at a rate of 20 °C/min via a K-type thermocouple and temperature controller (Harrick model ATK- 024-3) and was held for 30 minutes. Then hydrogen gas (Praxair, Ultra-High Purity (UHP)) flowed through the sample cup of the reaction chamber at 15.5 mL/min via a flow controller (VICI Condyne, model FC30SS1S3) and anisole was injected using a 0.5 mL Hamilton syringe at 0.09 mL/h via a syringe pump (KD Scientific, model 100) and was held for 40 minutes. Then the flow was switched to helium and was held at 150 °C for 30 minutes to remove any adsorbed species. Then the reactor chamber was cooled down to room temperature in helium gas at 15.5 mL/min and the diffuse reflectance spectra was measured using a UV-VIS-NIR spectrometer (Shimadzu, model 3600). The procedure was then repeated for reaction temperatures of 200, 250, 300 and 350 °C using the same catalyst sample.

3.5   Band gap energy calculations

The diffuse reflectance UV-Vis spectrum recorded for each sample was evaluated via the software UV Probe and transformed into the corresponding absorbances via the Kubelka-Munk function. R_∞ was evaluated by taking the negative difference between the sample absorbance and the baseline absorbance and raising 10 to the resultant power as shown in equation (3).

$$R_\infty == 10^{[-(\text{Abs}_{\text{sample}} - Abs_{baseline})]} \qquad (3)$$

The Kubelka-Munk function was evaluated from R_∞ as shown in equation (4).

$$F(R_\infty) = \frac{(1 - R_\infty)^2}{2R_\infty} \qquad (4)$$

Equation (5) was plotted as a function of $h\nu$ which is in the incident photon energy in electron volts (eV) where h represents Planck's constant (4.136×10^{-15} eV·s),

$$y = [F(R_\infty) * h\nu]^2 \qquad (5)$$

and ν is the frequency calculated using c, the speed of light (3.00×10^8 m/s) and the wavelength (λ) as shown in equation (6).

$$\nu = \frac{c}{\lambda} \qquad (6)$$

This is known as a Tauc plot. It should be noted that the exponent in equation (5) depends on the type of transitions occurring. In this case, the exponent is equal to 2 for direct allowed transitions. The linear region of a Tauc plot indicates the onset of absorption. Therefore, the absorption edge energy or band gap energy (Eg) was determined by extrapolating the linear region to the x-axis using the tangent.opx file in Origin.
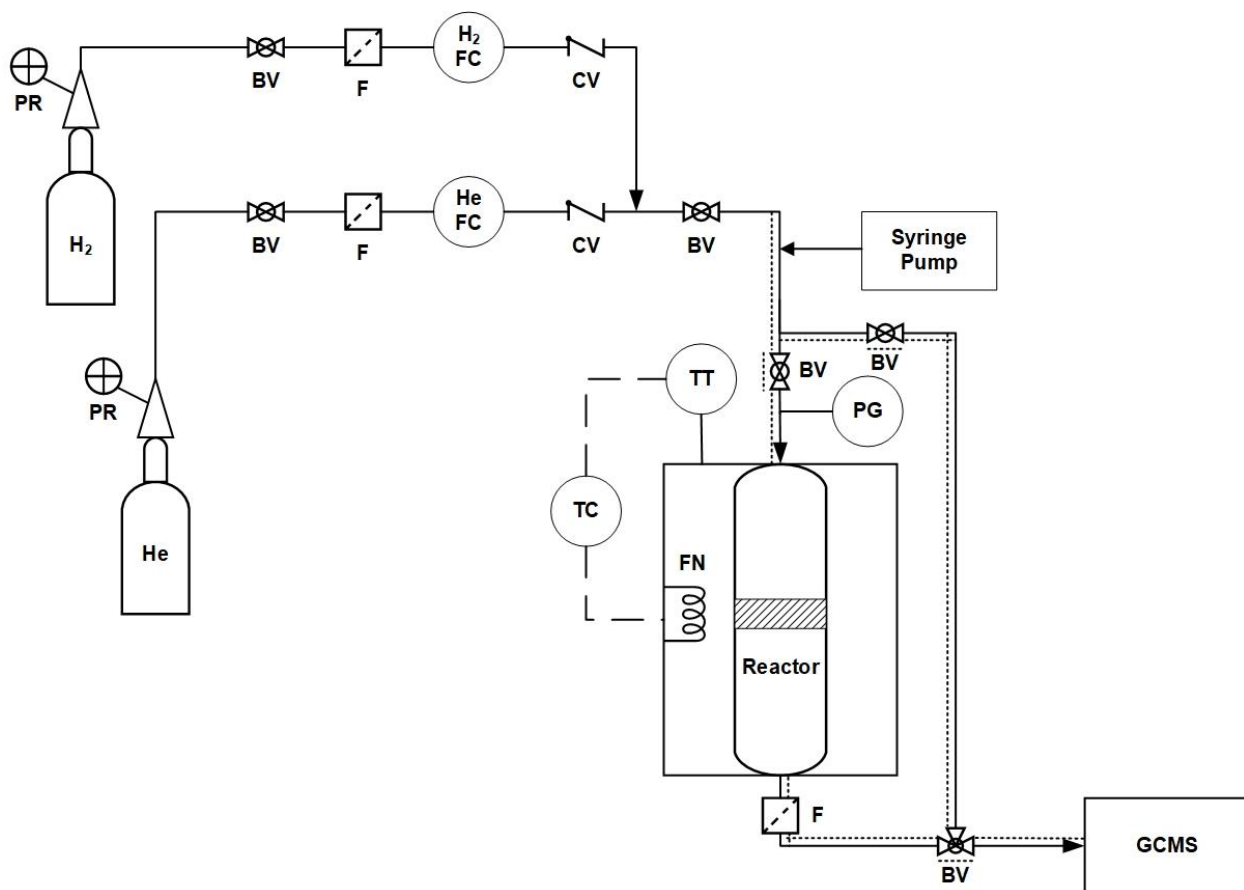
3.5.1   Catalyst Activity Measurement

Figure 3.2 Schematic of gas phase catalyst activity system (TT = temperature transmitter, TC = temperature controller, PG = pressure gauge, BV = ball valve, CV = check valve, F = filter, FC = flow controller, PR = pressure regular)

Catalytic activity tests were carried out in a 0.25 in. ID quartz tube fixed bed reactor which was mounted to a furnace (Figure 3.2). Catalysts (0.1 g) were pelletized between 600 and 850 μm mesh and placed in the middle of the reactor. Under helium (Praxair, UHP), the reactor temperature was increased to the reaction temperature at a rate of 10 °C/min via a K-type thermocouple and temperature controller (Watlow, series 98). Then the helium gas was turned off and hydrogen gas (Praxair, UHP) was introduced into the system at a flowrate of 11.5 mL/min via a mass flow controller (MKS, model 100). Next, anisole was injected using a 250 μm Hamilton syringe at 63 μm/h via a syringe pump (KD Scientific, model 100) into the stainless-steel tubing located upstream of the reactor. The liquid reactant was immediately vaporized as the tubing was heated to 200 °C via electric heat tracing. Prior to the reaction, the anisole and hydrogen gas mixture flowed through the by-pass system for 30 minutes in order

to reach steady state. The piping of the by-pass system and the piping located downstream of the reactor was heated to 250 °C via electric heat tracing to ensure condensation of the products and/or reactant did not occur. Then the ball valve for the by-pass system was closed, the ball valve for the inlet of the reactor was opened and the 3-way ball valve was turned to allow the gas stream to flow from the reactor. A GCMS (Agilent 7890A/5975C) with a HP-5MS column (Agilent, 30 m x 0.250 mm x 0.25 μm film thickness) was used to analyze the products of the reaction. The injector temperature was 300 °C and a split ratio of 1:30 was used. The initial oven temperature was 50 °C and was held for 2 minutes followed by a ramp of 10 °C /min until a final oven temperature of 230 °C which was held for 2 minutes. The weight hourly space velocity (WHSV), conversion and product selectivity were calculated by equations (7), (8) and (9), respectively.

$$WHSV = \frac{mass\ flow\ rate\ of\ anisole\ fed}{mass\ of\ equivalent\ catalyst\ loaded} \qquad (7)$$

$$Conversion\ (\%) = \frac{moles\ of\ anisole\ consumed}{moles\ of\ anisole\ fed} x\ 100 \qquad (8)$$

$$Product\ Selectivity\ (\%) = \frac{moles\ of\ product}{moles\ of\ anisole\ consumed} x\ 100 \qquad (9)$$

3.6 H_2-TPR Results

The reducibility of the molybdebum-based supported catalysts was investigated by H_2-TPR (Figure 3.3). Control experiments of all the blank supports except for CeO_2, resulted in no positive hydrogen consumption peaks, indicating that the supports are not reducible (Figure 3.4) under the conditions used for TPR. However, both SiO_2 and Al_2O_3 TPR results show negative hydrogen consumption peaks, which could be due to the presence of water on the support's surface. As the supports are heated, water on the support's surface evaporates into steam. Since the thermal conductivity of gas phase water is greater than that of argon, the thermal conductivity of the effluent gas mixture would increase, thus causing a negative peak.
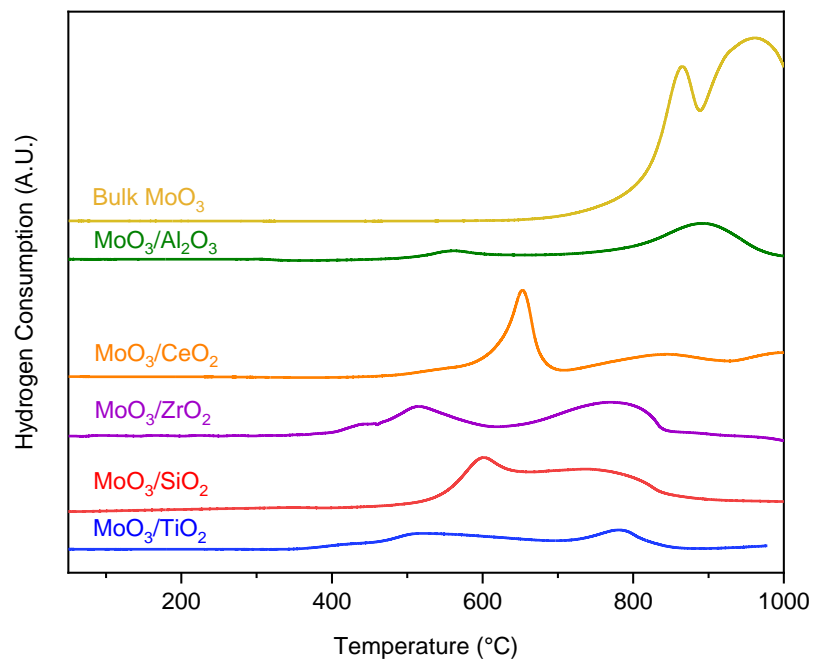
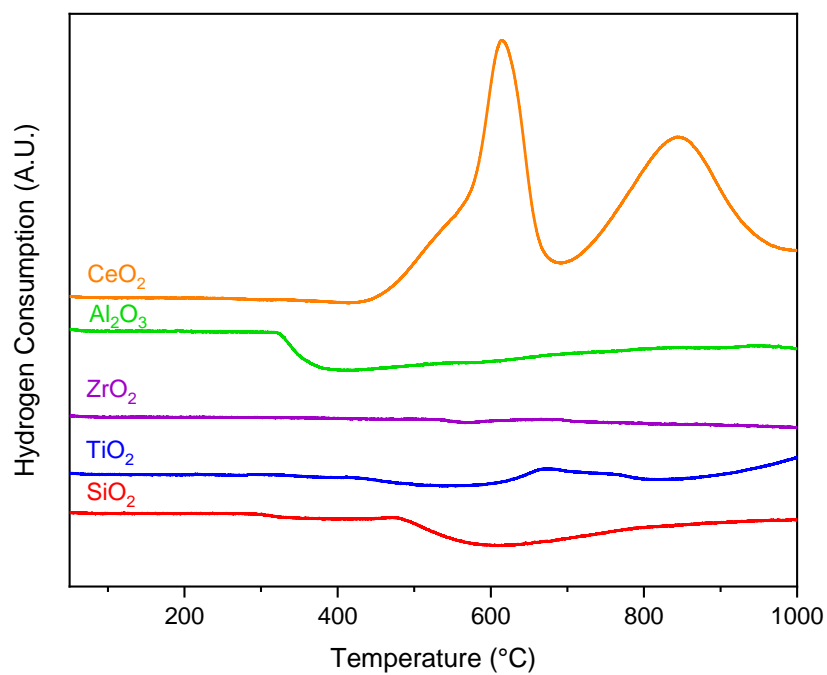**Figure 3.3 H₂-TPR of bulk and supported MoO₃ catalysts**

Figure 3.4 H₂-TPR of bare supports, CeO₂, γ-Al₂O₃, ZrO₂, TiO₂ and SiO₂

Blank ceria, on the other hand, was shown to have positive hydrogen consumption peaks which is consistent with literature (Wan et al., 2008). H_2-TPR of low surface area CeO_2 has been reported to result in one high temperature peak corresponding to its bulk reduction ($CeO_2 \rightarrow$ Ce). On the other hand, high surface area CeO_2 has reportedly resulted in two peaks, where the lower temperature peak is assigned to the reduction of surface Ce^{4+} and impurities such as CO and CO_2, and the high temperature peak is attributed to the reduction of the bulk CeO_2 (Giordano et al., 2000; Heracleous et al., 2005; Wan et al., 2008). Impregnation of MoO_3 onto the CeO_2 support caused the peak corresponding to the lowest temperature to increase in intensity and to shift to a higher temperature (Figure 3.5). The corresponding peak area increased by more than 50 % when MoO_3 was added to the support. Therefore, we can assume that the increase in peak area is due to the reduction of an Mo species and not due to the reduction of CeO_2. Also, a new peak is formed at 997 °C when MoO_3 is added to the support, indicating an Mo species is reduced.

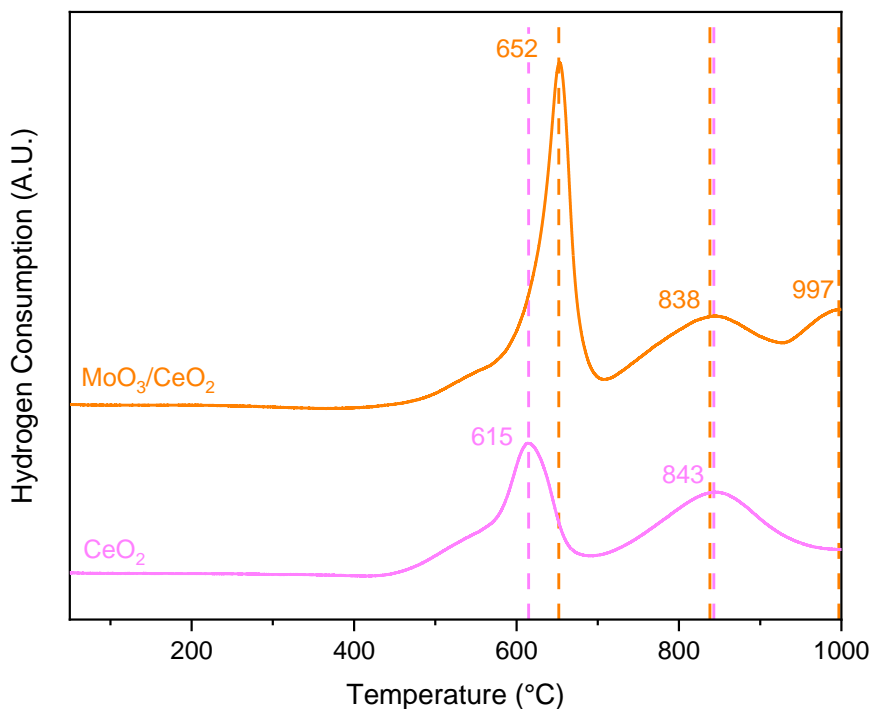**Figure 3.5 H_2-TPR of bare CeO_2 and MoO_3/CeO_2**

The reducibility of bulk MoO_3 was also studied by H_2-TPR, where two peaks were formed at the maximum temperature of reduction (T_{max}) values of 865 and 961 °C, respectively (Figure

3.3). It is well known that the reduction of MoO_3 occurs via two main steps: MoO_3 (Mo^{+6}) → MoO_2 (Mo^{+4}) and MoO_2 (Mo^{+4}) → Mo (Mo^0) (Arnoldy et al., 1985; Chary et al., 2004). The first step of the reduction has been shown to occur in more than one temperature range and therefore can result in more than one peak (Arnoldy et al., 1985; Zhang, Liu, et al., 2019; Shetty et al., 2015). However, the second step of the reduction only takes place in one band, thus forming only one peak. Lastly, a minor peak corresponding to the reduction of MoO_3 → Mo_4O_{11} can also form after the MoO_3 → MoO_2 peak(s) (Ressler et al., 2000; Zhang, Liu, et al., 2019; Shetty et al., 2015). This minor peak was not seen in our results, likely due to a lack of sensitivity of the equipment. The peak at 865 °C is assigned to the reduction of MoO_3 to MoO_2 and the 961 °C peak is attributed to the reduction of MoO_2 to Mo.

Compared to bulk MoO_3, the supported MoO_3 catalysts had significantly lower T_{max} values. This is consistent with the literature as the addition of a support increases the reducibility of the MoO_3 catalyst (i.e., lower temperatures are required to create the Mo^{5+} active sites) (Shetty et al., 2015; Chary et al., 2004). Impregnating MoO_3 onto a support increases the dispersion of MoO_3, thus increasing the MoO_3 surface area. The larger the surface area of MoO_3, the greater the probability of hydrogen reducing the MoO_3 surface.

H_2-TPR studies have determined that the reducibility of a supported catalyst is inversely related to the metal-support interaction (Wan et al., 2008; Arena & Parmaliana, 1996; Chary et al., 2004; Alvarez-amparán et al., 2020). The stronger the interaction between the metal and the support, the higher the temperature is needed for the reduction to occur and vice versa. H_2-TPR of the MoO_3/TiO_2, MoO_3/γ-Al_2O_3 and MoO_3/SiO_2 catalysts resulted in two hydrogen consumption peaks, whereas three peaks were observed for the MoO_3/ZrO_2 and MoO_3/CeO_2 catalysts. However, based on Figure 3.5, the peak at approximately 840 °C is assigned to the reduction of CeO_2 and not due to the reduction of an Mo species. Therefore, two peaks are produced due to the reduction of an Mo species for the MoO_3/TiO_2, MoO_3/γ-Al_2O_3, MoO_3/SiO_2 and MoO_3/CeO_2 catalysts.

The two hydrogen consumption peaks of these catalysts can be classified based on their T_{max} values: a low temperature peak with a T_{max} value between 400 – 700 °C and a high temperature peak with a T_{max} value between 700 – 1000 °C. The low temperature peak is attributed to the reduction of octahedrally coordinated molybdenum species $(Mo_{oct}^{+6}$ → $Mo_{oct}^{+4})$ and the high

temperature peak is attributed to the reduction of tetrahedrally coordinated molybdenum species ($Mo_{tet}^{+6} \rightarrow Mo_{tet}^{+4}$) (Ranga et al., 2018; Maity et al., 2001; Lødeng et al., 2017). There is a stronger interaction between a support and a molybdenum species when molybdenum is tetrahedrally coordinated than when it's octahedrally coordinated. The stronger the interaction between the support and the Mo metal, the higher the temperature is needed to reduce the catalyst. H_2-TPR studies of MoO_3/Al_2O_3 have concluded that the second peak can also be attributed to the second step of the reduction of the octahedral molybdenum species ($Mo_{oct}^{+4} \rightarrow Mo_{oct}^{0}$) (Cedeno-Caero & Alvarez-Amparan, 2014; Cordero & Agudo, 2000). We can therefore assume that the high temperature peak of the other supported catalysts could also be attributed to the second step reduction of the octahedral molybdenum species. For catalysts with high Mo loadings, the high temperature peak can also be due to the reduction of polymerized octahedral Mo species (Zhu et al., 2005; Hahn et al., 2014; Maity et al., 2001). Our supported MoO_3 catalysts have loadings of 10 wt. % which corresponds to below monolayer coverages, thus ensuring that crystallization does not occur. It has however been frequently reported that 5 wt. % is the maximum loading of MoO_3 on SiO_2 before crystalline nanoparticles are formed, despite this loading only corresponding to a fraction of monolayer coverage of 0.20 (Boer et al., 1991; Tian et al., 2010; Tsilomelekis & Boghosian, 2013). This is due to the weak interaction between heptamolybdate and SiO_2. Since our SiO_2 supported catalyst has a MoO_3 loading that's greater than 5 wt. %, its broad high temperature peak in Figure 3.5 is likely due to an overlapping of peaks resulting from the reduction of tetrahedrally and octahedrally molybdenum species and crystalline MoO_3.

Unlike the other supported catalysts, H_2-TPR of the MoO_3/ZrO_2 catalyst resulted in three peaks which have T_{max} values of 444, 516 and 771 °C, respectively. The peak at 516 °C is attributed to the reduction of octahedral Mo species ($Mo_{oct}^{+6} \rightarrow Mo_{oct}^{+4}$) and the peak at 771 °C is likely due to the simultaneous reduction of tetrahedrally coordinated molybdenum species ($Mo_{tet}^{+6} \rightarrow Mo_{tet}^{+4}$) and a further reduction of the octahedral Mo species ($Mo_{oct}^{+4} \rightarrow Mo_{oct}^{0}$). The additional low temperature peak at 444 °C that was not observed for the other supported catalysts, could be due to the reduction of the mixed oxide phase $Zr(MoO_4)_2$ (Ranga et al., 2018; Shetty et al., 2015).

In agreement with previous studies, the reducibility of the catalysts decreased in the following order: MoO_3/ZrO_2 (444 °C) > MoO_3/TiO_2 (523 °C) > MoO_3/γ-Al_2O_3 (561 °C) > MoO_3/SiO_2 (601 °C) > MoO_3/CeO_2 (652 °C) (Yun & Guliants, 2019; Kaluža et al., 2007; Shetty et al., 2015). The more reducible a supported MoO_3 catalyst is, the greater the number of Mo^{5+} sites that can be created. MoO_3/ZrO_2 was the most reducible catalyst meaning that the interaction between the molybdenum metal and the support was the weakest, thus allowing for the Mo^{5+} sites to be created at a lower temperature compared to the other supported catalysts.

It's well established that hydrogen consumption is directly related to the formation of oxygen vacancies which serve as the active site for HDO. However, it's also possible to over-reduce MoO_3 (Mo^{6+}) to an oxidation state of Mo^{4+}, rendering it inactive for HDO. Figure 3.3 indicates that most of the hydrogen was consumed above 350 °C for all the supported catalysts. Since activity experiments were conducted at a maximum temperature of 350 °C, the molybdenum oxide species were not immediately over-reduced.

3.7   Catalyst Activity and Observed Product Selectivity

Anisole conversion and product selectivities obtained using the supported MoO_3 catalysts were evaluated at steady state conditions at different temperatures following the methodology outlined in section 3.2.4. A typical kinetic experiment is shown in Figure 3.6.
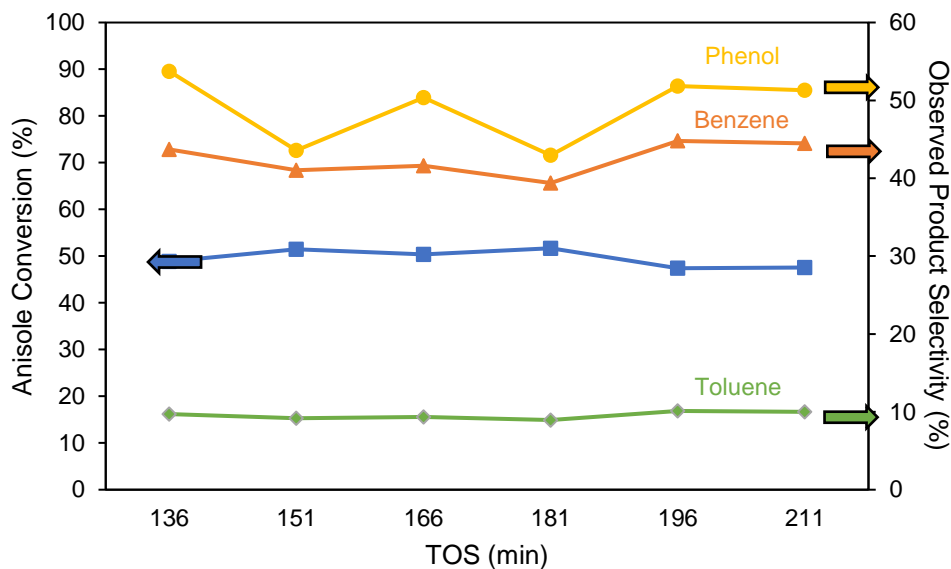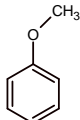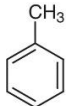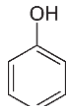
Figure 3.6 Anisole conversion and observed product selectivity vs time on stream (TOS) for HDO over MoO₃/TiO₂. Reaction conditions: T = 350 °C, P_{Total} = 1.013 bar (0.0191 bar P_{Feed}, balance H₂), WHSV = 0.63 h⁻¹

Table 3.1 shows the values for conversion and selectivity obtained over the supported catalysts. HDO over MoO_3/SiO_2 resulted in low anisole conversions, averaging 5.5 % when the TOS was 35 to 215 min. This is consistent with the H_2-TPR results, which demonstrated the low reducibility of the silica supported catalyst. Shetty et al. also observed low activity for the gas phase HDO of m-cresol over 10 wt. % MoO_3/SiO_2 with a 10 % conversion, postulating that it was due to its low reducibility and high electronegativity of the silica support cation (Si^{4+}) (Shetty et al., 2015). In similar redox processes, such as methanol oxidation or oxidative dehydrogenation of ethane and propane, an inverse correlation between catalytic activity and electronegativity of the support cation for MoO_3 supported catalysts has been observed (Tsilomelekis et al., 2007; Heracleous et al., 2005). It's known that for these redox reactions decreasing the electronegativity of the support cation ($Si^{4+} > Al^{3+} > Ti^{4+} > Zr^{4+} > Ce^{4+}$) increases the electron density of the Mo – O – support bridging oxygen atom, which allows for easier hydride abstraction. Results obtained by Shetty et al. indicate an inverse relationship between HDO catalytic activity and electronegativity of the support cation, except for MoO_3/CeO_2 because of the previously described phenomena, since oxygen vacancies get replenished with atoms from the bulk CeO_2 support (Shetty et al., 2015). It is thus hypothesized that the Mo – O – support bridging oxygen atoms also play a crucial role in the hydride abstraction step involved in creating oxygen vacancies which are required for HDO to occur

(Shetty et al., 2015). The low conversion of anisole over MoO_3/CeO_2 (4.3 %) was also seen in Shetty et al.'s gas phase HDO experiment where 10 wt.% MoO_3/CeO_2 resulted in 8 % m-cresol conversion (Shetty et al., 2015).

Table 3.1 Activity data for the conversion of anisole over supported 10 wt. % MoO_3 catalysts, P_{Total} = 1.013 bar (0.0191 bar P_{Feed}, balance H_2), WHSV = 0.63 h^{-1} and TOS = 0 – 215 min.

Catalyst	Temperature (°C)	Anisole Conversion (%)	Product Selectivity (%)		
			Benzene	Toluene	Phenol
MoO₃/ZrO₂	350	46 ± 0.8	61 ± 1.8	17 ± 0.6	29 ± 6.6
	325	16 ± 1.3	42 ± 3.6	18 ± 1.6	39 ± 5.7
	300	3.9 ± 2.3	n/d	n/d	n/d
MoO₃/TiO₂	350	50 ± 1.9	42 ± 2.2	10 ± 0.5	49 ± 4.6
	325	33 ± 1.7	32 ± 1.8	8.8 ± 0.3	33 ± 5.3
	250	5.5 ± 1.3	n/d	n/d	n/d
MoO₃/Al₂O₃	350*	98 ± 1.4	6.1 ± 0.1	2.7 ± 0.1	49 ± 9.1
MoO₃/SiO₂	350	5.5 ± 2.0	n/d	n/d	n/d
MoO₃/CeO₂	350	4.3 ± 1.1	n/d	n/d	n/d

n/d: Not determined due to very low conversions.
* Data obtained before catalyst deactivation.

Surprisingly, the MoO_3/γ-Al_2O_3 catalyst had the highest activity with nearly 100 % anisole conversion for the first 65 min of TOS, even though it is less reducible than MoO_3/TiO_2 and MoO_3/ZrO_2 and the support cation, Al^{3+}, is more electronegative than Ti^{4+} and Zr^{4+}, respectively. After one hour, however, the catalyst experienced severe deactivation, decreasing to 18.5 % conversion after TOS = 3.3 h (Figure 3.9). The low activity of 10 wt. % MoO_3/γ-Al_2O_3 was also observed by Shetty et al. for the HDO of m-cresol after a TOS of 3 h with 13 % conversion (Shetty et al., 2015). Gonçalves et al., however, conducted an experiment for the liquid phase HDO of m-cresol over 10 wt. % MoO_3/γ-Al_2O_3 at a space time of 26 g h / mol

and a TOS of 0 – 5 h and observed a low average conversion of roughly 16 % (Gonçalves et al., 2017). The same experiment was also conducted over 10 wt. % MoO_3/SiO_2 and the average conversion was the same at roughly 16 %. After a TOS of 20 h, the catalysts had the same levels of conversion, unlike atmospheric HDO studies which experience high levels of deactivation. Unlike the other supported catalysts in this study, $MoO_3/\gamma\text{-}Al_2O_3$ did not achieve high levels of deoxygenation, as seen by the low benzene and toluene selectivities and high selectivity towards phenol. It's thus possible that this catalyst undergoes a different mechanism than the other supported catalysts. It also had a high selectivity towards phenol derivatives which can be attributed alumina's acid sites, which are well known to facilitate transalkylation reactions (Nimmanwudipong, Ron C., et al., 2011); Runnebaum et al., 2012). The phenol derivative values, however, were not quantified so their selectivities were not determined. $MoO_3/\gamma\text{-}Al_2O_3$'s higher selectivity towards oxygenated products than deoxygenated products was not observed by Shetty et al. who found that $MoO_3/\gamma\text{-}Al_2O_3$ had higher yields of toluene (10 %) than phenol (1 %) and dimethyl phenol (1 %) at a low average conversion of 13 % (Shetty et al., 2015).

MoO_3/TiO_2 and MoO_3/ZrO_2 are promising HDO catalysts due to their excellent stability and ability to achieve high degrees of deoxygenation. Although at 350 °C MoO_3/TiO_2 and MoO_3/ZrO_2 had lower anisole conversions (50 and 46 %, respectively) than $MoO_3/\gamma\text{-}Al_2O_3$ (98 %), these catalysts had higher selectivities towards benzene and toluene (42 and 10 %, and 61 and 17 %, respectively) and lower levels of phenol selectivity (49 and 29 %, respectively). Either these catalysts selectively cleave anisole's $C_{aromatic} - O$ bond over the weaker $C_{aliphatic} - O$ bond or anisole first gets converted to phenol and subsequently phenol gets deoxygenated to benzene. Since the methanol and methane selectivities were not determined, it's impossible to say which of these two possible reaction pathways occurred. Using MoO_3/TiO_2 and MoO_3/ZrO_2, Shetty et al. obtained relatively high m-cresol conversions of 47 and 78 %, respectively with toluene being the only major product and zero selectivity towards benzene and phenol (Shetty et al., 2015). Another group studied the gas phase HDO of anisole over 12 wt. % MoO_3/ZrO_2 at 340 °C and at a TOS of 10 h and obtained roughly 53 % conversion (Ranga et al., 2018). The corresponding product selectivities were approximately 38 % benzene, 18 % phenol, 10 % cresol, 9 % toluene, 4 % methane and 5 % dimethyl phenol. Another study found that at 320 °C and at atmospheric pressure, 10 wt. % MoO_3/ZrO_2 resulted

in an average 51 % anisole conversion for a TOS of 0 – 4 h and the following product selectivities: 20 % benzene, 9 % toluene, 8 % other aromatics, 23 % phenol, 4 % methyl anisole, 19 % cresol, 13 % dimethyl phenol, 2 % other oxygenates and 2 % methane. (Shetty et al., 2017). Therefore, this study observed a lower selectivity towards deoxygenated products (37 %) compared to the deoxygenated product selectivity we obtained for MoO_3/ZrO_2 at 325 °C (60 %).

The superior stabilities of the titania and zirconia supported catalysts are believed to be due to slower rates of coke formation as TiO_2 and ZrO_2 are less acidic than γ-Al_2O_3 (Shetty et al., 2015). Although thermogravimetric analysis (TGA) of the spent samples was not performed to confirm this hypothesis, other studies have demonstrated a direct correlation between support acidity and coking, where the acidity of the support is reported to decrease in the following order: γ-$Al_2O_3 \gg TiO_2 > ZrO_2$ (He et al., 2012; Kydd et al., 2009). This is consistent with the observed stabilities where MoO_3/γ-Al_2O_3 had a much faster rate of deactivation than MoO_3/TiO_2 and MoO_3/ZrO_2 and the titania supported catalyst had better stability than MoO_3/ZrO_2, with the conversions decreasing from 61 to 48 % for a TOS of 16 to 211 min and from 47 to 42 % for a TOS of 20 to 200 min, respectively. The figure illustrating the difference in catalyst stabilities can be found in Appendix A.

The effect of temperature on the HDO of anisole was evaluated for the MoO_3/ZrO_2 and MoO_3/TiO_2 catalysts (Table 3.2). For both catalysts, increasing the temperature from 325 to 350 °C led to an increase in anisole conversion and benzene selectivity, while toluene selectivity remained constant. Other studies have also found that higher reaction temperatures result in higher conversions and higher selectivities towards aromatic hydrocarbons (Boullosa-eiras et al., 2014; Zhang, Liu, et al., 2019; Prasomsri et al., 2013). (Boullosa-eiras et al., 2014; c; X. Zhang, Liu, et al., 2019; Prasomsri et al., 2013). Therefore, higher temperatures favour the cleavage of anisole's $C_{aromatic}$ – O bond. However, X. Zhang, Liu, et al. found that conversion and selectivity to aromatic hydrocarbons decreased when the reaction temperature was above 360 °C as polycyclic aromatic hydrocarbons were formed, likely blocking the active sites (X. Zhang, Liu, et al., 2019).

3.7.1   Activation Energy

Activation energies (E_a) were determined for the HDO of anisole over MoO_3/ZrO_2 and MoO_3/TiO_2 by creating Arrhenius plots, assuming a pseudo first order dependence on anisole for the overall reaction rate and carrying a mol balance at differential reactor conditions. The differential equation for a fixed bed reactor is shown below:

$$\frac{dX}{dW} = -\frac{r_A}{F_{AO}} \tag{10}$$

where X represents the conversion of anisole, W is the catalyst weight, r_A is the rate of reaction of anisole and F_{AO} is the initial molar flowrate of anisole. The pseudo first order reaction rate for anisole is shown below:

$$r_A = -kC_A \tag{11}$$

The concentration of anisole can be written as follows:

$$C_A = \frac{F_A}{v} \tag{12}$$

where F_A is the molar flowrate of anisole and v is the volumetric flowrate of anisole. Assuming there is no pressure drop and that the reactor is isothermal, the volumetric flowrate (v) can be rewritten as:

$$v = v_o(1 + \varepsilon X) \tag{13}$$

where v_o is the initial volumetric flowrate of anisole and ε is the extent of reaction. And the molar flowrate of anisole (F_A) can be rewritten as:

$$F_A = F_{AO}(1 - X) \tag{14}$$

Substituting equations (13) and (14) into equation (12) gives:

$$C_A = \frac{C_{AO}(1 - X)}{(1 + \varepsilon X)} \tag{15}$$

Substituting equation (15) into equation (11) gives:

$$r_A = \frac{-kC_{AO}(1-X)}{(1+\varepsilon X)} \tag{16}$$

Substituting equation (16) into equation (10) gives:

$$\frac{dX}{dW} = \frac{kC_{AO}(1-X)}{F_{AO}(1+\varepsilon X)} \tag{17}$$

which can be integrated from X=0 when W=0 to X=X when W=W which gives:

$$(1+\varepsilon)\ln\frac{1}{(1-X)} - \varepsilon X = -\frac{kC_{AO}W}{F_{AO}} \tag{18}$$

Equation (18) was rearranged to isolate for the rate constant (k). Conversions at steady-state were used to calculate the rate constants. The results of this analysis are shown in Figures 3.7 and 3.8. The activation energies were 72.8 and 159 kJ/mol for MoO_3/ZrO_2 and MoO_3/TiO_2, respectively. The activation energy calculated for the zirconia supported catalyst ($E_a = 159$ kJ/mol) is relatively close to the E_a found in literature (115 ± 2 kJ/mol) for anisole HDO using 10 wt. % MoO_3/ZrO_2 evaluated on the $300 - 340\ °C$ temperature range (Shetty et al., 2019).
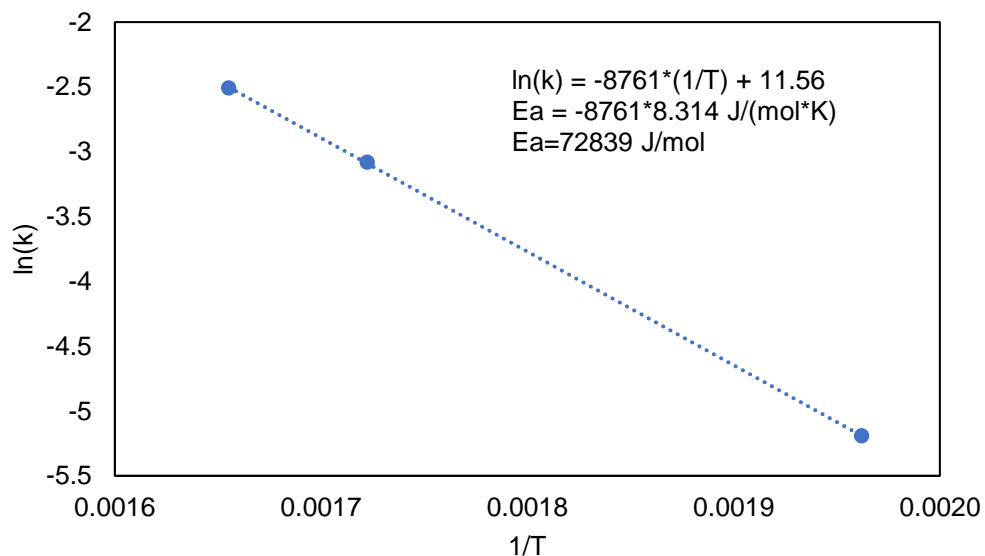

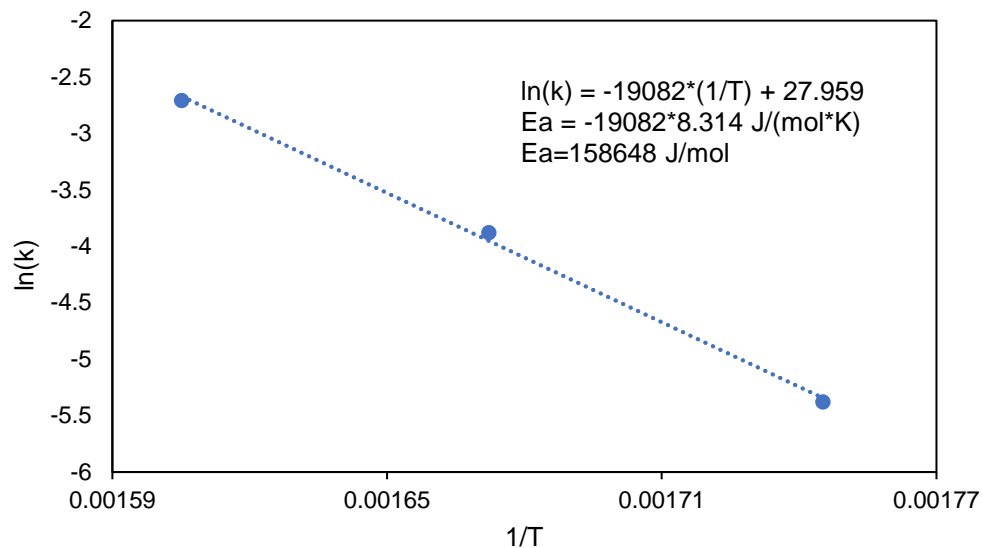**Figure 3.7 Arrhenius plot corresponding to the activity experiments with MoO_3/TiO_2**

55

The plot shows data points with the fitted equation:

$$\ln(k) = -19082 \cdot (1/T) + 27.959$$
$$E_a = -19082 \cdot 8.314 \ \text{J/(mol} \cdot \text{K)}$$
$$E_a = 158648 \ \text{J/mol}$$

The axes are labeled $\ln(k)$ (y-axis, ranging from -6 to -2) and $1/T$ (x-axis, ranging from 0.00159 to 0.00177).

Figure 3.8 Arrhenius plot corresponding to the activity experiments with MoO$_3$/ZrO$_2$

3.7.2 MoO$_3$/γ-Al$_2$O$_3$ Deactivation

The effect of reaction temperature on anisole conversion was studied for MoO$_3$/γ-Al$_2$O$_3$ (Figure 3.9). Surprisingly, the alumina supported catalyst had improved stability at the higher reaction temperatures, despite literature indicating a general and direct correlation between reaction temperature and the rate of coking (Zhou et al., 2016). The other possible route for MoO$_3$ (Mo^{6+}) deactivation is over-reduction to MoO$_2$ (Mo^{4+}). Increasing the reaction temperature, however, results in a higher degree of reduction and therefore a larger concentration of Mo^{4+} sites, as indicated by H$_2$-TPR, which are inactive for HDO. We therefore hypothesize that the faster rate of deactivation at lower temperatures is due to an increase in the number of strongly adsorbed phenol derivatives or oligomers of these species on the surface of the catalyst, which could block access to catalytic active sites or could directly lead to coke precursors. We thus hypothesize that the slower rate of catalyst deactivation at higher reaction temperatures is due to a decrease in the number of adsorbed phenolic species on the surface of the catalyst. TGA of the spent MoO$_3$/γ-Al$_2$O$_3$ samples in an inert atmosphere, such as nitrogen, should be performed to determine the amount of adsorbed phenolic species on each sample.

Although MoO$_3$/γ-Al$_2$O$_3$ initially had the highest activity of all the supported catalysts at 350 °C (Table 3.2), it rapidly deactivated from 98 to 18 % anisole conversion for the TOS of 65 to

200 min. It is possible that the deactivation was caused by coking as the acid sites of alumina are known to promote polymerization and polycondensation reactions (Zanuttini et al., 2014; Echeandia et al., 2014; Popov et al., 2010). TGA should be performed on the spent catalyst to measure the amount of coke deposited on its surface. Alternatively, the catalyst could have deactivated due to over-reduction of molybdenum oxide to Mo^{4+}.
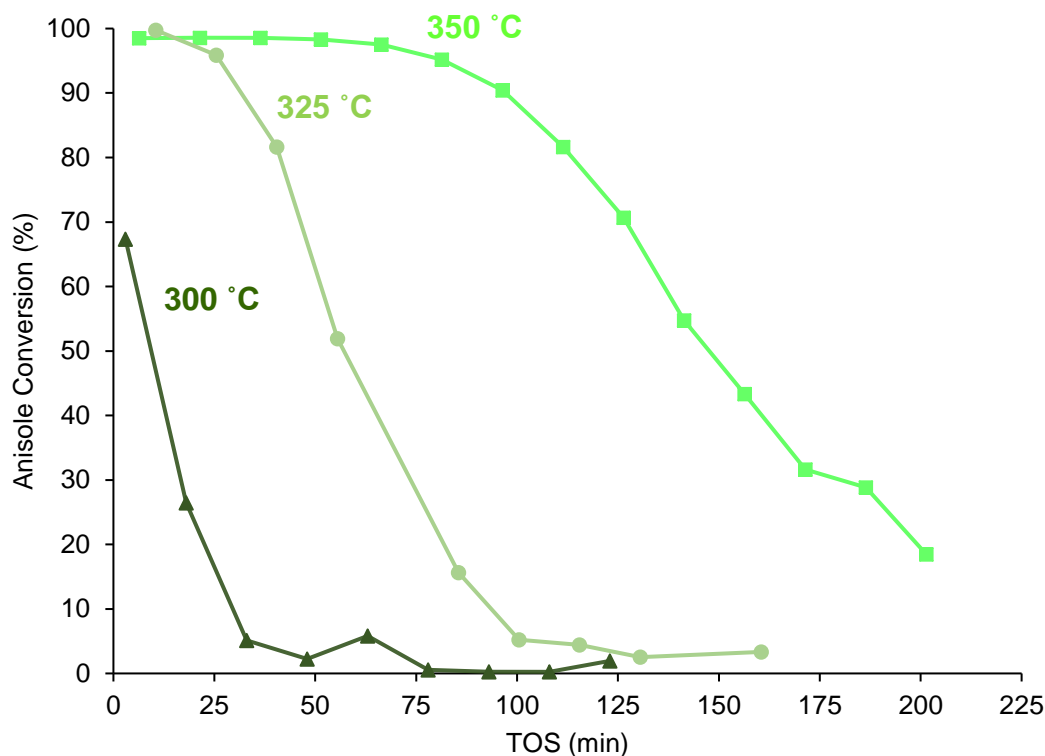

Figure 3.9 Activity data of anisole HDO on MoO3/γ-Al2O3 at 300 °C (dark green triangles), 325 °C (light olive green circles) and 350 °C (neon green squares). Reaction conditions: P_{Total} = 1.013 bar (0.0191 bar P_{Feed}, balance H_2), WHSV = 0.63 h^{-1} and TOS = 0 – 215 min.

3.8   Ex Situ UV-Vis Spectroscopy Results

The large absorption band seen in the UV-Vis spectra of bulk MoO_3 (Figure 3.10) is attributed to a ligand-to-metal charge transfer (LMCT) transition, where the valence band is generated by oxygen 2p π-orbitals and the conduction band is formed by overlapping metal 4d and 5s orbitals (Deb, 1968; Goodenough, 1971). The difference in energy between the highest occupied energy state of the valence band and the lowest unoccupied state of the conduction band is known as the band gap energy (Eg). The band gap energy is therefore a valuable tool

for evaluating the electronic structure of the catalyst and can be calculated by transforming the UV-Vis spectra (Figure 3.11) (Section 3.2.3.3).
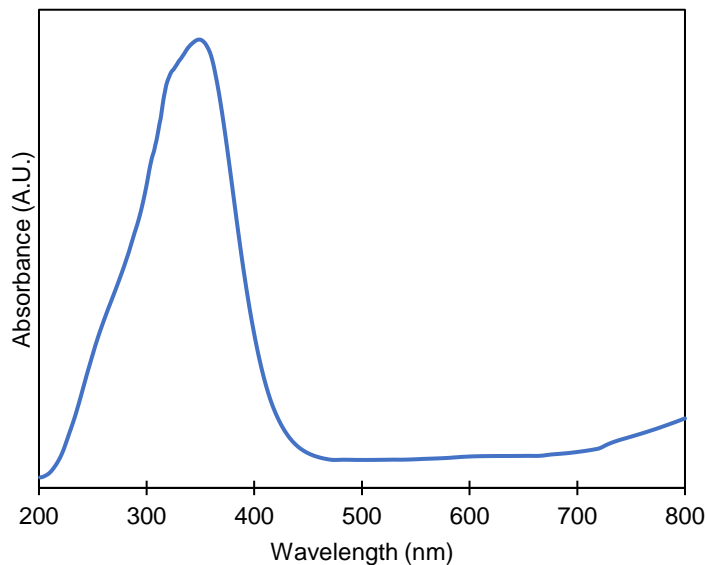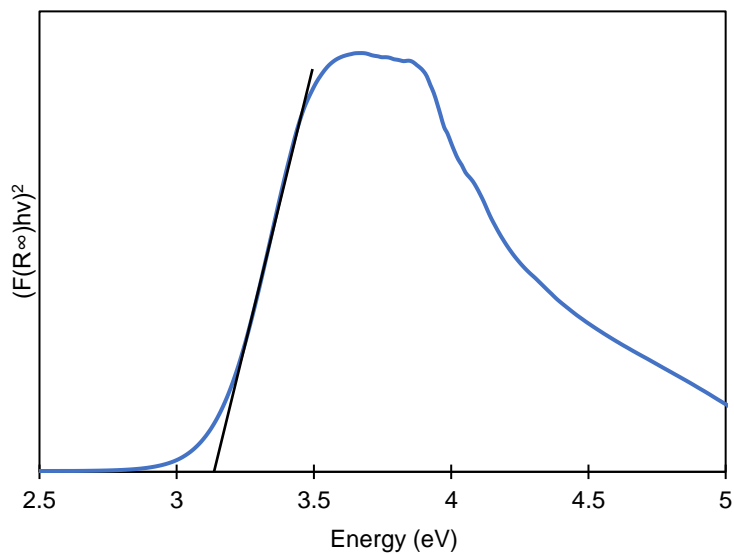

Figure 3.10 UV-Vis absorption spectrum of bulk MoO₃

Figure 3.11 Tauc plot of bulk MoO₃

The band gap energies (E_g) of the LMCT transitions of the bulk and supported MoO_3 catalysts are summarized in Table 3.3 and the corresponding UV-Vis spectra of the supported catalysts can be found in Appendix A. Researchers have found a linear indirect correlation between the band gap energy and the average number of adjacent molybdenum ions in oxide clusters

(Weber, 1995; Tian et al., 2010). Therefore, we can estimate the relative dispersion of the MoO$_3$ on the different supports via their band gap energy. It should be noted, however, that the Eg values only provide an average value of the MoO$_x$ cluster size and do not provide any information on the size distribution of the molybdenum oxide species that contribute to that average.

Table 3.2 UV–Vis DRS absorption-edge energies of supports and supported catalysts (10 wt.%).a,b

Catalyst	Band gap energy of support (eV)	Band gap energy of supported catalyst (eV)
MoO$_3$/TiO$_2$	3.60	3.02
MoO$_3$/CeO$_2$	3.24	2.76
MoO$_3$/ZrO$_2$	5.03	3.30
MoO$_3$/ γ-Al$_2$O$_3$	n/d	3.96
MoO$_3$/SiO$_2$	n/d	3.20
Bulk MoO$_3$	n/a	3.13

[a] n/d: not determined.
[b] n/a: not applicable.

The band gap energy for bulk MoO$_3$ was found to be 3.13 eV. This is in agreement with literature as MoO$_3$ is classified as an n-type semiconductor with indirect band gaps that have reported widths between 2.9 eV and 3.15 eV (Krylov, 1980; Erre et al., 1983). Small differences in these values are reported to be due to the difference in the number of oxygen vacancies in each sample (Liu et al., 2011). SiO$_2$ and Al$_2$O$_3$ are weak absorbers in the UV–Vis region, and their absorption can therefore be neglected whereas ZrO$_2$, TiO$_2$, and CeO$_2$ absorb strongly and their absorptions overlap with the LMCT transitions for Mo^{6+} species (Shetty et al., 2015).

Weber found that band gap energies at about 2.7, 3.0, 3.3, 3.9, and 4.3 eV correspond to [Mo$_6$O$_{19}$]$^{2-}$ polyanions, bulk MoO$_3$ and polyanions of [Mo$_7$O$_{24}$]$^{6-}$, [Mo$_2$O$_7$]$^{2-}$ and [MoO$_4$]$^{2-}$, respectively. The band gap energy of MoO$_3$/ γ-Al$_2$O$_3$ was 3.96 eV, indicating that the Mo

species were highly dispersed on this support and existed primarily as $[Mo_2O_7]^{2-}$ species (Weber, 1995). This value is consistent with results by Tian who found that 1 and 20 wt. % MoO_3 on γ-Al_2O_3 corresponded to band gap energies of 4.4 and 3.6 eV, respectively (Tian et al., 2010). The highest level of dispersion was thus achieved using the alumina supported catalyst as it had the largest band gap energy. The high level of dispersion can be attributed to its high surface area (Gonçalves et al., 2017; Xanes et al., 1995).

Although silica typically has a higher surface area than alumina, the MoO_3/SiO_2 catalyst has an Eg value of 3.20 eV, which is just below the Eg value of 3.30 eV corresponding to $[Mo_7O_{24}]^{6-}$ clusters but also just above the Eg value for bulk MoO_3 (up to 3.15 eV). A high level of dispersion was hence not obtained on silica. Low levels of metal oxide dispersion, however, are typical on SiO_2 due to the low reactivity and high acidity of its surface hydroxyls (Boer et al., 1991; Tian et al., 2010; Tsilomelekis & Boghosian, 2013). A study by Tian et al. found that the maximum loading of MoO_3 on SiO_2 was 5 wt. % (corresponding to a fraction of monolayer coverage of 0.20) before crystalline MoO_3 nanoparticles began to be formed (Tian et al., 2010). However, Shetty et al. used a loading of 10 wt. % for MoO_3 supported on SiO_2 and obtained a band gap energy of 4.1 eV, indicating the presence of sub-monolayer dispersed MoO_x species. We therefore decided to use the same 10 wt. % loading to see if we would get similar results. Nevertheless, our low band gap energy of 3.1 eV for MoO_3/SiO_2 indicates that the MoO_x species are not isolated and instead crystallization occurred with the MoO_x species existing in large clusters. This is consistent with the H_2-TPR results which showed a broad high temperature peak.

MoO_3/ZrO_2 has an Eg value of 3.30 eV, whereas the bare support had a much larger band gap energy of 5.03 eV. This shift is due to the presence of oligomeric MoO_x domains on the ZrO_2 surface (Tsilomelekis & Boghosian, 2013) and, according to Weber's empirical correlation, corresponds to $[Mo_7O_{24}]^{6-}$ polyanions. Like MoO_3/ZrO_2, the Eg value was lower for MoO_3/TiO_2 (3.02 eV) compared to the bare support (3.60 eV). However, the shift is much smaller compared to MoO_3/ZrO_2 which could be due to an overlapping of absorption bands of the support and the MoO_3 (Shetty et al., 2015). The band gap energy of 3.02 eV corresponds to bulk MoO_3, indicating that monolayer coverage was met or exceeded. Interestingly, MoO_3/CeO_2 has an Eg value of 2.76 eV, which corresponds to $[Mo_6O_{19}]^{2-}$ polyanions, meaning

that monolayer coverage was exceeded, crystallization occurred, and large clusters were formed. This means that MoO_x domains are more tightly packed upon incorporation of the CeO_2 support compared to that of their bulk structure MoO_3. One possible explanation for this could be because the catalysts were synthesized via impregnation, which is known to be more difficult at achieving high levels of dispersion compared to other methods (Deraz, 2018).

The level of MoO_x dispersion therefore decreased in the following order: MoO_3/γ-Al_2O_3 (3.96 eV) > MoO_3/ZrO_2 (3.30 eV) > MoO_3/SiO_2 (3.20 eV) > MoO_3/TiO_2 (3.02 eV) > MoO_3/CeO_2 (2.76 eV). This order is consistent with results obtained by Shetty et al., with the exception of MoO_3/SiO_2 (Shetty et al., 2015). In summary, among all formulations tested, the alumina supported catalyst achieved the highest level of dispersion, due to its high surface area, and the ceria supported catalyst had the lowest level of dispersion where it became a more tightly packed cubic structure than bulk MoO_3, possibly due to the catalyst synthesis method.

3.9   In Situ UV-Vis Results

The effect of temperature on the band gap energy of the supported and bulk MoO_3 catalysts for reduction (heating in H_2 atmosphere) and reaction (heating in H_2 and gas phase anisole) conditions was determined by in situ UV-Vis spectroscopy experiments run at the following temperatures: 150, 200, 250, 300 and 350 °C. The corresponding results for MoO_3/Al_2O_3, MoO_3/SiO_2 and bulk MoO_3 are shown in Figure 3.12 and results for MoO_3/TiO_2, MoO_3/ZrO_2, MoO_3/CeO_2 and bulk MoO_3 are shown in Figure 3.13. It should be noted, however, that band gap energy values were not determined for the MoO_3/ZrO_2 catalyst under the reaction conditions as a peak corresponding to anisole distorted the peak corresponding to the LMCT, thus preventing the E_g from accurately being determined. This did not occur for the other catalysts since they had much higher absorbances than the zirconia supported catalyst. In Figures 3.12 and 3.13, there are two main trends that are observed: 1) the band gap energy decreases with increasing temperatures for both the reaction and the reduction experiments and 2) the reduction and reaction experiments exhibit different values for the band gap energy at a given temperature.

The change in band gap energy can be attributed to a change in cluster size and/or a change in oxidation state (i.e. oxygen vacancy formation). Dieterle et al. observed an increase in band

gap energy from 2.90 to 2.97 eV with an increase in concentration of oxygen vacancies. The opposite trend is observed here. However, there was an observed change in catalyst colour, with the post reaction and reduction samples being blue/grey. This is indicative of oxygen vacancy formation as the sample colour is reported to change as a function of the degree of reduction with yellow (MoO_{3-x}) and grayish/blue (MoO_{3-y}) with $x < y$ (Dieterle et al., 2002; Whiffen & Smith, 2010; Tan et al., 2016). With regards to the cluster size, Weber proposed an inverse correlation between the band gap energy and the average number of adjacent molybdenum ions in small oxide clusters (Weber, 1995). Our results therefore indicate that the cluster size increases (i.e. crystallization occurs) with an increase in temperature for both the reduction and the reaction experiments. The difference in the degree of change for each catalyst could be due to the different metal – support interactions and surface areas of the supports. Our results indicate that cluster size has a greater impact on the band gap energy than the local Mo symmetry, consistent with the observations by Fournier et al. (Fournier et al., 1989).
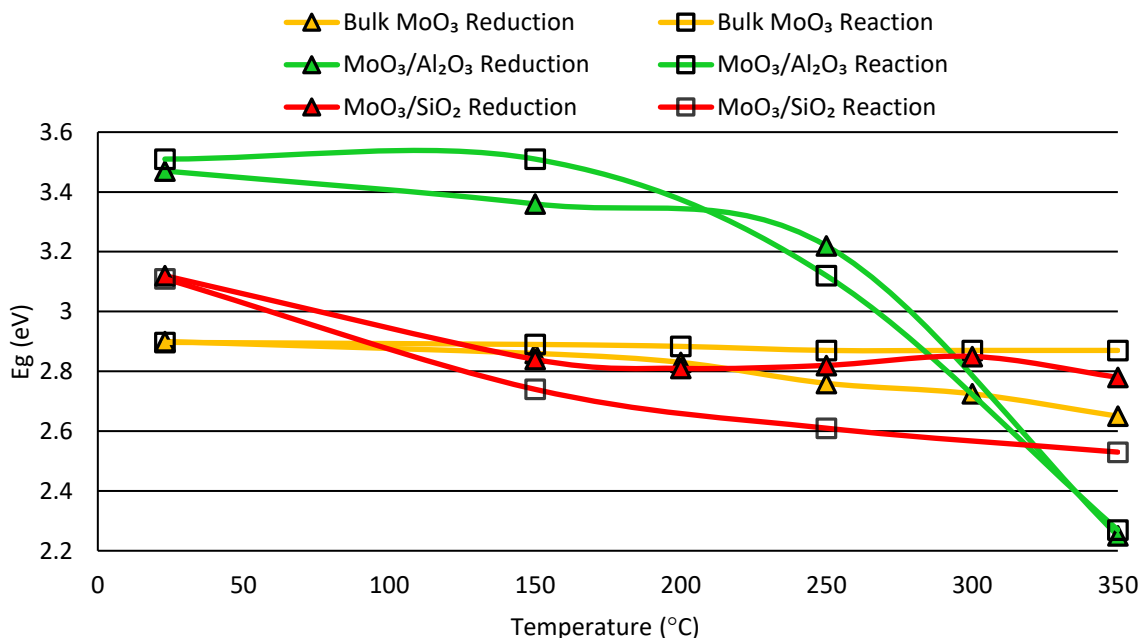

Figure 3.12 UV-Vis DRS Absorption Edge Energy (Eg) of supported and bulk MoO₃ catalysts for △ reduction in H₂ atmosphere and □ reaction at various temperatures.

Figure 3.13 UV-Vis DRS Absorption Edge Energy (Eg) of supported and bulk MoO₃ catalysts for △ reduction in H₂ atmosphere and ☐ reaction at various temperatures.
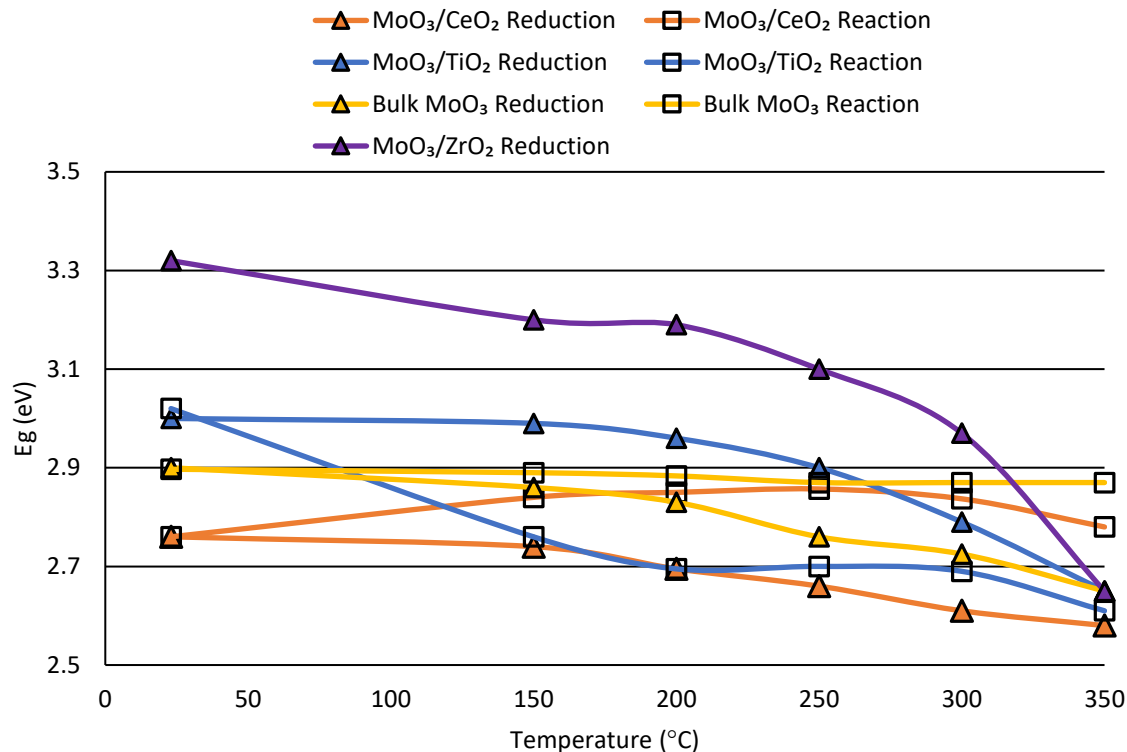
3.9.1   Band Gap Energy at 350 °C

The activity experiments indicate that a high temperature of at least 325 °C is required to obtain moderate levels of anisole conversion over the supported MoO_3 catalysts. Therefore, the most valuable information is the band gap energies corresponding to the reaction runs at 350 °C, as it provides information on the influence of cluster size on the catalyst's activity. The Eg values of the supported catalysts after undergoing the reaction atmosphere at 350 °C decreased in the following order: MoO_3/CeO_2 (2.78 eV) > MoO_3/TiO_2 (2.61 eV) > MoO_3/SiO_2 (2.53 eV) > $MoO_3/\gamma\text{-}Al_2O_3$ (2.27 eV). Therefore, the MoO_x cluster size, under reaction conditions, was the largest for the alumina supported catalyst and the lowest for the ceria supported catalyst. However, all the catalysts have band gap energies that are less than that of pristine bulk MoO_3 (2.9 eV to 3.15 eV) and therefore, corresponds to MoO_x clusters that are more tightly packed than that of bulk MoO_3. Interestingly, the Eg value of $MoO_3/\gamma\text{-}Al_2O_3$ at 350 °C for both reduction and reaction experiments was approximately 2.27 eV, which is less than the Eg value corresponding to $[Mo_6O_{19}]^{2-}$ polyanions (2.7 eV). Hence, agglomeration and crystallization of

MoO$_x$ was the most severe on the alumina supported catalyst post-reaction at 350 °C, possibly due to weaker metal – support interactions.

3.9.2   Total Change in Band Gap Energy

The difference in Eg values from the pre-run to the experimental run at 350 °C is also of interest as it reveals information on the degree of change of the cluster size. For the reaction experiments, the difference in Eg values of the supported catalysts decreases in the following order: MoO$_3$/γ-Al$_2$O$_3$ (1.24 eV) >> MoO$_3$/SiO$_2$ (0.58 eV) > MoO$_3$/TiO$_2$ (0.35 eV) > bulk MoO$_3$ (0.03 eV) > MoO$_3$/CeO$_2$ (-0.02 eV). For the reduction experiments, the difference in Eg values of the supported decreases in the following order: MoO$_3$/γ-Al$_2$O$_3$ (1.22 eV) >> MoO$_3$/ZrO$_2$ (0.67   eV) > MoO$_3$/TiO$_2$ (0.41 eV) > MoO$_3$/SiO$_2$ (0.34   eV) > bulk MoO$_3$ (0.25 eV) > MoO$_3$/CeO$_2$ (0.18 eV). Therefore, in general, the difference in Eg values of the catalysts from the pre-run to the run at 350 °C follow the same order for the reaction and reduction atmospheres. The presence of anisole, and therefore the potential for coking, has no effect on the order of decreasing Eg difference values of the supported catalysts. This is clear for the most acidic supported catalyst, with the highest ability for coke formation: MoO$_3$/γ-Al$_2$O$_3$. For this catalyst the Eg value after the reaction and reduction atmospheres were 2.25 and 2.27 eV, respectively.

For the reaction atmosphere (hydrogen and gas phase anisole), the band gap values for the MoO$_3$/TiO$_2$ and MoO$_3$/SiO$_2$ catalysts are similar at all the reaction temperatures tested as well as before the reaction occurred. However, although these catalysts had similar band gap values and therefore similar cluster sizes, they had very different HDO activities at 350 °C, as seen from Table 3.1, with MoO$_3$/TiO$_2$ and MoO$_3$/SiO$_2$ having anisole conversions of 50 and 5.5 %, respectively. Therefore, the cluster size does not seem to have a major effect on the catalyst's activity.

3.9.3   Mo^{5+} Absorption Band

The in situ UV-Vis spectra of the supported catalysts illustrates the formation of a new peak, for both the reduction (H$_2$ atmosphere) and reaction (H$_2$ and gas phase anisole atmosphere) experiments, at all the temperatures tested. An example of the corresponding Tauc plots for the UV-Vis spectra of the reduction and reaction experiments over MoO$_3$/TiO$_2$ are shown in

Figures 3.14 and 3.15, respectively. The spectra of the other supported MoO_3 catalysts and bulk MoO_3 can be found in Appendix A. It's proposed that this peak corresponds to the formation of an uncoordinated Mo species (Mo^{5+}) (Douvas et al., 2014; Tan et al., 2016; Luo et al., 2016; Braun et al., 2000). This indicates that oxygen vacancies, which are required to initiate HDO, were formed and the supported catalysts were reduced. Although this new absorption peak was not seen for the experiments with bulk MoO_3, the post reduction spectra had a significant increase in absorption in the UV-Vis range, which has also been attributed to the presence of oxygen vacancies (X. Li et al., 2014). The post reaction spectra of bulk MoO_3, however, did not have any increase in absorbances from the pre-run. Therefore, bulk MoO_3 was reduced in the reduction atmosphere and not in the reaction atmosphere. Since the reduction atmosphere does not contain any oxygen, oxygen vacancies are therefore easier to create whereas in the reaction atmosphere, the reverse Mars-van Krevelen mechanism occurs and the oxygen vacancies that are created are filled by anisole's oxygen atom.
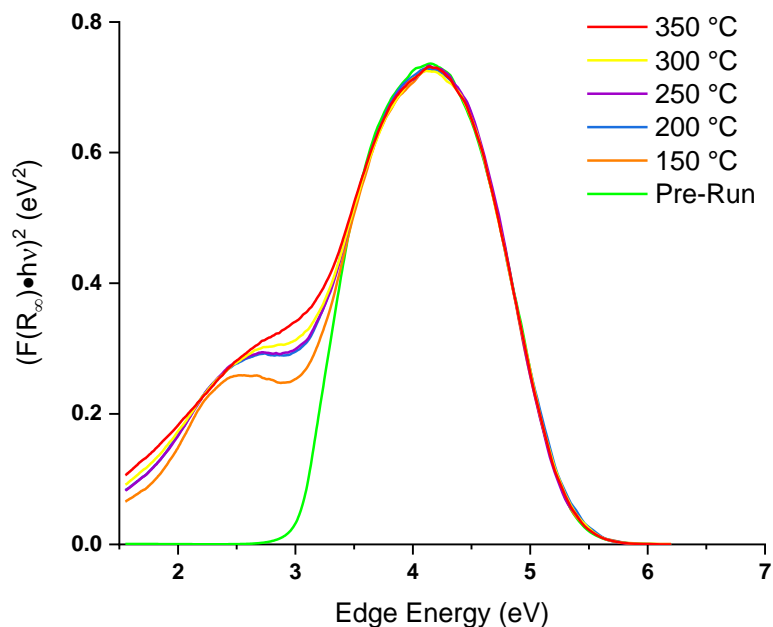

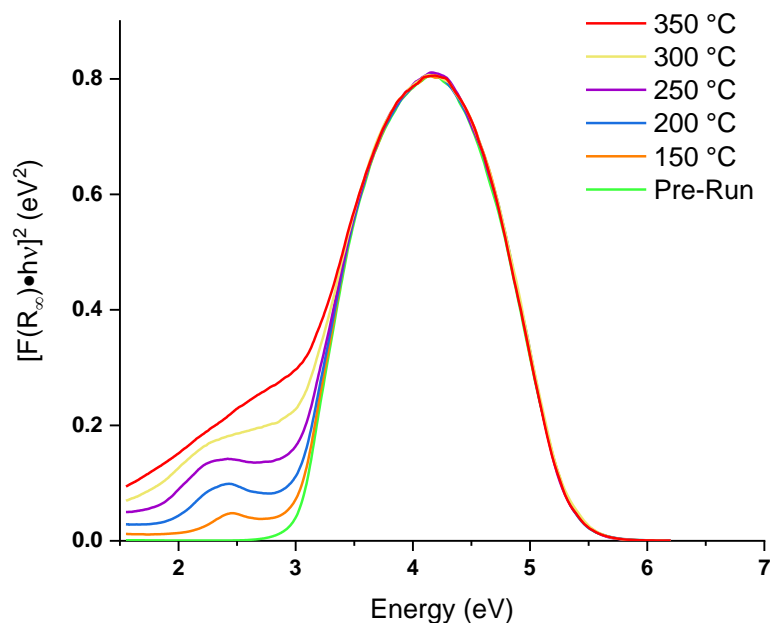**Figure 3.14 In situ UV-Vis spectra of MoO₃/TiO₂ under the reaction atmosphere**

Figure 3.15 In situ UV-Vis spectra of MoO$_3$/TiO$_2$ under the reduction atmosphere

The peak corresponding to Mo^{5+} is due to intervalence charge transfer (IVCT) which occurs when electrons jump between two different Mo atoms with different oxidation states (Mo^{5+} – O – Mo^{6+} → Mo^{6+} – O – Mo^{5+}) interchanging the oxidation states (Buckley & Clark, 1985). For example, Porter et al. observed these IVCT bands at 2.48 eV for MoO$_2$ (Mo^{4+}) , at 2.13, 2.42, and 1.3 eV for Mo$_4$O$_{11}$ (Mo^{5+}) and at 2.11 and 1.3 eV for Mo$_9$O$_{26}$ (Porter et al., 1972). Hence, there is a direct correlation between the blue shift of the IVCT absorption band and the degree of reduction of molybdenum oxide. Porter et al. found that the IVCT position is exponentially related to the number of charge carriers (i.e. the number of electrons per Mo atom) by applying Meyer's rule which is valid under the assumption that the band structure and mobility of the carriers does not change (Porter et al., 1972). Building on Porter's work, Dieterle et al. prepared a series of MoO$_{3-x}$ samples under different conditions and successfully used the empirical correlation to determine the degree of reduction of each MoO$_{3-x}$ sample (Dieterle et al., 2002). Using Porter's empirical correlation, we determined the degree of reduction of the spent supported catalysts for both the reaction and reduction in situ UV-Vis experiments (Figures 3.16 and 3.17, respectively).
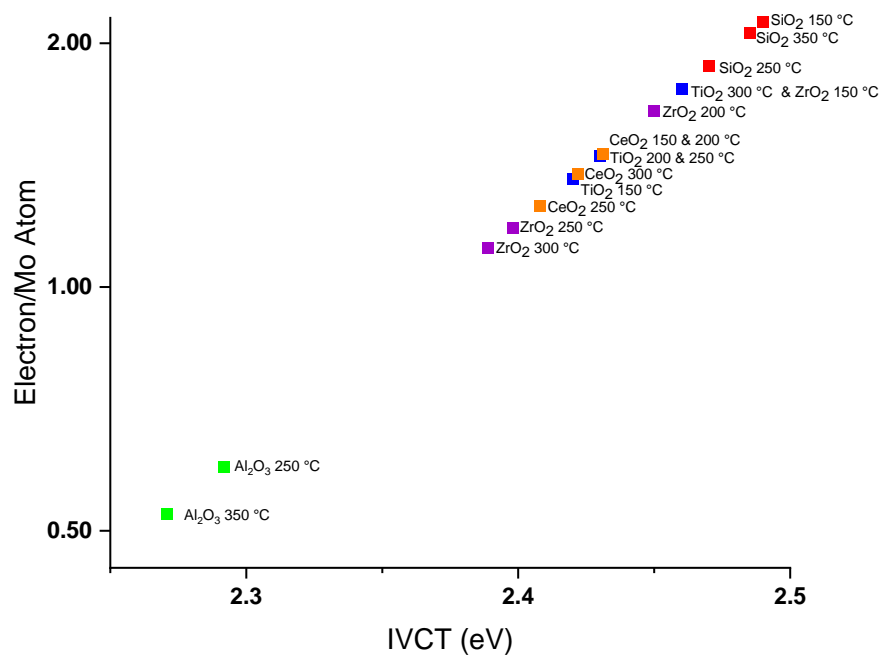
Figure 3.16 Position of the IVCT transition of the supported MoO₃ catalysts post in situ UV-Vis reaction (H₂ and gas phase anisole atmosphere) experiments
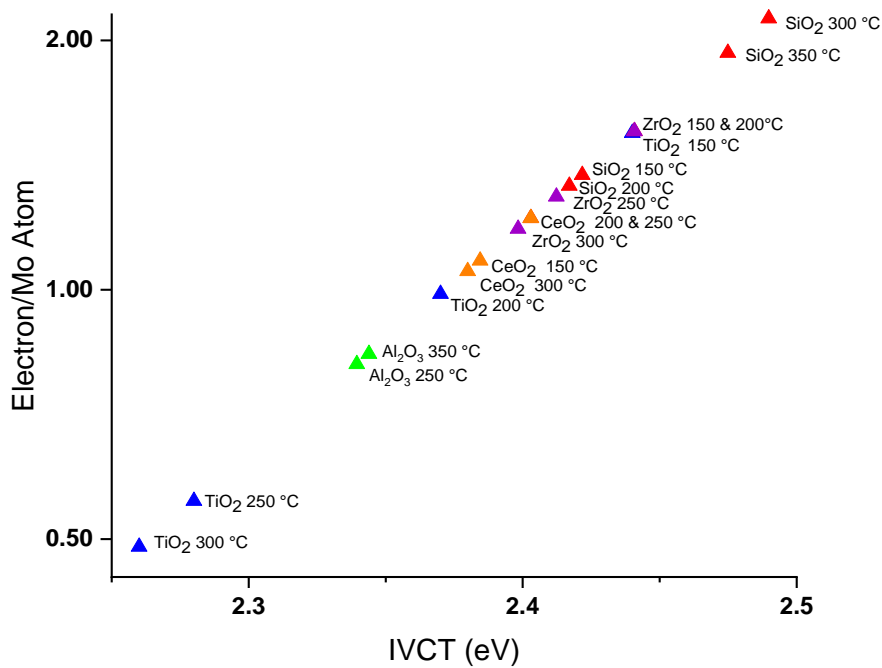

Figure 3.17 Position of the IVCT transition of the supported MoO₃ catalysts post in situ UV-Vis reduction (H₂ atmosphere) experiments

Higher operating temperatures result in an increased degree of reduction of molybdenum oxide, as evidenced by H_2-TPR. Therefore, increasing the operating temperature should result in a blue shift the IVCT absorption band (i.e. an increase in the IVCT position). This is true for the titania supported catalyst under the reaction atmosphere where the IVCT band position increased from 2.42 to 2.43 eV when the operating temperature increased from 150 to 200 and 250 °C, respectively, and from 2.43 to 2.46 eV when the operating temperature increased from 200 to 250 and 300 °C, respectively. These values are greater than the IVCT positions corresponding to the active site Mo^{5+} (2.13 and 2.42 eV) but less than the IVCT position of Mo^{4+} (2.48 eV) which is less active for HDO.

For the reaction atmosphere (H_2 and gas phase anisole), the alumina supported catalyst had IVCT positions of 2.27 and 2.29 eV for temperatures of 350 and 250 °C, respectively. These values are within the range of IVCT positions corresponding to Mo^{5+} (2.13 and 2.42 eV). These results strongly suggest that the rapid deactivation observed for the $MoO_3/\gamma-Al_2O_3$ is not due to an over-reduction of MoO_3 (Mo^{6+})$\rightarrow$ MoO_2 (Mo^{4+}) and instead is probably due to coking.

The IVCT values can also be used to justify anisole conversions obtained in the activity experiments. The IVCT positions of the supported catalysts for the reaction atmosphere at high temperatures (300 and 350 °C) decreased in the following order: $MoO_3/\gamma-Al_2O_3 \gg MoO_3/ZrO_2 > MoO_3/CeO_2 > MoO_3/TiO_2 > MoO_3/SiO_2$. In general, this order can be directly correlated with its catalytic activity, as the activity experiments had anisole conversion decrease in the following order: $MoO_3/\gamma-Al_2O_3 \gg MoO_3/TiO_2 > MoO_3/ZrO_2 \gg MoO_3/SiO_2$. Therefore, although $MoO_3/\gamma-Al_2O_3$ is not as reducible as MoO_3/TiO_2 and MoO_3/ZrO_2, it obtained higher anisole conversions likely due to its ability to preserve Mo^{5+} active sites.

The in-situ UV-Vis reaction spectra can also give insights for the low activity observed for the silica supported catalyst. For the reaction atmosphere, MoO_3/SiO_2 had IVCT positions of 2.49, 2.47 and 2.49 eV corresponding to temperatures of 150, 250 and 350 °C, respectively. These positions indicate that the silica supported catalyst over reduces to inactive Mo^{4+}. This is consistent with results by Shetty et al., where XPS spectra of MoO_3/SiO_2 indicated that it was the least effective at preventing the overreduction of molybdenum oxide to its inactive oxidation state of Mo^{4+} (Shetty et al., 2015). Furthermore, for the reduction atmosphere at 350 °C, the silica supported catalyst had an IVCT position corresponding to 2.48 eV. Therefore,

the IVCT position, and therefore the degree of reduction, was the same regardless of whether an oxygen-containing hydrocarbon (anisole) was present or not. The reduction atmosphere (H_2) can be regarded as one half of the reverse Mars-van Krevelen mechanism as there is no oxygen-containing compound present to complete the cycle. Since the degree of reduction was the same for the reduction and reaction atmospheres, this means that for the case of silica, anisole did not adsorb into most of the vacancies, completing the cycle.

The IVCT absorption bands of the supported catalysts obtained under the reaction atmosphere were integrated using Origin to find the corresponding peak areas. The values were plotted against the corresponding number of electrons per Mo atom calculated by Porter's empirical correlation (Figure 3.18). The peak areas were found to be directly proportional to the number of additional electrons (per Mo atom) gained by the Mo^{+6} after the reaction atmosphere (H_2 and gas phase anisole). Like the IVCT position, the peak area of the IVCT absorption band can therefore also be used to determine an approximate degree of reduction of molybdenum oxide.
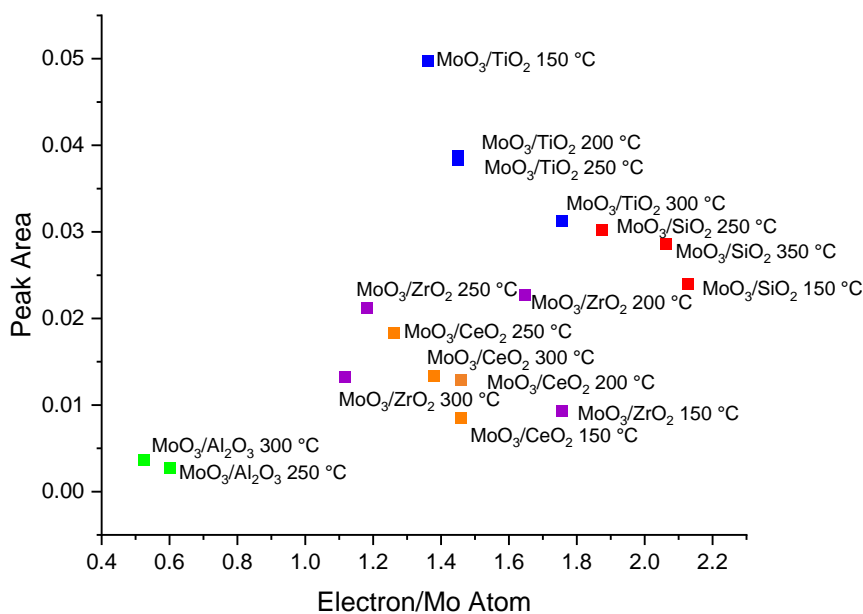

Figure 3.18 Peak area of the IVCT absorption band under the reaction (H_2 and gas phase anisole) atmosphere vs. the number of electrons per molybdenum atom

References

Alvarez-amparán, M. A., Guillén-aguilar, D., & Cedeño-caero, L. (2020). MoWFe based
catalysts to the oxidative desulfurization of refractory dibenzothiophene compounds : Fe
promoting the catalytic performance. *Fuel Processing Technology*, *198*, 106233.
https://doi.org/10.1016/j.fuproc.2019.106233

Arena, F., & Parmaliana, A. (1996). Silica-supported molybdena catalysts. Surface
structures, reduction pattern, and oxygen chemisorption. *Journal of Physical Chemistry*,
100(51), 19994–20005. https://doi.org/10.1021/jp9618587

Arnoldy, P., De Jonge, J. C. M., & Moulijn, J. A. (1985). Temperature-programed reduction
of molybdenum(VI) oxide and molybdenum(IV) oxide. *The Journal of Physical
Chemistry*, *89*(21), 4517–4526. https://doi.org/10.1021/j100267a021

Boer, M. De, Dillen, A. J. Van, Koningsberger, D. C., & Geus, J. W. (1991). Remarkable
spreading behavior of molybdena on silica catalysts . An in situ EXAFS-Raman study.
Catalysis Letters, *11*, 227–240.

Boullosa-eiras, S., Lødeng, R., Bergem, H., Stöcker, M., Hannevold, L., & Blekkan, E. A.
(2014). Catalytic hydrodeoxygenation (HDO) of phenol over supported molybdenum
carbide , nitride , phosphide and oxide catalysts. *Catalysis Today*, *223*, 44–53.
https://doi.org/10.1016/j.cattod.2013.09.044

Braun, S., Appel, L. G., Camorim, V. L., & Schmal, M. (2000). Thermal Spreading of MoO3
onto Silica Supports. *Journal of Physical Chemistry*, *104*, 6584–6590.
https://doi.org/10.1021/jp000287m

Buckley, I. R., & Clark, R. R. (1985). Structural and Electronic Properties of some
Polymolybdates Reducible to Molybdenum Blues. *Coordination Chemistry Reviews*, *65*,
167–218.

Cedeno-Caero, L., & Alvarez-Amparan, M. A. (2014). Performance of molybdenum oxide in
spent hydrodesulfurization catalysts applied on the oxidative desulfurization process of
dibenzothiophene compounds. *Reaction Kinetics, Mechanics and Catalysis*, *113*, 115–

131. https://doi.org/10.1007/s11144-014-0729-8

Chary, K. V. R., Rajender, K., Kishan, G., Niemantsverdriet, J. W., & Mestl, G. (2004).
Structure and catalytic properties of molybdenum oxide catalysts supported on zirconia.
Journal of Catalysis, *226*, 283–291. https://doi.org/10.1016/j.jcat.2004.04.028

Cordero, R. L., & Agudo, A. L. (2000). Effect of water extraction on the surface properties of
Mo/Al2O3 and NiMo/Al2O3 hydrotreating catalysts. *Applied Catalysis A : General*,
202, 23–35.

Deb, S. K. (1968). Physical properties of a transition metal oxide : optical and photoelectric
properties of single crystal and thin film molybdenum trioxide. *Proceedings of the
Royal Society*, *304*, 211–231.

Deraz, N. M. (2018). The comparative jurisprudence of catalysts preparation methods : I .
precipitation and impregnation methods. *Chemistry*, *2*(1), 19–21.

Dieterle, M., Weinberg, G., & Mestl, G. (2002). Raman spectroscopy of molybdenum oxides
- Part I. Structural characterization of oxygen defects in MoO3-x by DR UV/VIS,
Raman spectroscopy and X-ray diffraction. *Physical Chemistry Chemical Physics*, *4*(5),
812–821. https://doi.org/10.1039/b107012f

Douvas, A. M., Vasilopoulou, M., Georgiadou, D. G., Soultati, A., Davazoglou, D., Vourdas,
N., Giannakopoulos, K. P., Kontos, A. G., Kennou, S., & Argitis, P. (2014). Sol-gel
synthesized, low-temperature processed, reduced molybdenum peroxides for organic
optoelectronics applications. *Journal of Materials Chemistry C*, *2*(31), 6290–6300.
https://doi.org/10.1039/c4tc00301b

Echeandia, S., Pawelec, B., Barrio, V. L., Arias, P. L., Cambra, J. F., Loricera, C. V., &
Fierro, J. L. G. (2014). Enhancement of phenol hydrodeoxygenation over Pd catalysts
supported on mixed HY zeolite and Al2O3. An approach to O-removal from bio-oils.
Fuel, *117*, 1061–1073. https://doi.org/10.1016/j.fuel.2013.10.011

Erre, R., Legay, M. H., & Fripiat, J. J. (1983). Reaction of molecular hydrogen with the 100
face of MoO3: II. Kinetics initiated by atomic hydrogen and characterization of the

surface electronic state. *Surface Science*, *127*(1), 69–82.

Fournier, M., Louis, C., Che, M., Chaquin, P., & Masure, D. (1989). Polyoxometallates as Models for Oxide Catalysts Part I . An UV-Visible Reflectance Study of Polyoxomolybdates : Influence of. *Journal of Catalysis*, *119*, 400–414.

Giordano, F., Trovarelli, A., Leitenburg, C. De, & Giona, M. (2000). *A Model for the Temperature-Programmed Reduction of Low and High Surface Area Ceria*. *282*, 273–282. https://doi.org/10.1006/jcat.2000.2900

Gonçalves, V. O. O., Ciotonea, C., Arrii-Clacens, S., Guignard, N., Roudaut, C., Rousseau, J., Clacens, J. M., Royer, S., & Richard, F. (2017). Effect of the support on the hydrodeoxygenation of m-cresol over molybdenum oxide based catalysts. *Applied Catalysis B: Environmental*, *214*, 57–66. https://doi.org/10.1016/j.apcatb.2017.05.003

Goodenough, J. B. (1971). Metallic Oxides. *Progress in Solid State Chemistry*, *5*, 145–399.

Hahn, T., Bentrup, U., Armbrüster, M., Kondratenko, E. V, & Linke, D. (2014). The Enhancing Effect of Brønsted Acidity of Supported MoOx Species on their Activity and Selectivity in Ethylene / trans -2-Butene Metathesis. *ChemCatChem*, *6*, 1664–1672. https://doi.org/10.1002/cctc.201400040

He, Z., Yang, M., Wang, X., Zhao, Z., & Duan, A. (2012). Effect of the transition metal oxide supports on hydrogen production from bio-ethanol reforming. *Catalysis Today*, *194*(1), 2–8. https://doi.org/10.1016/j.cattod.2012.05.004

Heracleous, E., Machli, M., Lemonidou, A. A., & Vasalos, I. A. (2005). Oxidative dehydrogenation of ethane and propane over vanadia and molybdena supported catalysts. *Journal of Molecular Catalysis A: Chemical*, *232*, 29–39. https://doi.org/10.1016/j.molcata.2005.01.027

Kaluža, L., Gulková, D., Vít, Z., & Zdražil, M. (2007). Effect of support type on the magnitude of synergism and promotion in CoMo sulphide hydrodesulphurisation catalyst. *Applied Catalysis A: General*, *324*(1–2), 30–35. https://doi.org/10.1016/j.apcata.2007.02.050

Krylov, O. V. (1980). *Catalysis by Non-Metals*. Academic Press.

Kydd, R., Teoh, Y., Scott, J., Ferri, D., & Amal, R. (2009). Probing Surface Properties and Reaction Intermediates During Heterogeneous Catalytic Oxidation of Acetaldehyde. *ChemCatChem*, *1*, 286–294. https://doi.org/10.1002/cctc.200900099

Li, X., Liu, L., Wang, A., Wang, M., Wang, Y., & Chen, Y. (2014). Creation of oxygen vacancies in MoO3/SiO2 by thermal decomposition of pre-impregnated citric acid under N2and their positive role in oxidative desulfurization of dibenzothiophene. *Catalysis Letters*, *144*(3), 531–537. https://doi.org/10.1007/s10562-013-1141-0

Liu, X., He, Y., Wang, S., & Zhang, Q. (2011). Preparation of MoO2 sub-micro scale sheets and their optical properties. *Journal of Alloys and Compounds*, *509*(SUPPL. 1), S408–S411. https://doi.org/10.1016/j.jallcom.2011.01.089

Lødeng, R., Ranga, C., Rajkhowa, T., Alexiadis, V. I., Bjørkan, H., Chytil, S., Svenum, I. H., Walmsley, J., & Thybaut, J. W. (2017). Hydrodeoxygenation of phenolics in liquid phase over supported MoO3 and carburized analogues. *Biomass Conversion and Biorefinery*, *7*(3), 343–359. https://doi.org/10.1007/s13399-017-0252-z

Luo, Z., Miao, R., Huan, T. D., Mosa, I. M., Poyraz, A. S., Zhong, W., Cloud, J. E., Kriz, D. A., Thanneeru, S., He, J., Zhang, Y., Ramprasad, R., & Suib, S. L. (2016). Mesoporous MoO3–x Material as an Efficient Electrocatalyst for Hydrogen Evolution Reactions. *Advanced Energy Materials*, *6*(16). https://doi.org/10.1002/aenm.201600528

Maity, S. K., Rana, M. S., Bej, S. K., Ancheyta-Juárez, J., Murali Dhar, G., & Prasada Rao, T. S. R. (2001). Studies on physico-chemical characterization and catalysis on high surface area titania supported molybdenum hydrotreating catalysts. *Applied Catalysis A: General*, *205*(1–2), 215–225. https://doi.org/10.1016/S0926-860X(00)00567-6

Nimmanwudipong, T., Ron C., R., Block, D. E., & Gates, B. C. (2011). Catalytic Reactions of Guaiacol : Reaction Network and Evidence of Oxygen Removal in Reactions with Hydrogen. *Catalysis Letters*, *141*, 779–783. https://doi.org/10.1007/s10562-011-0576-4

Popov, A., Kondratieva, E., Goupil, J. M., Mariey, L., Bazin, P., Gilson, J., Travert, A., &

Mauge, F. (2010). Bio-oils Hydrodeoxygenation : Adsorption of Phenolic Molecules on Oxidic Catalyst Supports. *Journal of Physical Chemistry*, 15661–15670. https://doi.org/10.1021/jp101949j

Porter, V. R., White, W. B., & Roy, R. (1972). Optical spectra of the intermediate oxides of titanium, vanadium, molybdenum, and tungsten. *Journal of Solid State Chemistry*, *4*(2), 250–254. https://doi.org/10.1016/0022-4596(72)90113-2

Prasomsri, T., Nimmanwudipong, T., & Román-Leshkov, Y. (2013). Effective hydrodeoxygenation of biomass-derived oxygenates into unsaturated hydrocarbons by MoO3 using low H2 pressures. *Energy & Environmental Science*, *6*(6), 1643–1972. https://doi.org/10.1039/C3EE24360E

Ranga, C., Lødeng, R., Alexiadis, V. I., Rajkhowa, T., Bjørkan, H., Chytil, S., Svenum, I. H., Walmsley, J., Detavernier, C., Poelman, H., Voort, P. Van Der, & Thybaut, J. W. (2018). Effect of composition and preparation of supported MoO3 catalysts for anisole hydrodeoxygenation. *Chemical Engineering Journal*, *335*(April 2017), 120–132. https://doi.org/10.1016/j.cej.2017.10.090

Ressler.T, Jentoft, R. E., Wienold, J., Gunter, M. M., & Timpe, O. (2000). In Situ XAS and XRD Studies on the Formation of Mo Suboxides during Reduction of MoO3. *Journal of Physical Chemistry*, *104*, 6360–6370. https://doi.org/10.1021/jp000690t

Runnebaum, R. C., Nimmanwudipong, T., Block, D., & Gates, B. C. (2012). Catalytic conversion of compounds representative of lignin-derived bio-oils: a reaction network for guaiacol, anisole, 4-methylanisole, and cyclohexanone conversion catalysed by Pt/Al2O3. *Catalysis Science & Technology*, *2*, 113–118. https://doi.org/10.1039/C1CY00169H

Shetty, M., Anderson, E. M., Green, W. H., & Román-leshkov, Y. (2019). Kinetic analysis and reaction mechanism for anisole conversion over zirconia-supported molybdenum oxide. *Journal of Catalysis*, *376*, 248–257. https://doi.org/10.1016/j.jcat.2019.06.046

Shetty, M., Murugappan, K., Green, W. H., & Roma, Y. (2017). Structural Properties and Reactivity Trends of Molybdenum Oxide Catalysts Supported on Zirconia for the

Hydrodeoxygenation of Anisole. *ACS Sustainable Chemistry and Engineering*, *5*, 5293−5301. https://doi.org/10.1021/acssuschemeng.7b00642

Shetty, M., Murugappan, K., Prasomsri, T., Green, W. H., & Román-Leshkov, Y. (2015). Reactivity and stability investigation of supported molybdenum oxide catalysts for the hydrodeoxygenation (HDO) of m-cresol. *Journal of Catalysis*, *331*, 86–97. https://doi.org/10.1016/j.jcat.2015.07.034

Tan, X., Wang, L., Cheng, C., Yan, X., Shen, B., & Zhang, J. (2016). Plasmonic MoO3-x@MoO3 nanosheets for highly sensitive SERS detection through nanoshell-isolated electromagnetic enhancement. *Chemical Communications*, *52*(14), 2893–2896. https://doi.org/10.1039/c5cc10020h

Tian, H., Roberts, C. A., & Wachs, I. E. (2010). Molecular structural determination of molybdena in different environments: Aqueous solutions, bulk mixed oxides, and supported MoO3 catalysts. *Journal of Physical Chemistry C*, *114*(33), 14110–14120. https://doi.org/10.1021/jp103269w

Tsilomelekis, G., & Boghosian, S. (2010). Structural and vibrational properties of molybdena catalysts supported on alumina and zirconia studied by in situ Raman and FTIR spectroscopies combined with 18O/16O isotopic substitution. *Catalysis Today*, *158*(1–2), 146–155. https://doi.org/10.1016/j.cattod.2010.06.026

Tsilomelekis, G., & Boghosian, S. (2013). On the configuration, molecular structure and vibrational properties of MoO$_x$ site s on alumina, zirconia, titania and silica. *Catalysis Science and Technology*, *3*(8), 1869–1888. https://doi.org/10.1039/c3cy00057e

Tsilomelekis, G., Christodoulakis, A., & Boghosian, S. (2007). Support effects on structure and activity of molybdenum oxide catalysts for the oxidative dehydrogenation of ethane. *Catalysis Today*, *127*, 139–147. https://doi.org/10.1016/j.cattod.2007.03.026

Wan, H., Li, D., Zhu, H., Zhang, Y., Dong, L., Hu, Y., Liu, B., Sun, K., Dong, L., & Chen, Y. (2008). Journal of Colloid and Interface Science A comparative study on the dispersion behaviors and surface acid properties of molybdena on CeO 2 and ZrO 2 (

Tet). *Journal of Colloid and Interface Science*, *326*, 28–34.

  https://doi.org/10.1016/j.jcis.2008.07.036

Weber, R. S. (1995). Effect of Local Structure on the UV-Visible Absorption Edges of

  Molybdenum Oxide. In *Journal of Catalysis* (Vol. 151, pp. 470–474).

Whiffen, V. M. L., & Smith, K. J. (2010). Hydrodeoxygenation of 4-Methylphenol over

  Unsupported MoP, MoS2, and MoOx Catalysts. *Energy & Fuels*, *24*(6), 4728–4737.

  https://doi.org/10.1021/ef901270h

Xanes, M. L., Hu, H., Wachs, I. E., Drive, A., & Bare, S. R. (1995). Surface Structures of

  Supported Molybdenum Oxide Catalysts : Characterization by Raman and Mo Ls-Edge

  XANES. *Journal of Physical Chemistry*, *99*(27), 10897–10910.

  https://doi.org/10.1021/j100027a034

Yun, S., & Guliants, V. V. (2019). Support Effects on Water Gas Shift Activity and Sulfur

  Dependence of Mo Sulfide Catalysts. *Energy & Fuels*, *33*, 11655−11662.

  https://doi.org/10.1021/acs.energyfuels.9b02470

Zanuttini, M. S., Costa, B. O. D., Querini, C. A., & Peralta, M. A. (2014).

  Hydrodeoxygenation of m-cresol with Pt supported over mild acid materials. *Applied*

  Catalysis A, General, *482*, 352–361. https://doi.org/10.1016/j.apcata.2014.06.015

Zhang, X., Liu, Q., Zhang, Q., Liu, Q., Chen, L., Li, Y., Wang, C., & Ma, L. (2019).

  Aromatic fuel production from phenolics by catalytic hydrodeoxygenation over novel

  Mo-based catalyst. *Energy Procedia*, *158*, 984–990.

  https://doi.org/10.1016/j.egypro.2019.01.240

Zhou, G., Jensen, P. A., Le, D. M., Knudsen, N. O., & Jensen, A. D. (2016). Atmospheric

  Hydrodeoxygenation of Biomass Fast Pyrolysis Vapor by MoO3. *ACS Sustainable*

  Chem, *4*, 5432−5440. https://doi.org/10.1021/acssuschemeng.6b00757

Zhu, H., Shen, M., Wu, Y., Li, X., Hong, J., Liu, B., Wu, X., Dong, L., & Chen, Y. (2005).

  Dispersion Behaviors of Molybdena on Titania (Rutile and / or Anatase). *Journal of*

  Physical Chemistry, *109*, 11720–11726. https://doi.org/10.1021/jp050890a

Chapter 4

4   Conclusion and Future Work/Recommendations

4.1   Conclusion

For all Mo-based catalysts tested in this study, the addition of a support increased the reducibility of the MoO_x species, as evidenced by H_2-TPR, with MoO_3/ZrO_2 and MoO_3/TiO_2 being the most reducible. Ex situ UV-Vis spectroscopy indicated that the level of MoO_x dispersion decreased in the following order: MoO_3/γ-Al_2O_3 (3.96 eV) > MoO_3/ZrO_2 (3.30 eV) > MoO_3/SiO_2 (3.20 eV) > MoO_3/TiO_2 (3.02 eV) > MoO_3/CeO_2 (2.76 eV). The effect of the reaction conditions (H_2 + anisole at 150 to 300 °C) on the cluster size of MoO_x species was also evaluated via in situ UV-Vis spectroscopy. MoO_x species migrated on the support surface during the reaction and when the reaction temperature was 350 °C, the spent catalysts had MoO_x domains that were more tightly packed than those of bulk MoO_3, with the degree of crystallinity decreasing in the following order: MoO_3/γ-Al_2O_3 (2.27 eV) > MoO_3/SiO_2 (2.53 eV) > MoO_3/TiO_2 (2.61 eV) > MoO_3/CeO_2 (2.78 eV). Comparison between reaction (H_2 + anisole) and reduction (H_2 only) atmospheres indicated that coking had no influence on the cluster size of MoO_x. Although MoO_3/SiO_2 had low HDO activity (5.5 % anisole conversion) whereas MoO_3/TiO_2 had high activity (50 %), they had similar band gap values before and after the in situ UV-Vis reaction atmosphere experiments. Therefore, molybdenum oxide cluster size did not have a major effect on the HDO activity.

Under both the reduction and reaction atmospheres, the in situ UV-Vis spectra of all the supported catalysts showed a new peak corresponding to an intervalence charge transfer (IVCT), indicating the formation of oxygen vacancies, where $Mo^{5+} - O - Mo^{6+} \rightarrow Mo^{6+} - O - Mo^{5+}$. Meyer's rule was applied to estimate the degree of reduction of the spent catalysts based on their IVCT position. The IVCT peak area was found to also be able to estimate the oxidation state of Mo species as there is a direct relationship between the IVCT absorption band peak area and the IVCT position.

A direct correlation was generally observed between the supported catalyst's catalytic activity for HDO and its ability to preserve Mo^{5+} sites, preventing over-reduction to less active Mo^{4+}

sites. The low anisole conversion (5.5 %) using MoO_3/SiO_2 at 350 °C can be explained by the catalyst's high average concentration of Mo^{4+} sites. Conversely, $MoO_3/\gamma\text{-}Al_2O_3$ had the highest average concentration of Mo^{5+} sites which justifies why it obtained the highest activity of all the supported catalysts with an average conversion of 98 % for the first 65 min TOS at 350 °C. However, $MoO_3/\gamma\text{-}Al_2O_3$ suffered from rapid deactivation with only 18 % conversion at 200 min TOS. Although the alumina supported catalyst had high anisole conversions for the TOS of 0 to 65 min, it had low selectivity towards benzene and toluene (6.1 and 2.7 %, respectively) and high selectivity towards phenol, averaging 49 %. This catalyst may follow a different mechanism for HDO than MoO_3/ZrO_2 and MoO_3/TiO_2, as they had higher selectivities towards benzene (61 and 42 %, respectively) and toluene (17 and 10 %, respectively) at 350 °C. The zirconia and titania supported catalysts not only resulted in high selectivities towards deoxygenated products, but they also maintained their stabilities and obtained relatively high steady-state conversions (46 and 50 %, respectively) at 350 °C. These catalysts were the most reducible of the supported MoO_3 catalysts, though the zirconia and titania supports were not as effective as $\gamma\text{-}Al_2O_3$ at stabilizing the Mo^{5+} species. This work shows that supported MoO_3 catalysts are effective catalysts for HDO provided that they are not only reducible but are also able to preserve Mo^{5+}, which serve as the active site for HDO, preventing over-reduction to inactive Mo^{4+}.

Increasing the reaction temperature from 300 to 350 °C resulted in increased stability of $MoO_3/\gamma\text{-}Al_2O_3$. In HDO with MoO_3 based catalysts, there are two main routes for deactivation: coking and over-reduction to Mo^{4+}. Since higher reaction temperatures are known to increase the rates of coking as well as increase the number of oxygen vacancies, the observed deactivation is unlikely to be due to either of these two reasons. Also, the IVCT peak position of the alumina supported catalyst indicated that it had the highest average number of Mo^{5+} sites which further supports the theory that the main cause of the deactivation was not due to the catalyst being over-reduced. Instead, we hypothesize that the faster rate of deactivation at lower temperatures is due to an increase in the number of strongly adsorbed phenolic species on the catalyst surface, which would block access to catalytic active sites and could directly lead to coke precursors.

4.2 Future Work/Recommendations

Future activity experiments should be performed for anisole HDO over MoO_3/TiO_2 and MoO_3/ZrO_2 at higher reaction temperatures ($350 - 400$ °C) to determine the optimal temperature for maximum benzene and toluene yields while also considering catalyst stability due to coking as well as the potential to produce cracked products.

The supported MoO_3 catalysts should undergo in situ near ambient pressure X-ray photoelectron spectroscopy (NAP-XPS) to determine the Mo oxidation states during the reaction. This will determine the validity of estimating the degrees of reduction based on the catalyst's IVCT position. Also, the observed crystallinity of the spent supported catalysts via in situ UV-Vis spectroscopy could be confirmed by performing in situ powder X-ray diffraction (PXRD) and in situ Raman spectroscopy. Of the as-synthesized supported catalysts, MoO_3/γ-Al_2O_3 had the highest degree of dispersion and it was believed to be due to a high surface area of the γ-Al_2O_3 support. The Brunauer–Emmett–Teller (BET) surface areas of the catalysts and supports could be determined by N_2 adsorption to confirm this hypothesis. Finally, the amount of carbon deposited on the surface of the catalysts must be determined by TGA in air. The amount of strongly adsorbed phenolic species (potentially responsible for catalyst deactivation) can be determined by TGA in an inert atmosphere such as nitrogen.

Appendices

Appendix A: The absorbance spectra of the blank supports and supported MoO_3 catalysts and the corresponding Tauc plots are shown below. The Appendix A also includes the Tauc plots of the in situ UV-Vis plots for the SiO_2, Al_2O_3, CeO_2, ZrO_2 supported and bulk MoO_3 catalysts under the reaction and reduction conditions. The activity data of all the supported catalysts are also shown in a figure with anisole conversion with respect to the TOS.
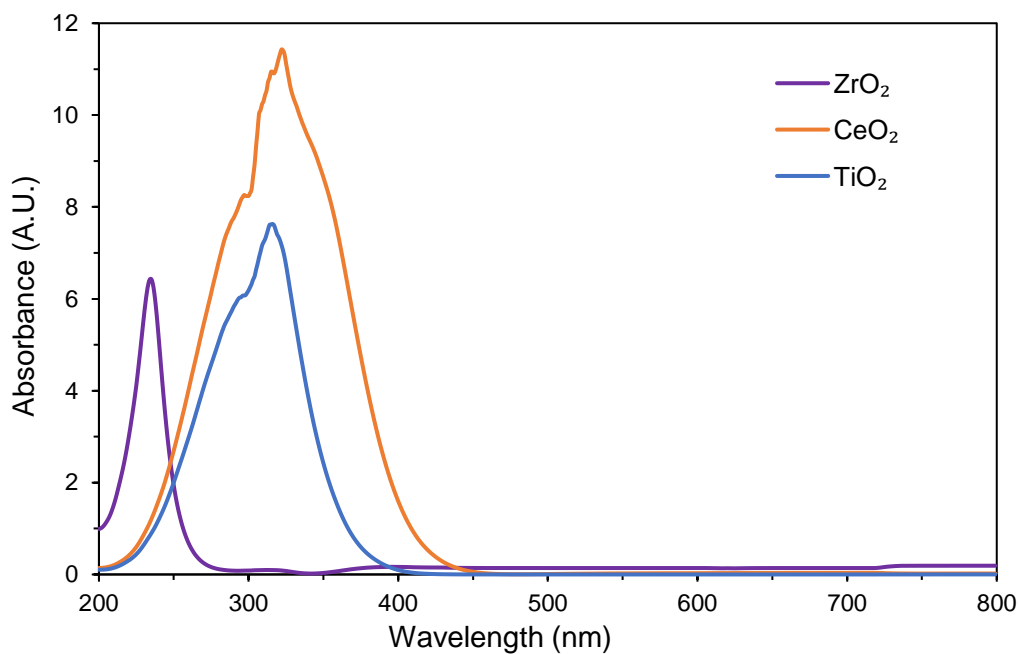
Figure A.1 UV−Vis DRS absorption spectra of different supports.
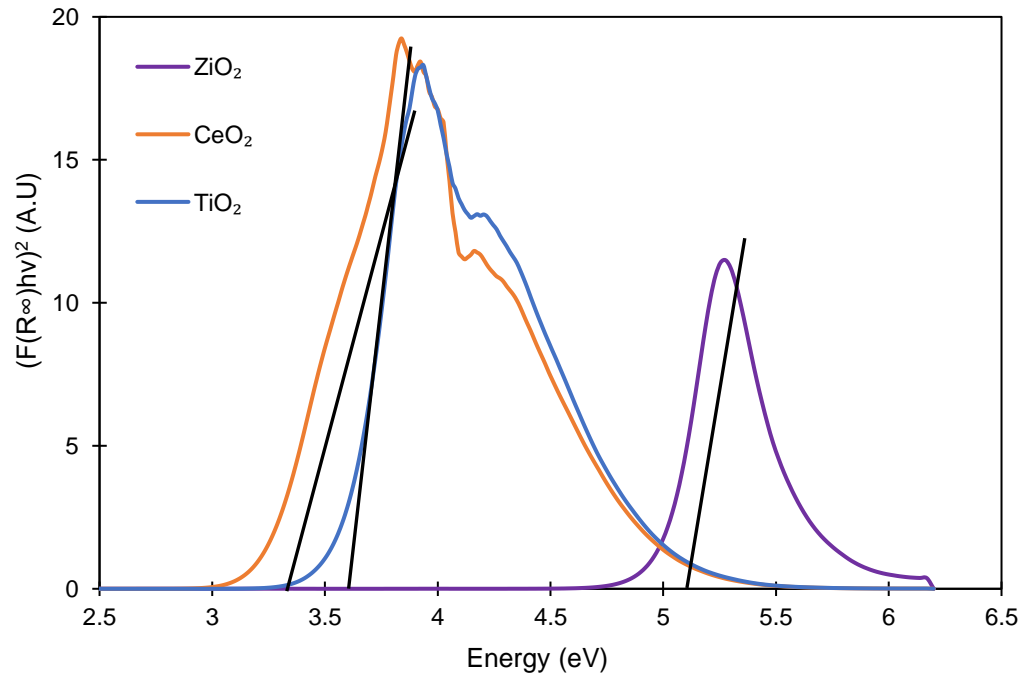
Figure A.2 UV–Vis DRS absorption edges energy (Eg) of the blank supports.
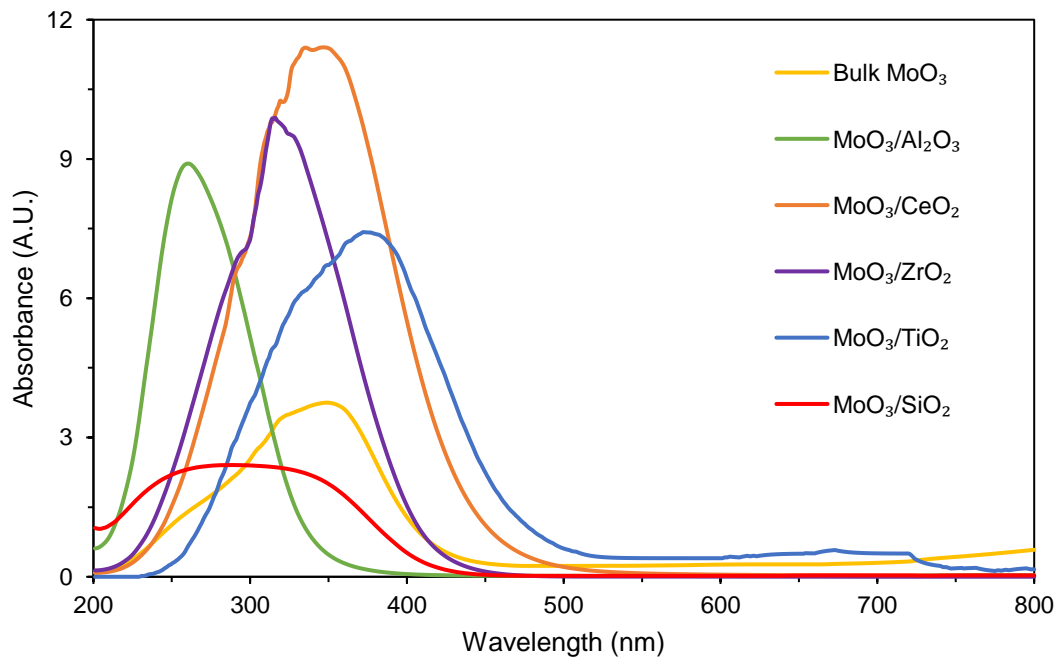
Figure A.3 UV-Vis DRS absorption spectra of the supported MoO₃ catalysts.
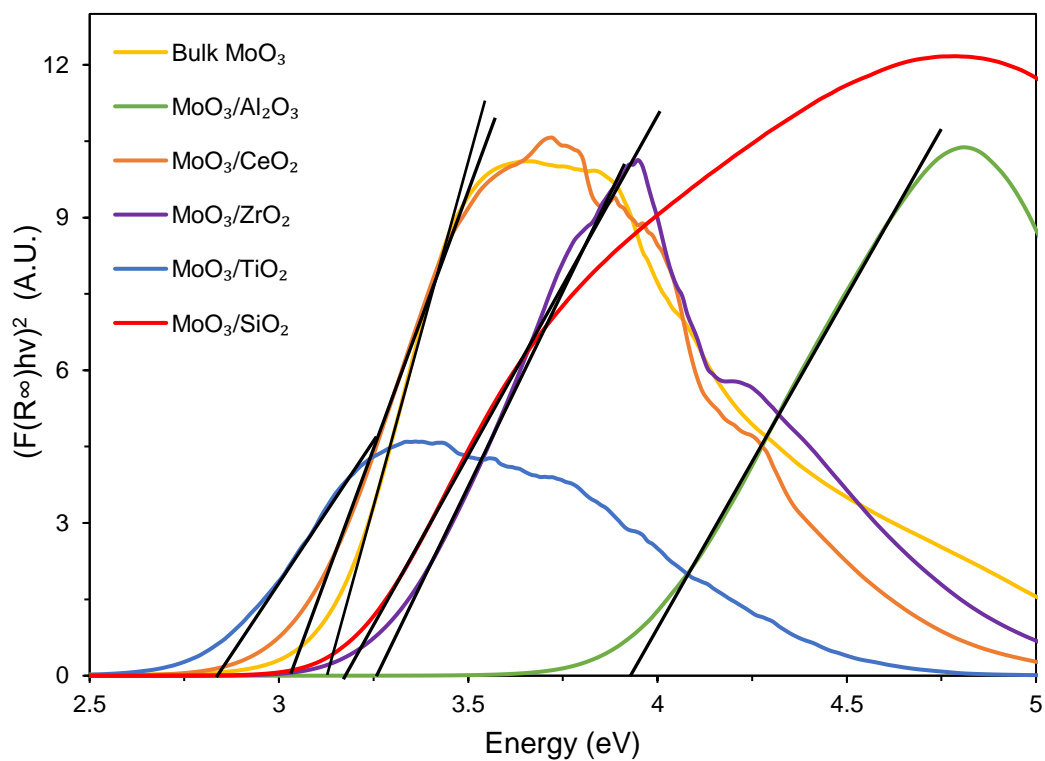
Figure A.4 UV-Vis DRS absorption edge energy (Eg) of the supported MoO₃ catalysts.
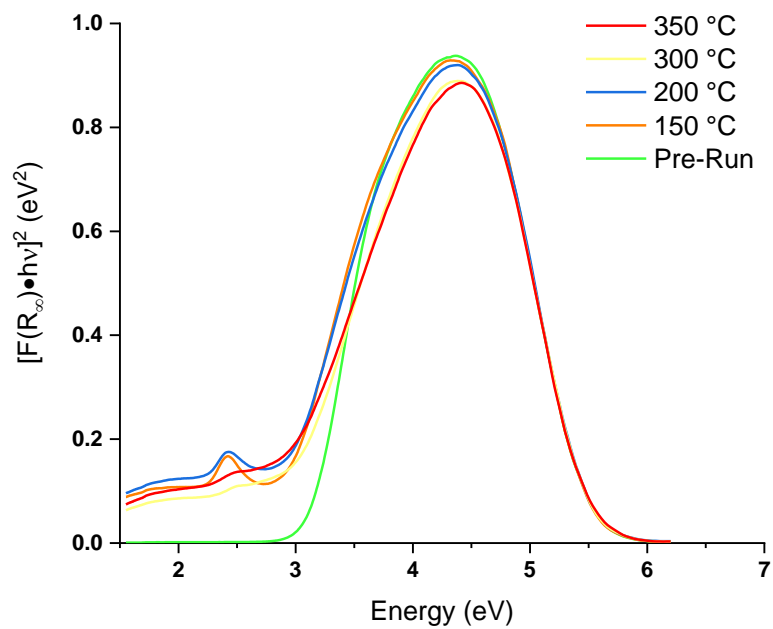
Figure A.5 In situ UV-Vis spectra of MoO₃/SiO₂ under the reduction atmosphere.
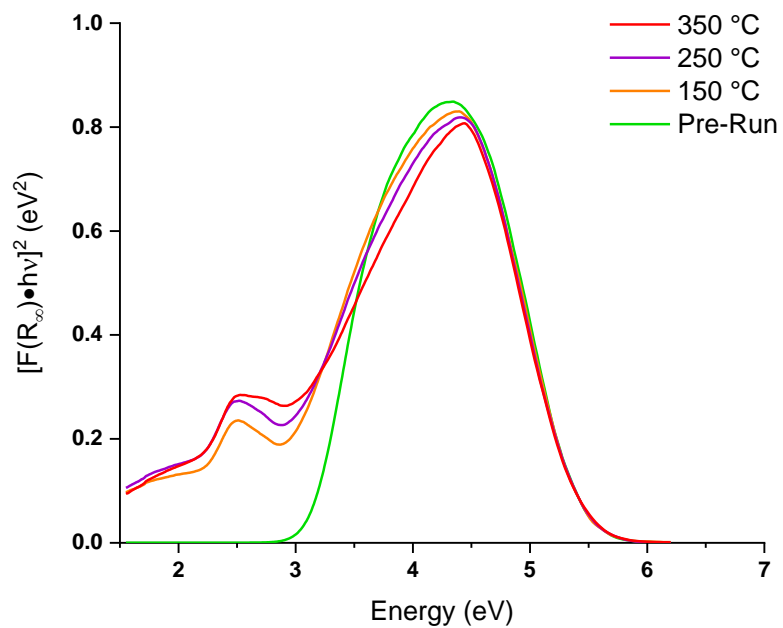
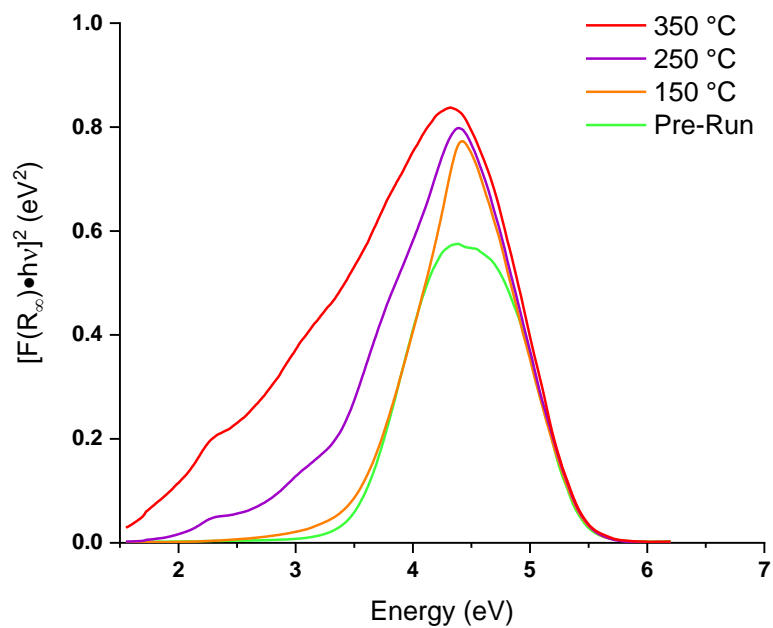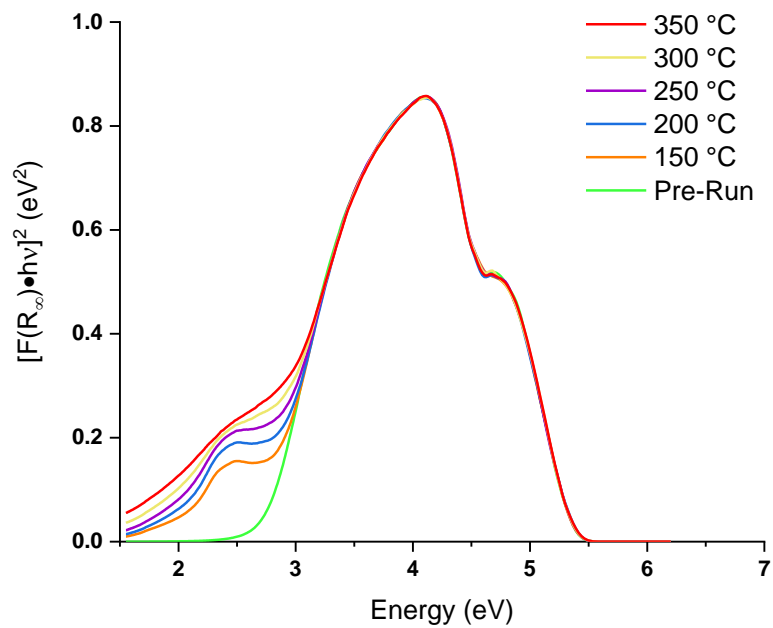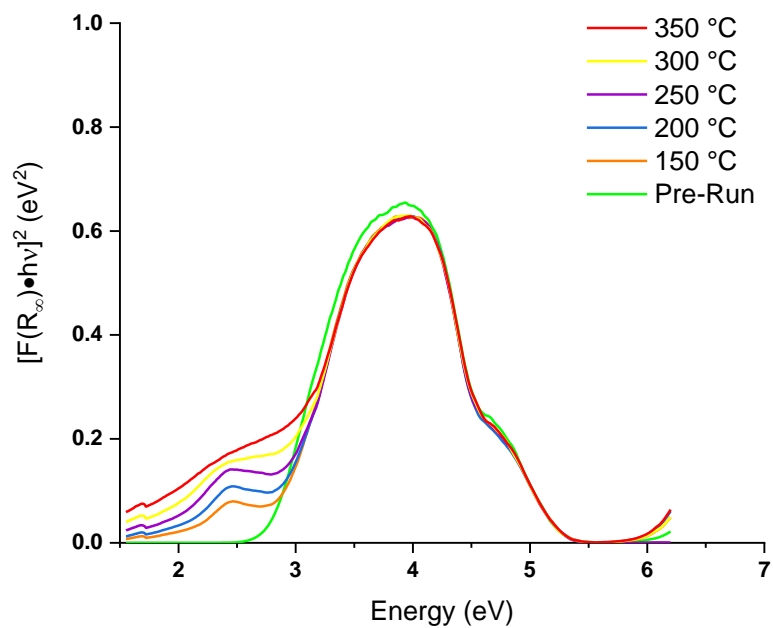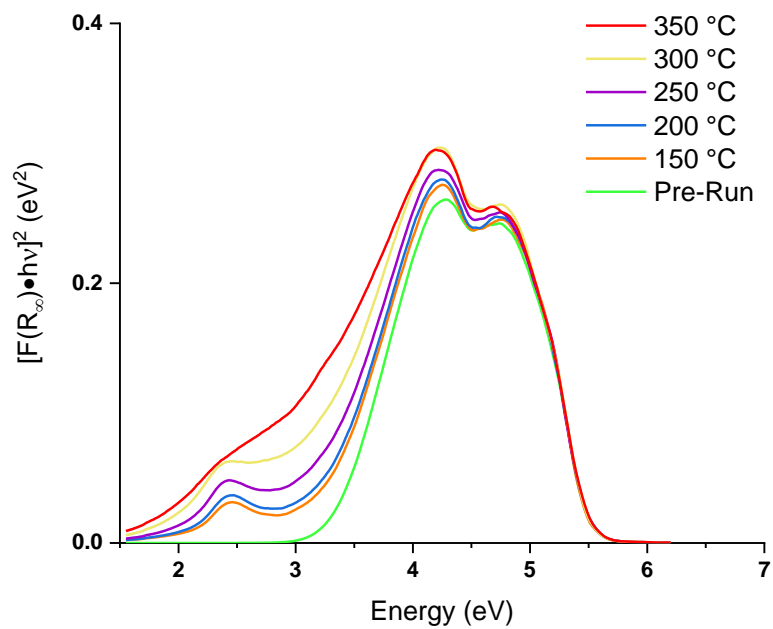**Figure A.6 In situ UV-Vis spectra of MoO₃/SiO₂ under the reaction atmosphere.**
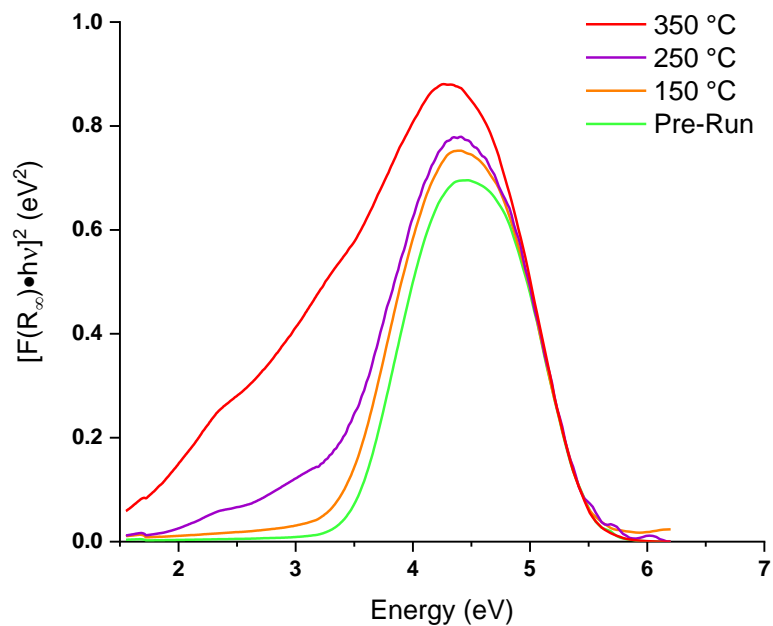
Figure A.7 In situ UV-Vis spectra of MoO₃/Al₂O₃ under the reduction atmosphere.

Figure A.8 In situ UV-Vis spectra of MoO$_3$/Al$_2$O$_3$ under the reaction atmosphere.

Figure A.9 In situ UV-Vis spectra of MoO$_3$/CeO$_2$ under the reduction atmosphere.

Figure A.10 In situ UV-Vis spectra of MoO₃/CeO₂ under the reaction atmosphere.

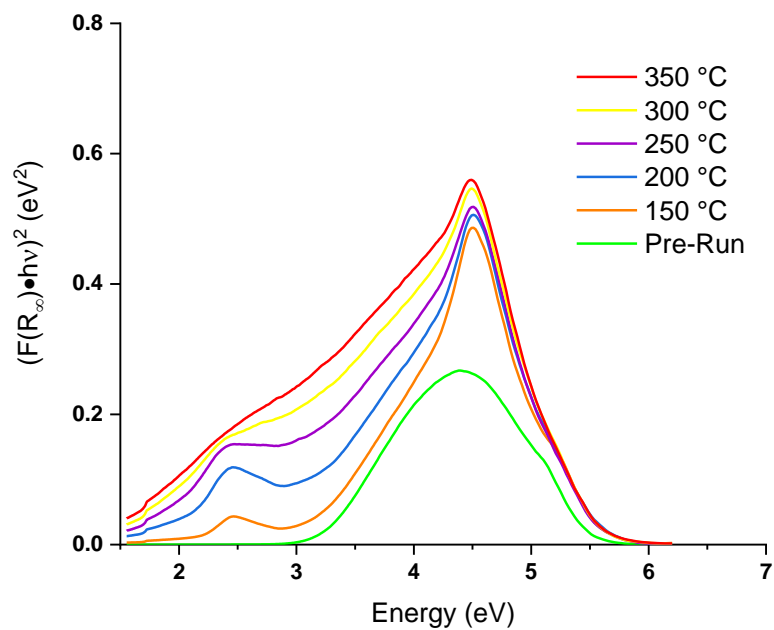**Figure A.11 In situ UV-Vis spectra of MoO₃/ZrO₂ under the reduction atmosphere.**

Figure A.12 In situ UV-Vis spectra of MoO$_3$/ZrO$_2$ under the reaction atmosphere.
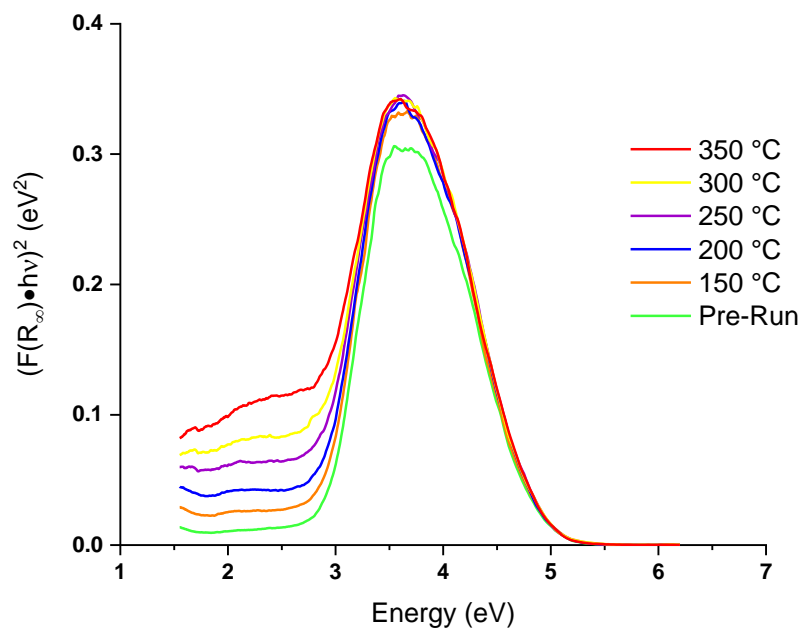

Figure A.13 In situ UV-Vis spectra of bulk MoO$_3$ under the reduction atmosphere.
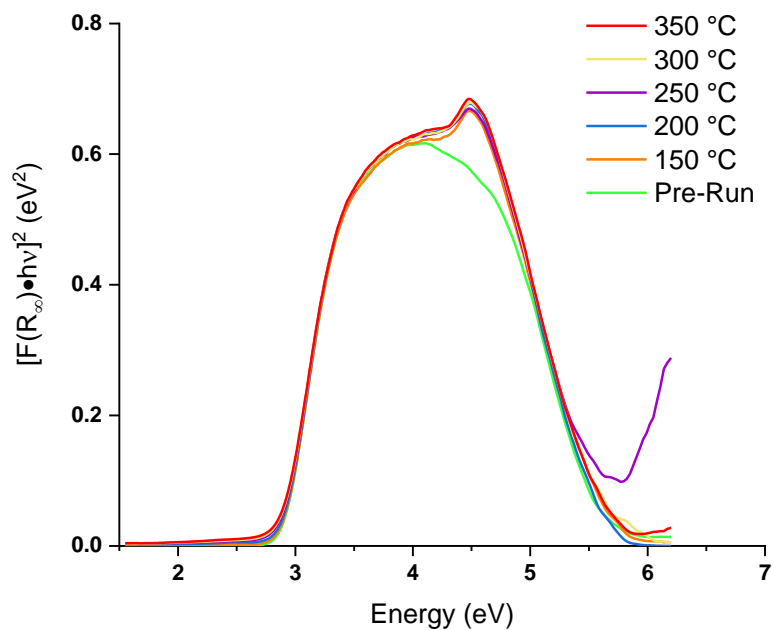
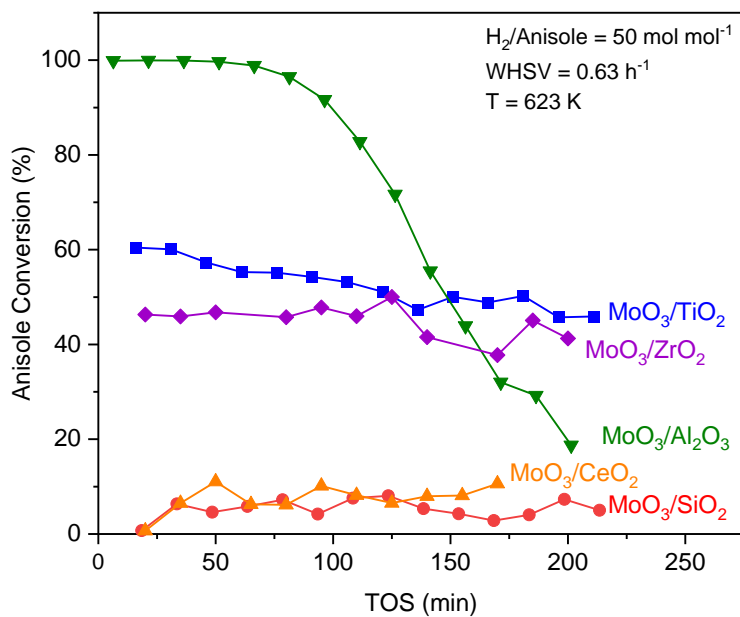**Figure A.14 In situ UV-Vis spectra of bulk MoO₃ under the reaction atmosphere.**

Figure A.15 Activity data for the conversion of anisole over supported MoO₃ catalysts, P$_{Total}$ = 1.013 bar (0.0191 bar P$_{Feed}$, balance H₂)

Curriculum Vitae

Name:	Chantal Walker

Post-secondary Education and Degrees:

New Mexico State University
Las Cruces, New Mexico, United States
2011-2013 Completed first two years of BSc. in Chemical Engineering

Western University
London, Ontario, Canada
2013-2017 BESc in Chemical Engineering

Western University
London, Ontario, Canada
2018-2020 MESc in Chemical Engineering

Honours and Awards:

Regents Scholarship
Awarded to each student admitted with a 4.0+/4.0 GPA
Aug 2011-May 2012

Crimson Scholar
Awarded to each student who maintains a 3.5+ GPA
Aug 2011-May 2013

Dean's Honour List
Awarded to each student who maintains an 80%+ average
Sept 2015-Apr 2016

Western Graduate Research Scholarship
Awarded to each student who maintains a 78%+ average
Aug 2018-Dec 2020

Ontario Graduate Scholarship
Merit-based scholarship awarded to domestic graduate students conducting research in science and technology fields
Apr 2019-Apr 2020

Related Work Experience

Teaching Assistant
Western University
Sept 2018-Apr 2020